Terahertz Time-domain Spectroscopy and Imaging for Quantitative Skin Characterization

WANG, Jiarui

A Thesis Submitted in Partial Fulfilment

of the Requirements for the Degree of

Doctor of Philosophy

in

Electronic Engineering

The Chinese University of Hong Kong

July 2021

Declaration

I hereby declare this thesis is my original work and contains nothing which is the result of work done in collaboration with others, except as specified in the text and Acknowledgement. This work has not been submitted to this or any other university for the award of any degree.

The materials of some chapters have been published in the following journal and conference papers:

- Chapter 1

Jiarui Wang, Hannah Lindley-Hatcher, Xuequan Chen, Emma Pickwell-MacPherson, "THz Sensing of Human Skin: A Review of Skin Modeling Approaches", Sensors 21 (11), 3624, 2021.

- Chapter 2

Jiarui Wang, Hannah Lindley-Hatcher, Xuequan Chen, Emma Pickwell-MacPherson, "THz Sensing of Human Skin: A Review of Skin Modeling Approaches", Sensors 21 (11), 3624, 2021.

- Chapter 3

Jiarui Wang, Rayko I Stantchev, Qiushuo Sun, Tor-Wo Chiu, Anil T Ahuja, Emma Pickwell MacPherson, "THz in vivo measurements: the effects of pressure on skin reflectivity", Biomedical optics express 9 (12), 6467-6476, 2018.

Hannah Lindley-Hatcher, AI Hernandez-Serrano, Qiushuo Sun, **Jiarui Wang**, Juan Cebrian, Laurent Blasco, Emma Pickwell-MacPherson, "A robust protocol for in vivo THz skin measurements", Journal of Infrared, Millimeter, and Terahertz Waves 40 (9), 980-989, 2019.

Hannah Lindley-Hatcher, AI Hernandez-Serrano, **Jiarui Wang**, Juan Cebrian, Joseph Hardwicke, Emma Pickwell-MacPherson, "Evaluation of in vivo THz sensing for assessing human skin hydration", Journal of Physics: Photonics 3 (1), 014001, 2020.

Qiushuo Sun, Rayko I Stantchev, **Jiarui Wang**, Edward PJ Parrott, Alan Cottenden, Tor - Wo Chiu, Anil T Ahuja, Emma Pickwell - MacPherson, "In vivo estimation of water diffusivity in occluded human skin using terahertz reflection spectroscopy", Journal of biophotonics 12 (2), e201800145, 2019

Jiarui Wang, Hannah Lindley-Hatcher, Xuequan Chen, Emma Pickwell-MacPherson, "THz Sensing of Human Skin: A Review of Skin Modeling Approaches", Sensors 21 (11), 3624, 2021

Jiarui Wang, Rayko I Stantchev, Qiushuo Sun, Emma Pickwell-MacPherson, "The Effect of Pressure on Terahertz In Vivo Spectroscopic Imaging", in International Conference on Infrared, Millimeter, and Terahertz Waves, IRMMW-THz, 2018

Hannah Lindley, AI Hernandez-Serrano, Qiushuo Sun, **Jiarui Wang**, Emma Pickwell-MacPherson, "Pressure Controlled in vivo THz Measurements of Skin: Monitoring the Effects of Moisturizers", in International Conference on Infrared, Millimeter, and Terahertz Waves, IRMMW-THz, 2019

- Chapter 4

Jiarui Wang, Qiushuo Sun, Rayko I Stantchev, Tor-Wo Chiu, Anil T Ahuja, Emma Pickwell-MacPherson, "In vivo terahertz imaging to evaluate scar treatment strategies: silicone gel sheeting", Biomedical optics express 10 (7), 3584-3590, 2019

Qiushuo Sun, Rayko I Stantchev, **Jiarui Wang**, Edward PJ Parrott, Alan Cottenden, Tor - Wo Chiu, Anil T Ahuja, Emma Pickwell - MacPherson, "In vivo estimation of water diffusivity in occluded human skin using terahertz reflection spectroscopy", Journal of biophotonics 12 (2), e201800145, 2019

Jiarui Wang, Qiushuo Sun, Rayko I Stantchev, Emma Pickwell-MacPherson, "In Vivo Terahertz Skin Imaging for Scar Treatment Evaluation", in International Conference on Infrared, Millimeter, and Terahertz Waves, IRMMW-THz, 2019

- Chapter 5

Jiarui Wang, Hannah Lindley-Hatcher, Kai Liu, Emma Pickwell-MacPherson, "Evaluation of transdermal drug delivery using terahertz pulsed imaging", Biomedical Optics Express 11 (8), 4484-4490, 2020

Jiarui Wang, Emma Pickwell-MacPherson, "Terahertz Imaging for Topical and Micro/Nano Needle Patch Drug Delivery", in International Conference on Infrared, Millimeter, and Terahertz Waves, IRMMW-THz, 2020

- Chapter 6

Jiarui Wang, Hannah Lindley-Hatcher, Xuequan Chen, Emma Pickwell-MacPherson, "THz Sensing of Human Skin: A Review of Skin Modeling Approaches", Sensors 21 (11), 3624, 2021.

Xuequan Chen, Qiushuo Sun, **Jiarui Wang**, Hannah Lindley-Hatcher, Emma Pickwell-MacPherson, "Exploiting complementary terahertz ellipsometry configurations to probe the hydration and cellular structure of skin in vivo", Advanced Photonics Research, 2000024, 2021

- Chapter 7

Jiarui Wang, Hannah Lindley-Hatcher, Xuequan Chen, Emma Pickwell-MacPherson, "THz Sensing of Human Skin: A Review of Skin Modeling Approaches", Sensors 21 (11), 3624, 2021.

This thesis does not exceed 50,000 words.

WANG Jiarui	WANG Jiarui	18th June 2021
Student Name	Signature	Date
Prof Emma MacPherson	E MacPherson	18th June 2021
Supervisor	Signature	Date

Abstract

Terahertz (THz) light is located between microwave and infrared light with frequencies between 0.1 and 10 THz (1 THz=10^{12} Hz). As a non-invasive and non-ionizing imaging technique, THz spectroscopy and imaging can distinguish different tissue types and pathological changes, which makes it a favorable tool for *in vivo* skin characterization without interfering the living skin system. Moreover, the high absorption by water makes THz light highly sensitive to water offering the potential for diagnosis of diseases that affect the water content. However, some key variables affect THz *in vivo* skin measurement, such as the duration of skin contact with the imaging window and the contact pressure. Research has been done to explore the ability of THz imaging for skin hydration sensing but skin structure characterization study in THz regime is still underdeveloped.

In this thesis, the variables that affect *in vivo* skin measurements are discussed in Chapter 3 with methods to minimize or at-least control the pressure effect, occlusion effects and individual differences. A systematic study about the changes caused by contact pressure is also included in this chapter. Potential applications by THz spectroscopy and imaging are also proposed and demonstrated in Chapter 4-5. Namely in Chapter 4, *in vivo* study on human about silicone gel sheet (SGS) effects is demonstrated. Fluidic changes caused by SGS application is monitored. In Chapter 5, we employed THz imaging to compare the efficiency of different transdermal drug delivery methods using *ex vivo* porcine skin.

Imaging with a THz time-domain spectrometer (THz-TDS) has been used to study the skin hydration and layer thickness. In Chapter 6, we further expand the ability of THz-TDS system to study anisotropic properties of the stratum corneum (SC) by installing a double prism system and polarizers into the THz-TDS system. With the proposed anisotropic skin model, we are able to study both the hydration and inhomogeneity of SC caused by occlusion and topical applications of skin products.

In summary, this thesis focuses on using a THz-TDS system to characterize skin properties with different optical models and instrumentation.

摘要

太赫茲光波處於微波和紅外光波之間，頻率介於 0.1 到 10 THz（1 THz=10^{12} Hz）。基於其無創、非電離的特性，太赫茲光譜及成像可以分辨不同的組織及病理變化。這使得太赫茲技術在皮膚表徵方面有很大的應用價值并且不會對活體產生影響。更重要的是，太赫茲在水裏有很高的吸收性，這使得太赫茲光波可以靈敏的反映出水含量。但是利用太赫茲測量在體皮膚時，其結果常常受到多種因素的影響，例如，皮膚與探測窗口的接觸壓力以及由於接觸所導致的皮膚水分難以蒸發進入環境。目前有很多利用太赫茲技術檢測皮膚含水量的研究，但是利用太赫茲技術探測皮膚結構的研究相對較少。

本篇論文中，我們在第三章討論了影響太赫茲在體檢測皮膚的參數，并且提出了一些減少接觸壓力、不同受試者皮膚狀態等導致的誤差的方法。關於接觸壓力造成的影響系統地總結在第三章。另外，我們也研究了太赫茲光譜學及成像的潛在應用。在第四章，我們研究了太赫茲檢測在硅膠治療方面的應用。我們利用太赫茲檢測了由於硅膠治療而導致的皮膚內水分變化。在第五章，我們利用太赫茲成像技術比較了不同經皮給藥的效率。

太赫茲光譜學及成像技術已經被應用於皮膚含水量及皮膚層厚度檢測。在第六章，我們擴大了太赫茲時域光譜系統在皮膚結構方面的檢測能力。通過植入一個雙棱鏡系統，角質層的各向異性被檢測出來。利用所提出的各項異性的皮膚模型，我們不僅可以研究在不同過程中皮膚含水量變化，還可以研究皮膚的均一性。

總結來說，本篇論文主要聚焦於利用太赫茲時域光譜系統、皮膚光學模型及儀表技術來表徵皮膚。

Acknowledgement

Time flies fast and at this moment, I would like to express my gratitude to all the people who helped me throughout my journey to get the Ph.D degree.

Firstly, I would like to thank my supervisor Prof. Emma Pickwell-MacPherson who is always nice and patient to us. Her patience and respects to students made me have a happy time in the past four years. I still remember the first year when I stepped into CUHK and I could not adapt to the new life quickly and usually felt upset. She not only guided me in my research but also shared tips in life. She also made our group very united and created a great atmosphere for us. I feel so lucky to be her student!

I would also thank my co-supervisor Prof. Thierry BLU for all the technical suggestions about my research and knowledge about mathematics. He is always patient and listened my works carefully every time.

My gratitude also goes to Dr. Rayko Ivanov Stantchev. He helped me to install the pressure sensors into our system, provided suggestions and also revised every manuscript carefully. He was always very helpful, patient and willing to be the subject when I conducted *in vivo* experiments. I would also thank another post-doc in our group Dr. Xuequan Chen who helped me a lot about the data processing and also give me many suggestions. He has taught me to build and align our THz systems. I would also thanks Dr. Rui Zhang for his suggestions not only in research but also in life and career.

I would also thank all the other members in our group. I am so lucky to have Dr. Qiushuo Sun to be our senior. She organized a lot of activities the first year I joined our group. She was the first one who taught me to use our systems and conduct experiments. She also encouraged me to do my first project. I am very grateful for all her help both in research and life. I also thank Kai Liu for his help and suggestion from medical aspects in the transdermal drug delivery project. He also helped me a lot in life. I also thank Kaidi Li for all the talks we had in both research, life and future career. I really enjoyed all the activities he organized in the past four years. I thank both Kai and Kaidi for all the great travels we had in the past four years. I would also thank our group members in Warwick. I would thank Hannah Lindley-Hatcher for revising my papers and providing suggestions. She also helped me to revise the English of my thesis.

I would also thank all my friends. I thank Hetong Wang for all the great funs we had. In the past four years, we celebrated birthdays and many holidays together. We shared our happiness and sadness. I would also thank Kejia Li for her support when I am upset. Though we were not in the same city, she was still the one I wanted to talk to when things did not go my way. I would like to express my thank to Yiting Xu for all the chats we had about career and life. I would also thank Ruifang Han for her kind help when I need to use the equipment from their group. I would thank all my friends and colleagues in EE department for their generous help.

Before I stepped into CUHK, I had met a lot of great professors and teachers. I would like to thank all of them for making me what I am now. Thank Prof. Lelun

Jiang for giving me the great opportunity during my undergraduate to work in his lab where I also met my boyfriend. Thank Prof. Rong Song for introducing MATLAB software which I frequently used in the past four years. Thank Prof. Yunxi Luo for his patience in teaching both artificial and digital circuit which made me quickly install the pressure sensors into the THz system.

I also want to express my thanks and love to my boyfriend Dr. Chengfeng Pan. I am very grateful that I could have such a wonderful boyfriend. He is knowledgeable and has given me so many suggestions in the past four years. Thank him for his support and company in the past four years. We both spent efforts to maintain the long-distance relationship.

Last but not the least, I want to thank my family, my father, my mother and my little brother for all their support and love throughout my life. Thank my father who always encourages me. He also spent efforts in his career. His kindness and generosity to others have left a seed into my heart and encourages me to be kind. His attitude towards work also makes me dedicate to my work. He is an ordinary man but he tries his best to make a difference in the area he worked. I would also thank my mother for all her support in life. She had given me freedom to choose what I want, what I study, what I wear since I was a child. She is an independent woman and also encourages me to be independent. She encouraged me to travel alone when I reached an adult age. When I have difficulties, she also makes me feel that I have backups. I would like to thank my little brother. He is so sweet and has brought so much fun to our family. Though it was not always happy when he was little and naughty, he always bought me my favorite snacks when I went home. I

would also thank my grandparents for loving and taking care of me when my parents were busy in my childhood. I am so lucky to have such great family and I will love you all forever.

Collaborative notes

I would like to acknowledge Dr. Xuequan Chen for the designing, coding and algorithms of THz systems and ellipsometer project, Dr. Rayko Ivanov Stantchev and Dr. Qiushuo Sun for the help and instructions on pressure effect project and silicone gel sheet project, Dr. Tor Wo Chiu for providing suggestions on the silicone gel sheet project.

Contents

List of Figures

List of Publications

Peer-Review Journals:

1. **Jiarui Wang**, Rayko I Stantchev, Qiushuo Sun, Tor-Wo Chiu, Anil T Ahuja, Emma Pickwell MacPherson, "THz in vivo measurements: the effects of pressure on skin reflectivity", Biomedical optics express 9 (12), 6467-6476, 2018
2. **Jiarui Wang**, Qiushuo Sun, Rayko I Stantchev, Tor-Wo Chiu, Anil T Ahuja, Emma Pickwell-MacPherson, "In vivo terahertz imaging to evaluate scar treatment strategies: silicone gel sheeting", Biomedical optics express 10 (7), 3584-3590, 2019
3. Qiushuo Sun, Rayko I Stantchev, **Jiarui Wang**, Edward PJ Parrott, Alan Cottenden, Tor - Wo Chiu, Anil T Ahuja, Emma Pickwell–MacPherson, "In vivo estimation of water diffusivity in occluded human skin using terahertz reflection spectroscopy", Journal of biophotonics 12 (2), e201800145, 2019
4. Hannah Lindley-Hatcher, AI Hernandez-Serrano, Qiushuo Sun, **Jiarui Wang**, Juan Cebrian, Laurent Blasco, Emma Pickwell-MacPherson, "A robust protocol for in vivo THz skin measurements", Journal of Infrared, Millimeter, and Terahertz Waves 40 (9), 980-989, 2019
5. **Jiarui Wang**, Hannah Lindley-Hatcher, Kai Liu, Emma Pickwell-MacPherson, "Evaluation of transdermal drug delivery using terahertz pulsed imaging", Biomedical Optics Express 11 (8), 4484-4490, 2020
6. Hannah Lindley-Hatcher, AI Hernandez-Serrano, **Jiarui Wang**, Juan Cebrian, Joseph Hardwicke, Emma Pickwell-MacPherson, "Evaluation of in vivo THz sensing for assessing human skin hydration", Journal of Physics: Photonics 3 (1), 014001, 2020
7. **Jiarui Wang**, Hannah Lindley-Hatcher, Xuequan Chen, Emma Pickwell-MacPherson, "THz Sensing of Human Skin: A Review of Skin Modeling Approaches", Sensors 21 (11), 3624, 2021
8. Xuequan Chen, Qiushuo Sun, **Jiarui Wang**, Hannah Lindley-Hatcher, Emma Pickwell-MacPherson, "Exploiting complementary terahertz

ellipsometry configurations to probe the hydration and cellular structure of skin in vivo", Advanced Photonics Research, 2000024, 2021

Conference Presentations and Proceedings:

1. **Jiarui Wang**, Rayko I Stantchev, Qiushuo Sun, Emma Pickwell-MacPherson, "The Effect of Pressure on Terahertz In Vivo Spectroscopic Imaging", in International Conference on Infrared, Millimeter, and Terahertz Waves, IRMMW-THz, 2018
2. **Jiarui Wang**, Qiushuo Sun, Rayko I Stantchev, Emma Pickwell-MacPherson, "In Vivo Terahertz Skin Imaging for Scar Treatment Evaluation", in International Conference on Infrared, Millimeter, and Terahertz Waves, IRMMW-THz, 2019
3. Hannah Lindley, AI Hernandez-Serrano, Qiushuo Sun, **Jiarui Wang**, Emma Pickwell-MacPherson, "Pressure Controlled in vivo THz Measurements of Skin: Monitoring the Effects of Moisturizers", in International Conference on Infrared, Millimeter, and Terahertz Waves, IRMMW-THz, 2019
4. Xuequan Chen, Qiushuo Sun, **Jiarui Wang**, Hannah Lindley, Kai Liu, Kaidi Li, Xavier Barker, Rayko Stantchev, Arturo Hernandez, Emma Pickwell-MacPherson, "THz Instrumentation and Analysis Techniques for Biomedical Research", in International Conference on Infrared, Millimeter, and Terahertz Waves, IRMMW-THz, 2019
5. **Jiarui Wang**, Emma Pickwell-MacPherson, "Terahertz Imaging for Topical and Micro/Nano Needle Patch Drug Delivery", in International Conference on Infrared, Millimeter, and Terahertz Waves, IRMMW-THz, 2020

1. Introduction

1.1 Terahertz radiation

Terahertz radiation (THz) lies between 0.1 to 10 THz (1 THz=10^{12} Hz) with wavelengths ranging from 30 μm to 3 mm, this lies between far infrared radiation and microwaves, as illustrated in Fig.1. 1. This region has been called the "THz gap" because of the difficulties faced in THz generation and detection. In 1975, David H. Auston developed the first photo-conductive antenna which enabled the generation and detection of broadband THz pulses[1]. Due to the rapid recent development of THz research especially in THz devices and applications, commercialized THz systems are now available for use in research. Therefore, THz spectroscopy and imaging have been used in a wide range of applications, for example, communication, cultural heritage analysis, security, molecular structure characterization and biomedical imaging[2].

The photon energy of THz radiation ranges from 0.4 meV to 40 meV, this is significantly lower than the ionization energy of hydrogen. The low energy of THz radiation makes it very suitable for biomedical imaging as we expect it to be safe for use on living subjects. Moreover, THz spectrometers can provide frequency domain spectra, this enables chemical characterization based on the unique fingerprint of certain chemicals. The sensitivity to water limits the capability for measurements of deeper layers of tissue but it does make THz radiation suitable for measuring biological samples and performing measurements of the skin.

Indeed, several studies have demonstrated the potential of THz imaging as a medical modality for tissue imaging[3,4].

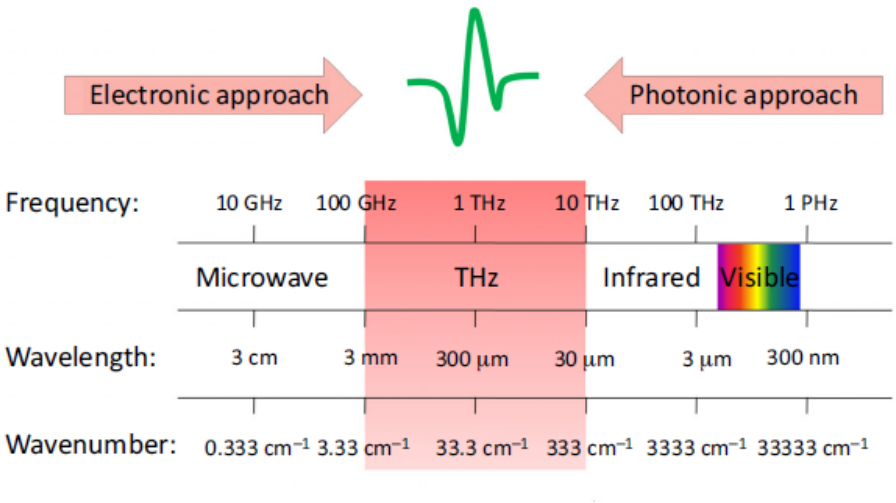

Fig.1. 1 The electromagnetic spectrum showing the location of THz waves [2]

1.2 Medical imaging methods

There are different imaging or non-imaging methods for skin or tissue measurements. The aim of skin measurement is mainly to extract the morphology, histology and functionality of the skin[5]. Moreover, it is of great interest to apply skin imaging for diagnosis of skin lesions and pathological processes objectively and quantitively[6]. To better illustrate that THz spectroscopy could be a promising technique for biomedical imaging and medical diagnosis, different imaging methods will be compared in this section.

Observation with the “naked eye” is one of the primary tools used for skin assessment. However, it is limited by variation from person to person and can only reveal surface changes in the skin[5]. Histological examination of biopsies usually combined with optical microscopy is another option but it is invasive and also

requires sample preparation and fixation which can change the biological properties[7]. Therefore, to meet the need for non-invasive in vivo measurements of the skin, emerging techniques are now available or are being developed. Optical microscopy is usually used for the detection of morphological changes in tissues. However, it usually requires sample preparation and fixation which can cause damage or changes in biological samples[5]. When the sample is thick and structures overlap, confocal laser scanning microscopy (CLSM) is more suitable[8]. However, the long scanning time and potential changes in the sample during scanning need to be considered in order to acquire high-quality images. Fluorescence microscopy is another kind of optical microscope based on fluorescence and phosphorescence, combined with CLSM, it has been widely used for evaluating transdermal drug delivery[9]. It is able to track and quantitatively analyze drugs labeled with fluorescent dyes. Electron microscopy provides especially high resolution(nm). However, sample preparation is needed to enhance the contrast. Moreover, transmission electron microscopy has been used to image the shape of corneocytes in the stratum corneum (SC) and the morphology of individual layers in the SC[10]. Vibrational spectroscopy is capable of identifying chemicals without labeling. Near infrared(NIR) imaging is a commonly used technique for skin measurement, and because of the clear absorption bands of water molecules at 1450 and 1920 nm, it can also be used for hydration sensing[11]. However, NIR usually produces complex spectra which are difficult to interpret, it has low resolution (5~10 μm)[12] and is difficult to resolve the hydration at an

arbitrary depth[13]. Raman spectroscopy combined with confocal microscopy can identify chemical components and observe their concentration distribution through the depth of the skin[14]. Though the penetration depth can reach up to 150 mm, the resolution is about 5 μm. The Fourier-transformed infrared (FTIR) spectrum for a tissue is dominated by the absorption of water making it difficult for this method to extract information about other bio-molecules. Attenuated total reflectance FTIR can help by sampling only the superficial layers of tissue making the water absorption less pronounced, but will lead to a very shallow penetration depth[15]. THz spectroscopy is able to observe intermolecular vibrations in some chemicals[16] whereas infrared waves reveal intermolecular modes[17]. Based on dielectric differences of normal and malignant tissues, microwave and millimeter-wave technologies also have the potential to provide cost-effective options for tumor diagnosis. It has been reported that millimeter waves are also sensitive to the water and thickness variation of skin and could be a potential technique for skin diagnosis[18][19]. Compared to THz waves, millimeter waves have a deeper penetration depth in living tissues of over 1 mm, reaching down to the dermis layer[20]. However, the longer wavelengths also restrict the spatial resolution limit for standard imaging configurations. Optical coherence tomography (OCT) is another method based on interferometric techniques that can be used for skin measurements, but it is mainly used to measure the morphology and structure of the skin[21,22]. Magnetic resonance imaging (MRI) is another commercialized medical imaging technique that can detect protons in water and therefore can be

used for tissue hydration sensing. However, it has some limitations. MRI mainly focus on soft tissue though there is research which applies this technique for skin imaging, but it is still at a preliminary stage[23] and its depth resolution is about 50-100 μm. Based on the sensitivity of THz radiation to water and its suitable penetration depth (100um to several mm) into skin and tissues, we believe that the development of THz imaging could enable effective analysis of the properties of the skin giving quantitative results and could aid the diagnosis of skin lesions and pathological processes. THz spectroscopy is able to observe intermolecular vibrations in some chemicals[16] whereas infrared waves reveal intramolecular modes[17].

1.3 THz biomedical applications

The main biomedical applications of THz imaging for skin focus on the diagnosis of cancer, scar measurement, drug diffusion monitoring and hydration sensing. The origin of these applications is based on the sensitivity to water and other liquids such as dimethyl sulfoxide (DMSO) and glycerol. Therefore, in this section, a brief introduction to skin and tissue related works is presented.

1.3.1. THz spectroscopy and imaging of skin

Skin is the largest organ in human body constituting 15-20% of the mass of the human body. Skin helps protect the body from dehydration and microbes. Skin has three primary layers: epidermis, dermis and hypodermis layers[24]. Skin is 20-70% water, making water one of the primary components of skin, skin also contains

collagen, elastin and other proteins. The epidermis is divided into 2 layers, the SC and the viable epidermis as shown by Fig.1. 2. As the outmost layer of the skin, the thickness of the SC varies across the body[25].

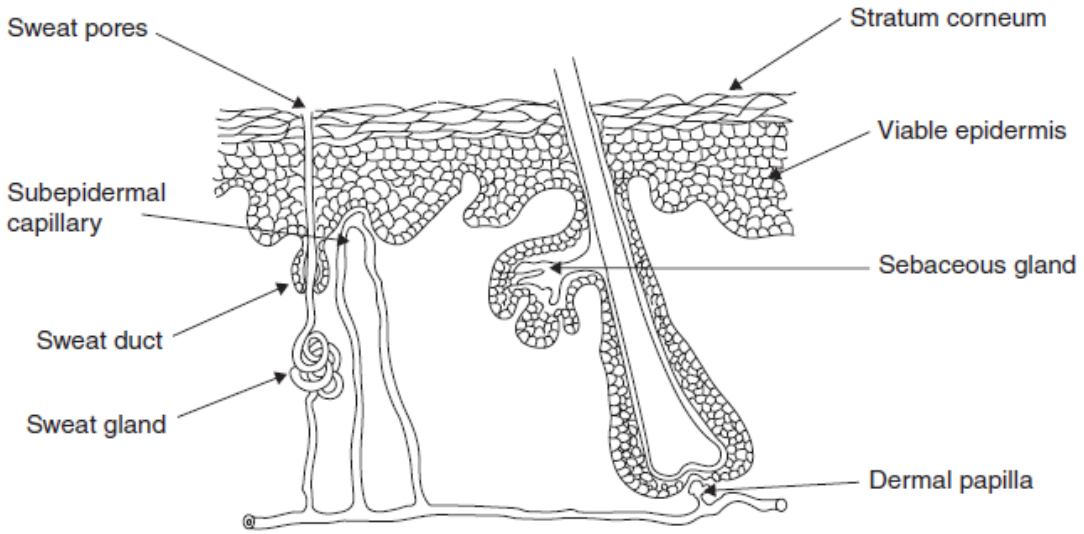

Fig.1. 2 Diagram of the cross-section of human skin[25]

Cole et al have shown that THz imaging and spectroscopy is able to differentiate the SC from the epidermis and observe the changes in thickness at different sites on the body [26]. As shown in Fig.1. 3 (a), the THz pulse reflected from the palm has a second reflection from the SC-epidermis interface for palm skin. However, for skin at other body sites such as the volar forearm and wrist, this is not observed as the SC is too thin (around 10-20 μm[24,27]) so the second reflection cannot be recognized as shown by Fig.1. 3 (b). Echchgadda et al. demonstrated the varied refractive index and absorption coefficient spectra observed at different body sites[28].

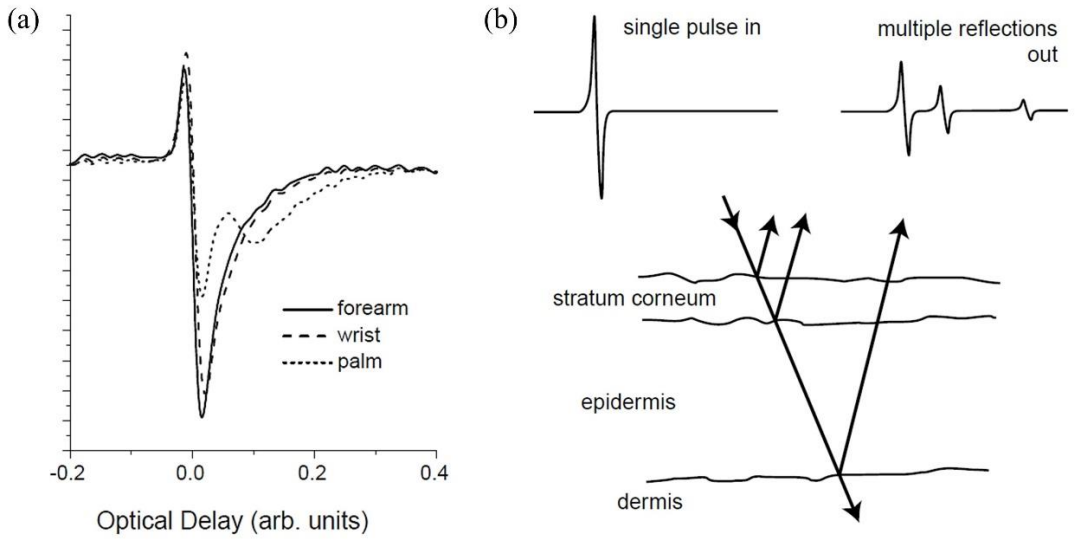

Fig.1. 3 (a) Processed THz pulse reflected from forearm, wrist and palm. (b) Diagram of multi reflections[26]

However, in reality, point measurements alone cannot satisfy the needs of medical applications. Therefore, THz imaging is developed to not only provide spectral information but also provide spatial information [29].

1.3.2. THz imaging for cancer diagnosis

One of most attractive applications of THz imaging is the diagnosis of cancer, especially diagnosis of skin cancer due to the shallow penetration depth of THz radiation in biological tissues. It is believed that the aberrant overgrowths and proliferation of cells inside skin cause skin cancer[24]. There are already several studies which explore the feasibility of THz imaging for skin cancer diagnosis. Firstly, Woodward et al. demonstrated that THz measurements can be used for the diagnosis of basal cell carcinoma *in vitro* and observed the differences in the THz pulse shape for healthy and diseased skin[3]. Wallace et al. then conducted a spectroscopy study calculating the optical indices of healthy and basal cell

carcinoma skin and observed a contrast. The increased refractive index and absorption coefficient for basal cell carcinoma tissue was attributed to the higher water content in the abnormal tissues[30]. However, water content inside tissue is not the only source of contrast between healthy and abnormal tissues in the THz regime. Dehydrated tissue samples also show that morphological differences will lead to contrast in the images of tissues[31,32].

For skin cancer diagnosis, determining tumor margins is very important to aid the excision of diseased tissues. Wallace et. al have shown that THz imaging could be a potential technique to identify diseased regions both ex vivo and in vivo[33]. As shown by Fig.1. 4, the histology results and THz images correspond well. Fig.1. 4 (a) is an image of the THz amplitude in time domain at time t. The red area in Fig.1. 4 (a) corresponds to the cancerous region which can also be observed in the histological result shown in Fig.1. 4 (b) and is marked by the black horizontal line. Moreover, the THz image can reveal not only the tumor margins, but also resolve depth information. This is illustrated by Fig.1. 5 (a), where the minimum amplitude in a THz pulse response is plotted, this figure shows the surface information of a nodular basal cell carcinoma tissue. And by plotting the THz amplitude at time t=2.8 ps, they are able to reveal the tumor extent at 250 μm depth into the skin as shown by Fig.1. 5 (b).

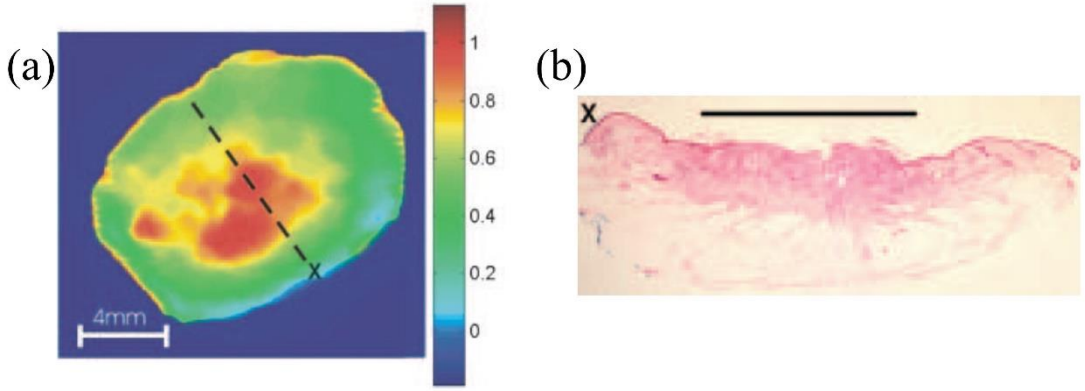

Fig.1. 4 (a) THz image (b) vertical histology section of the dashed line in (a).

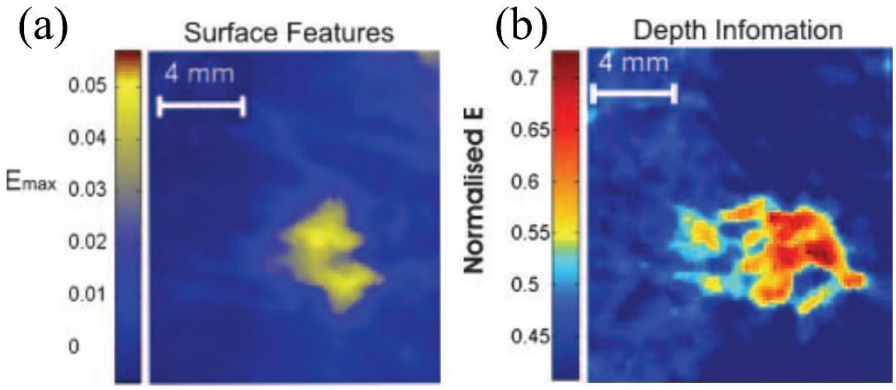

Fig.1. 5 (a) THz image of surface feature plotted by the minimum values of amplitude of a THz pulse (b) THz image of depth information plotted by the amplitude of a THz pulse at t=2.8 ps.

1.3.3. THz imaging for other skin applications

Given that both water content and structure changes of tissue will lead to differences in the optical properties, there are also other applications, such as evaluation of burns, scars, hydration inside skin and transdermal drug delivery. Taylor et al. imaged porcine skin burns and successfully demonstrated that healthy and burnt skin have different reflectivities at THz frequencies[34]. They also demonstrated that THz reflective imaging is able to detect and visualize edema in rat model[35]. Further studies by their group show that by monitoring hydration changes of tissue, THz imaging is able to assess the viability of tissue

flaps. Moreover, they also employed THz sensing to probe human cornea hydration[36]. Fig.1. 6(a) shows the THz imaging setup to conduct *in vivo*, non-contact measurement of human cornea. Their experiment on a drying porcine eye demonstrated the sensitivity of THz imaging for the cornea hydration. Fig.1. 6(b) shows the normalized reflectivity image of the *in vivo* human cornea. Fan et al. further demonstrated that a scar that is invisible to the naked eye can be seen by THz radiation and monitored the scar healing process by THz imaging[4]. Hernandez-Cardoso et al. employed THz imaging to detect the early stages of diabetic foot syndrome based on changes in the water content[37]. Fig.1. 7 shows the image of the water content of a diabetic foot and a healthy foot and the diabetic foot tends to have lower water content compared to healthy foot due to the deterioration. Moreover, works by Kim et al. show that THz reflection imaging is able to monitor the topical application of ketoprofen and dimethyl sulfoxide (DMSO) mixtures and demonstrated the feasibility of using THz imaging to evaluate the concentration of these solutions in the skin and penetration depth of the drugs[38,39]. However, all these works are based on the sensitivity of THz radiation to fluidic shift inside tissues. As has been mentioned above, the structural differences of tissues will also lead to contrast of THz spectrums. Therefore, exploring the capability of THz imaging for sensing structural changes in skin can further broaden the application of THz skin imaging[31,32].

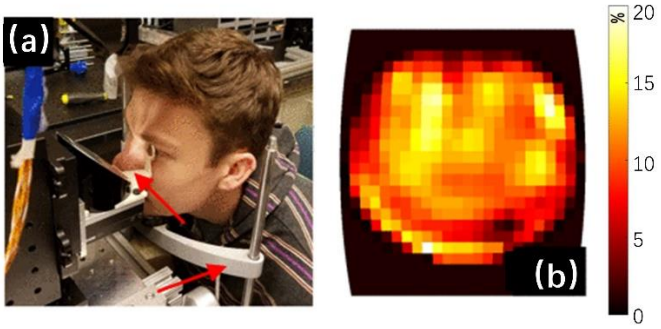

Fig.1. 6 (a)THz imaging setup to conduct in vivo, non-contact measurement of human cornea (b) reflectivity image of human cornea[36]

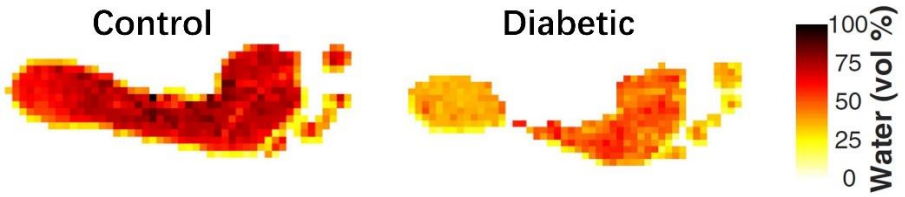

Fig.1. 7 Water content imaging of a healthy foot and the foot of a subject with diabetes[37]

1.4 Thesis overview

As described above, both tissue hydration and structural changes will lead to changes in the optical properties of tissues in the THz regime. In Chapter 2 of this thesis, we will introduce the THz imaging technique, the approach used to extract the optical indices and the skin models applied in the THz regime. In Chapter 3, we examine the parameters that affect in vivo measurements of the skin performed using THz imaging and a proposed protocol to eliminate variation between measurements. In Chapters 4 and 5 we apply THz imaging to evaluate silicone gel sheet treatment and transdermal drug delivery. In Chapter 6, we describe the application of an ellipsometry method to measure the anisotropic properties of the skin. And Chapter 7 presents a summary of this thesis.

2. THz imaging technique and related theory

2.1. THz generation

D. H. Auston introduced photoconductive antennas to generate and probe THz pulses in 1975[40] which is what we used for measurements in this thesis. Illustrated in Fig. 2. 1, a pair of metal electrodes patterned on a semiconductor wafer (GaAs or InGaAs) is used for the generation of THz pulses[41]. When a femtosecond pulse, with photon energy greater than the bandgap of the semiconductor, is pumped onto the photoconductive antenna, excited free electron-hole pairs form and recombine due to the biased voltage between the electrodes. This will induce a quick generation and vanishment of current and therefore causes an electromagnetic wave with frequency in THz regime.

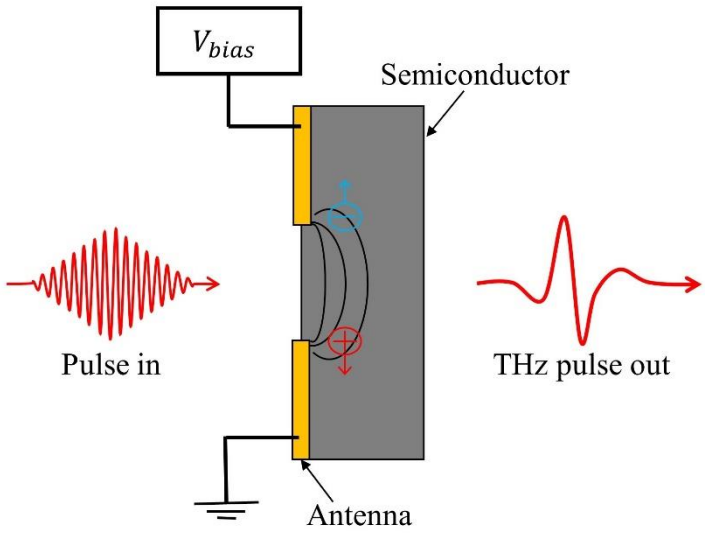

Fig. 2. 1 Illustration of THz pulse generation by photoconductive antenna

There are also other techniques for generating THz radiation. Based on the susceptibility of certain crystals (ZnTe), time-varying polarization is produced upon the incidence of the pumping light and induces the emission of a THz pulse.

This so called optical rectification can achieve emission of higher frequency ranges[42] but requires a high-power (GW/cm^2) pumping laser[43]. By utilizing an oscillation cavity, vacuum electronic devices can convert the kinetic energy of electrons to THz radiation. However, a small cavity is needed for the generation of THz radiation[44]. By exciting molecules with a transition band gap in the THz regime, a gas laser is able to emit THz light. However, this method is not continuously tunable due to transition band gaps between rotational modes not continuous. Quantum cascade lasers are also attracting interest for the generation of THz radiation. Despite the low operating temperatures, using the electron transition between intersubbands this method can give high power THz radiation with good flexibility because quantum cascade lasers can act as emitter and detector simultaneously[45].

2.2. THz Detection

Photoconductive antenna based detectors similar to the photoconductive antennas used for THz generation is what we use to measure THz radiation in this thesis. Illustrated in Fig. 2. 2, instead of having a bias voltage as in the emitter, a current detector is employed to detect THz radiation. The femtosecond laser pulse here works as the probing pulse which excites free electron-hole pairs in the semiconductor, these carriers are accelerated under the incoming THz electric field causing a current change to be detected. However, the femtosecond probing pulse can only detect the current induced by the instantaneous THz electric field.

Therefore, an optical delay stage is needed to change the arrival time of probing pulse.

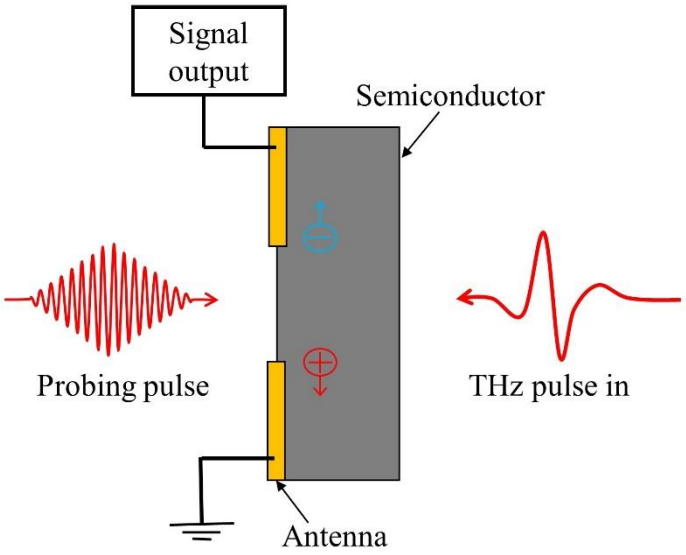

Fig. 2. 2 Illustration of THz pulse detection by photoconductive antenna

Materials that convert electromagnetic energy to thermal energy can convert incoming THz waves into electric signals[46]. However, these thermal based detectors usually represent only the intensity without phase information and therefore are not suitable for spectroscopy. By mixing and analyzing the detected THz wave with a reference THz wave, heterodyne detectors offer a high sensitivity, broad bandwidth option[47].

2.3. THz systems

In general, THz imaging systems can be divided into two catalogues: THz pulsed imaging (TPI) systems and continuous wave(CW) systems. Though CW system can be made low-cost, it usually contains intensity information with a narrow spectrum. Therefore, limited information can be provided by CW systems. Based on THz time-domain spectroscopy (THz-TDS), TPI systems are able to record THz

waveforms in the time-domain, providing both intensity and phase information. The waveform can then be Fourier transformed to extract the frequency domain spectra. By raster scanning the sample, TPI systems are able to acquire 2D images. Together with the time-domain waveform information, depth information is also provided. Therefore, 3D images can also be acquired. In the following paragraph, the TPI system we used for measurements is introduced.

As explained in Chapter 1, due to the high attenuation of THz waves in biological samples, *in vivo* measurements of skin are usually conducted in a reflection geometry. Fig. 2. 3 illustrates a typical TPI system (Menlo TERA K15) in reflection geometry which is also what we used in this thesis with SNR>90dB for the dynamic range. Fig. 2. 4 shows the photo when the Menlo TPI system is measuring the volar forearm of a subject. An imaging window is usually used to help place and align the sample. Both the emitter and detector in this system are based on photoconductive antennas which have been introduced respectively in Sections 2.1 and 2.2. The femtosecond fiber coupled laser (1560 nm, 100 mW) is split and directed into the THz emitter and detector and the laser passes through the delay stage before it reaches the detector. By moving the delay stage, the whole THz pulse carrying sample information can be acquired. By either moving the imaging window or the emitter and detector (including the lenses), 2D images of the sample or target area can be acquired. However, for in vivo studies, large increment may be caused by moving the imaging window. The later one is chosen for our work.

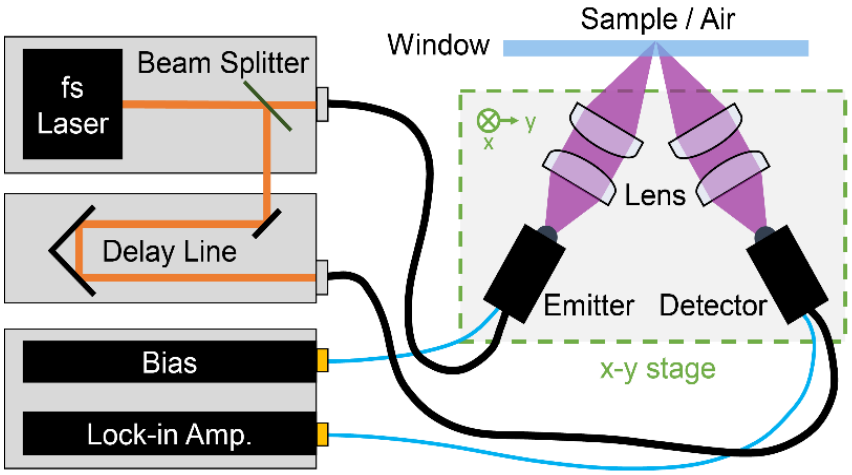

Fig. 2. 3 THz pulsed imaging system in reflection geometry

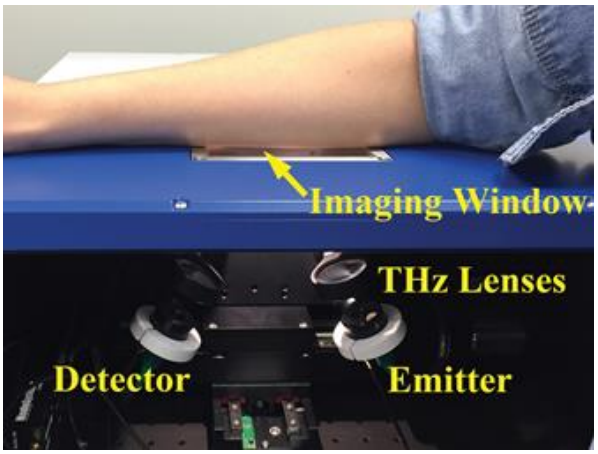

Fig. 2. 4 Menlo TERA K15 system in reflection geometry measuring the volar forearm

2.4. THz wave propagation

THz wave propagation in a medium can be described by the following equation:

$$E(z,t) = E_0 exp\left[i(wt - \frac{\tilde{n}w}{c}z)\right] \quad (2.\ 1)$$

where E_0 is the initial amplitude of electric field, $\tilde{n}$ is the complex refractive index of the medium, w is the angular frequency and $w=2\pi f$. c is the speed of light. z and t are the position and time respectively. The complex refractive index $\tilde{n}$ can also be written as:

$$\tilde{n} = n - ik \quad (2.\ 2)$$

where n is the refractive index of the medium, this describes the propagation process of the wave through the medium and k is the extinction coefficient, this describes the attenuation of THz waves inside the medium. The absorption coefficient is defined by $\alpha = 2wk/c$ and it describes how THz waves are attenuated with propagation distance. The above definition can be better understood when we rewrite Eq. 2. 1 as following:

$$E(z,t) = E_0 \exp(iwt) \cdot \exp\left(-\frac{kw}{c}z\right) \cdot \exp\left(-i\frac{nw}{c}z\right)$$
$$= E_0 \exp(iwt) \cdot \exp\left(-\frac{\alpha}{2}z\right) \cdot \exp\left(-i\frac{nw}{c}z\right) \quad (2.\ 3)$$

However, when we study the interaction of THz waves with a sample which in this thesis usually is skin tissue, THz waves are not simply propagated in a single medium. Therefore, THz wave propagation at an interface is introduced.

Assuming that THz waves propagate from medium 1 with complex refractive index and incident angle being $\tilde{n}_1$ and θ_1 to medium 2 with complex refractive index and incident angle being $\tilde{n}_2$ and θ_2 as shown in Fig. 2. 5, Snell's Law relates the incident, transmission and reflection angles and can expressed by the following equation:

$$\tilde{n}_1 \sin\theta_1 = \tilde{n}_2 \sin\theta_2 \quad (2.\ 4)$$

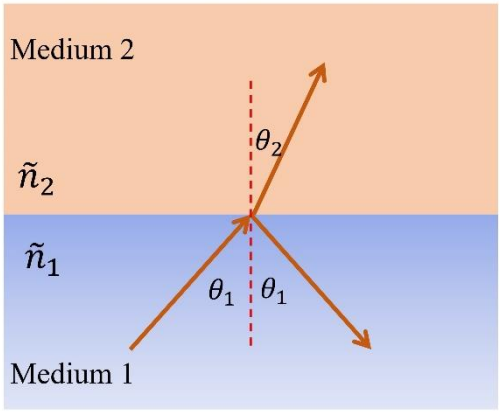

Fig. 2. 5 Illustration of the incident, transmission and reflection angles.

At the interface of the two media shown in Fig. 2. 5, the reflected electric field and the incident electric field follow the Fresnel Equations. For s-polarized and p-polarized light, the ratio between the reflected and incident electric fields can be written as Eq. 2. 5 and Eq. 2. 6 respectively. The ratio between transmitted and incident electric field for s-polarized and p-polarized light can be described by Eq. 2. 7 and Eq. 2. 8 respectively. Together with Eq. 2. 4, the Fresnel Equations and Snell's Law provide the possibility to extract the complex refractive index ($\tilde{n}_2$) of medium 2 with $\tilde{n}_1$ and θ_1 usually thought to be prior known

$$r_s = \frac{\tilde{n}_1 cos\theta_1 - \tilde{n}_2 cos\theta_2}{\tilde{n}_1 cos\theta_1 + \tilde{n}_2 cos\theta_2} \quad (2.\ 5)$$

$$r_p = \frac{\tilde{n}_2 cos\theta_1 - \tilde{n}_1 cos\theta_2}{\tilde{n}_2 cos\theta_1 + \tilde{n}_1 cos\theta_2} \quad (2.\ 6)$$

$$t_s = \frac{2\tilde{n}_1 cos\theta_1}{\tilde{n}_1 cos\theta_1 + \tilde{n}_2 cos\theta_2} \quad (2.\ 7)$$

$$t_p = \frac{2\tilde{n}_1 cos\theta_1}{\tilde{n}_2 cos\theta_1 + \tilde{n}_1 cos\theta_2} \quad (2.\ 8)$$

2.5. Data processing in reflection geometry

As discussed above, a reflection geometry system with a quartz imaging window is used during *in vivo* or *ex vivo* skin measurements to help place the sample or

target region reliably in focus and avoid phase uncertainty due to the uneven surface of skin Therefore, in the experimental setup, the THz light is reflected by the air-quartz and quartz-sample interfaces as shown in Fig. 2. 6. We define the first reflection from the air-quartz interface as the baseline and the baseline can be removed if we are able to measure the first reflection in isolation from the second reflection. This is done by putting another quartz window onto the first window to eliminate the second reflection. By subtracting the measured first reflection from the acquired response from the sample, the reflection from quartz-sample interface can be isolated as shown by Fig. 2. 7. We directly measured air in Fig. 2. 6., then by placing another quartz window on top of the imaging window, the baseline can be extracted shown by the black curve in Fig. 2. 7. Without eliminating the first reflection, two pulses are presented in the blue curve indicating the reflections from air-quartz and quartz-sample (air) interfaces. The red curve shows the reflection from quartz-sample interface alone which is obtained by subtracting the measured baseline.

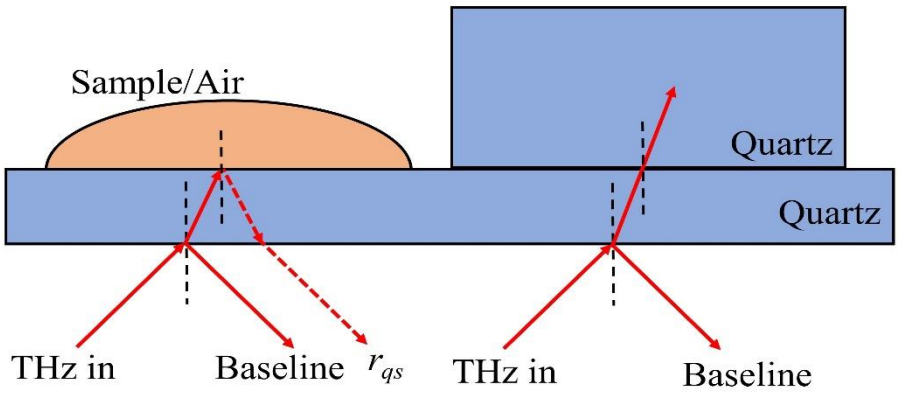

Fig. 2. 6 Illustration of the baseline measurement configuration.

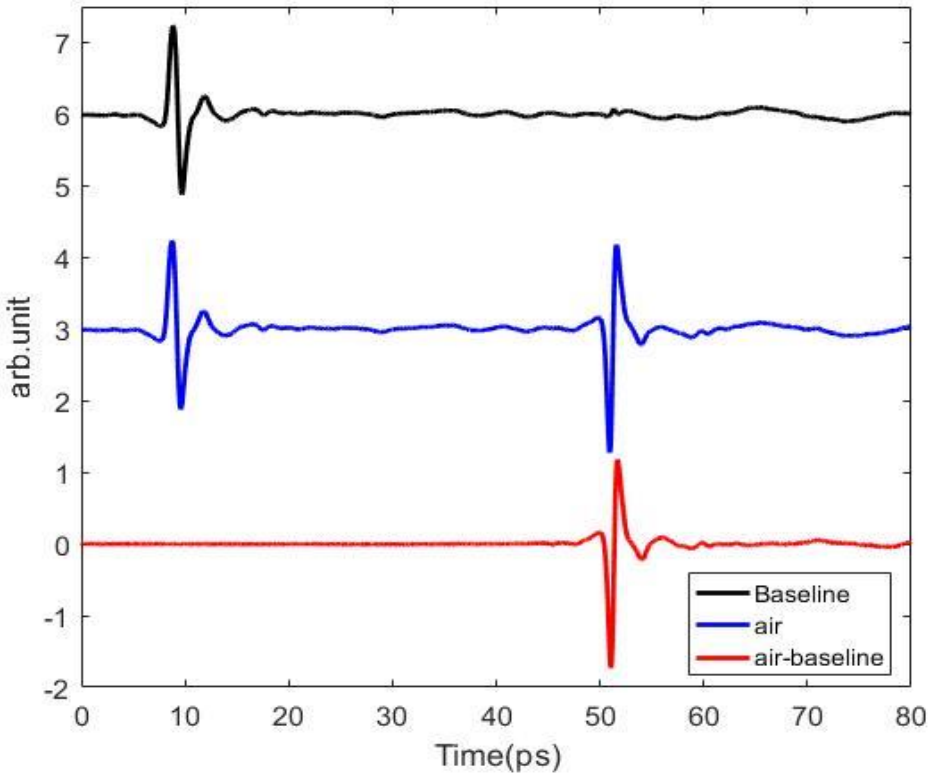

Fig. 2. 7 Illustration of the elimination of the baseline. Note that the pulse for baseline and air has been moved upward to avoid overlap of the pulses.

In THz spectroscopy, the signal from the sample under investigation and a reference signal from a sample with known properties are measured. Air is used as the reference here. THz-TDS measures the THz signal in time domain. By performing a Fourier transform, the signal is then converted to the frequency domain. The measured spectral ratio of the sample and reference signals is calculated by Eq. 2. 9, and we further remove low and high frequency noise in the processed signal using a band pass filter Eq. 2. 10. The reflectivity is calculated by Eq. 2. 11.

$$\mathrm{M} = \frac{FFT(E_{sample}(t) - E_{baseline}(t))}{FFT(E_{air}(t) - E_{baseline}(t))} \tag{2. 9}$$

$$\text{processed signal} = \mathrm{iFFT}[FFT(filter) \times M] \tag{2. 10}$$

$$reflectivity_{sample} = \left|r_{qs}\right|^2 = \left|r_{qa}M\right|^2 \quad (2.\ 11)$$

where r_{qs}, r_{qa} are the reflection coefficients at quartz-sample and quartz-air interfaces respectively, as calculated using Eq. 2. 5.

As has been introduced in Section 2.4, the Fresnel Equations and Snell's Law can be used for extracting the refractive index of samples. In this thesis, we used s-polarized THz waves to conduct measurements except where it is stated that p-polarized light was used. The spectral ratio for s-polarized THz waves can therefore be calculated using Eq. 2. 12.

$$M=\frac{r_{qs}}{r_{qa}} = \frac{\tilde{n}_q \cos\theta_q - \tilde{n}_s \cos\theta_s}{\tilde{n}_q \cos\theta_q + \tilde{n}_s \cos\theta_s} \cdot \frac{\tilde{n}_q \cos\theta_q + \tilde{n}_a \cos\theta_a}{\tilde{n}_q \cos\theta_q - \tilde{n}_a \cos\theta_a} \quad (2.\ 12)$$

Where $\tilde{n}_q$, $\tilde{n}_a$, $\tilde{n}_s$, are the complex refractive indices of quartz, air and the sample respectively, the sample is usually skin in this thesis, and θ_q, θ_a, θ_s, are the incident angles in quartz, air and the sample. Incident angles in different media can be related by Snell's Law as shown in Eq. 2. 13.

$$\tilde{n}_q \sin\theta_q = \tilde{n}_a \sin\theta_a = \tilde{n}_s \sin\theta_s \quad (2.\ 13)$$

With $\tilde{n}_s$ being the only unknown value, Eq. 2. 9 and Eq. 2. 12 can be equated to give the analytical solution presented in Eq. 2. 14 and Eq. 2. 15.

$$\tilde{n}_s = \sqrt{X^2 + {\tilde{n}_q}^2 \sin^2\theta_q} \quad (2.\ 14)$$

$$X = \frac{(1+M)\tilde{n}_a\tilde{n}_q \cos\theta_a \cos\theta_q + (1-\mathrm{M}){\tilde{n}_q}^2 \cos^2\theta_q}{(1+\mathrm{M})\tilde{n}_q \cos\theta_q + (1-\mathrm{M})\tilde{n}_a \cos\theta_a} \quad (2.\ 15)$$

Note that the skin studies throughout this thesis ignore the scattering effect due to the furrows on skin surface based on the simulation result in reference[48]. By considering the furrows on skin surface as a periodic structure with triangle feature, the scattering effect at 1 THz is negligible under different configurations.

But if the frequency goes higher, the scattering effect can be more pronounced and the Rayleigh roughness factor needs to be considered as shown in reference[49].

2.6. Skin models

2.6.1. Dielectric models

Aside from simply regarding the skin as a one-layer homogenous medium, there are also other studies which employ different models of the skin to study the interactions of THz waves with biological tissues. Truncated from the Debye model, the double Debye model was first used to study the permittivity of liquid water. Because of the high water content inside the skin, this model has subsequently been used for studying the THz dielectric response of human skin. The double Debye model is shown in the following form:

$$\tilde{\varepsilon}_r(w) = \varepsilon_\infty + \frac{\varepsilon_s - \varepsilon_2}{1+jw\tau_1} + \frac{\varepsilon_2 - \varepsilon_\infty}{1+jw\tau_2} \quad (2.16)$$

where ε_∞ is the limiting permittivity at high frequencies and ε_s is the static permittivity at low frequencies, ε_2 is the transitional permittivity at intermediate frequencies and τ_1 and τ_2 represent the relaxation times of the slow and fast relaxation processes corresponding to the breaking and reorientation of hydrogen bonds and the movement to a new tetrahedral site respectively. Together ε_∞, ε_s, ε_2, τ_1 and τ_2 are the five double Debye parameters.

Pickwell et al. modeled human skin using the double Debye model and simulated the THz response of the human forearm and palm tissues [50,51]. The simulated pulses obtained with this model fit well with the measured impulse functions from

the volar forearm and human palm, as illustrated in Fig. 2. 8. This model was then applied to non-melanoma skin cancer classification and high correlation between the double Debye parameters and the presence of skin cancer is observed[52]. However, regarding skin as a one-layer, homogeneous medium is an over-simplification and does not accurately represent human skin[51]. In order to include higher frequencies (up to 2 THz), additional terms should be added to the model to account for resonant Lorentzian processes[53]. This increases the complexity and difficulty of extracting the Debye parameters. Moreover, it is of more interest whether a model reflects the biological properties of the skin, such as the hydration levels inside the skin, which the double Debye model cannot do. The low water content of the human SC also raises questions as to the suitability of the double Debye model for describing the behavior of THz waves inside the SC.

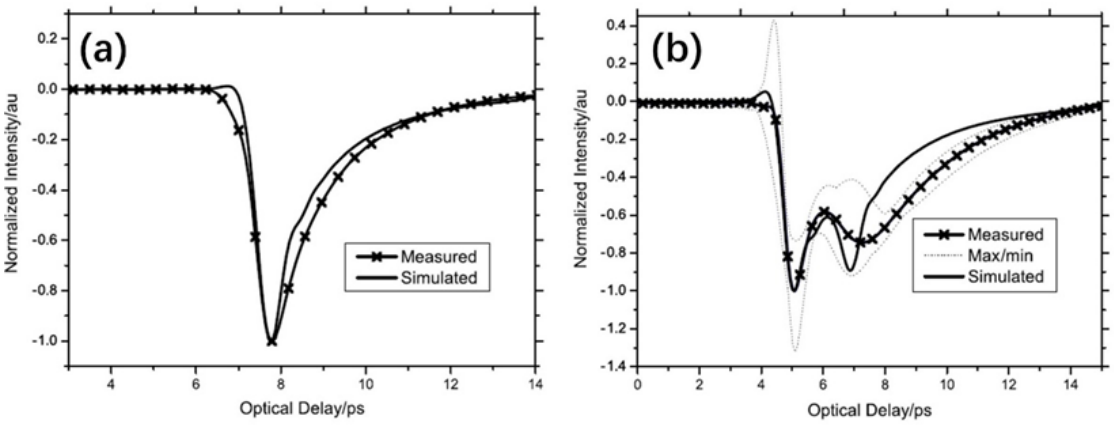

Fig. 2. 8 Measured and simulated impulse functions of (a) the volar forearm and (b) the palm

Effective medium theory (EMT) is used to model THz radiation in a composite system[54]. Many studies have used this theory to evaluate the water content inside biological phantoms and tissues[55]. The Bruggeman and Landau, Lifshitz,

Looyenga (LLL) models are the EMTs mainly used for THz biological applications to estimate hydration in plants and biological tissues[32,56]. In these models, skin is regarded as a composite of dehydrated skin and water. The permittivity of water and dehydrated skin can be measured beforehand and known. By varying the water content to obtain the best fit between the calculated permittivity of the composite system and the measured permittivity of skin, the water concentration can be determined. The Bruggeman model considers the skin to be composed of spheres of dehydrated biological tissues embedded in water, Eq. 2. 17 shows how this approach can be used to extract the permittivity of the system from the permittivity of the individual components:

$$\sum_{k=1}^{n} p_k \frac{\varepsilon_k - \varepsilon_{eff}}{\varepsilon_k + 2\varepsilon_{eff}} = 0 \quad \left(\sum_{k=1}^{n} p_k = 1\right) \tag{2. 17}$$

where p_k and ε_k are the volume percentage and permittivity of the k th component and ε_{eff} is the effective permittivity of the composite system.

However, other studies used the LLL model which allows the dehydrated biological tissues to take an arbitrary particle shape. The LLL model is shown in Eq. 2. 18:

$$\sqrt[3]{\varepsilon_{eff}} = \sum_{k=1}^{n} p_k \sqrt[3]{\varepsilon_k} \quad \left(\sum_{k=1}^{n} p_k = 1\right) \tag{2. 18}$$

Many papers have utilized this theory to estimate the water content inside biological tissues including skin. Dehydrated porcine tissue was measured by He et al. and this result was used to extract the water content inside different types

of tissues with the LLL model. The fitted and measured permittivities agree well with one another, as shown for skin in Fig. 2. 9 (a)-(b). The estimated water volumes obtained are consistent with values found in the literature[32]. From their fitting result, we can conclude that the LLL model can represent the permittivity of skin relatively well.

Hernandez-Cardoso et al. utilized the LLL model and THz imaging for the early diagnosis of diabetic foot syndrome, by observing the differences in the water content of the feet of diabetic and non-diabetic subjects [37]. As shown in Fig.1. 7, the foot of the subject with diabetic foot syndrome had significantly lower water content compared to that of healthy subject. Significant differences between the hydration of the feet of subjects in the control and the diabetic groups were found by conducting a quantitative analysis of the results from 33 subjects.

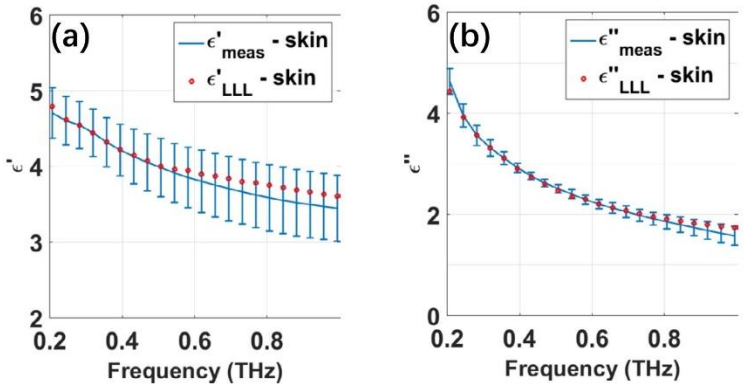

Fig. 2. 9 (a) Real and (b) Imaginary part of the skin permittivity[32].

However, to accurately estimate the water content of tissues using EMT, it is important to accurately extract the refractive index of dehydrated skin [32,37,49]. Thus, different measured results from references[32,37,49] for the refractive

indices and extinction coefficients of dehydrated skin are plotted and compared to those of measured water in Fig. 2. 10. As shown by the figure, the refractive index of dehydrated skin is less frequency dependent than that of water, which also indicates that the frequency dependence of skin mainly comes from the large component of water in the skin. The differences in the measured properties of dehydrated skin mainly come from the variation in the types of skin used and the dehydration process, as reference[37] used human biopsies and the other two references[32,49] used porcine skin with ethanol followed by air drying and heating to remove water respectively.

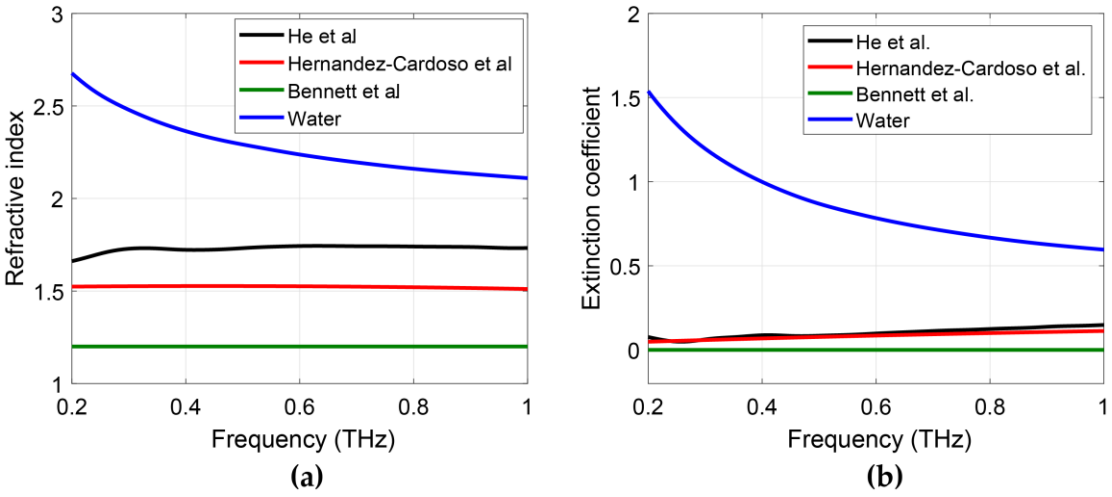

Fig. 2. 10 (a) Refractive index of dehydrated skin and water (b) Extinction coefficient of dehydrated skin from He et al. [32], Hernandez-Cardoso et al. [37] and Bennett et al.[49] and water

2.6.2. Structural models

THz radiation penetrates around 100 μm into the skin, meaning that it will reach as far as the dermis layer according to the skin structure introduced in section 1.3.1. Regarding skin as a one-layer homogeneous medium it is possible to simply use the method described in section 2.5 to extract the optical indices of skin.

A 2–layer model of the skin is proposed in this thesis to account for the contrast in water content between the SC which has a low water content and the epidermis and dermis layers which have higher water contents. The basic idea of the 2-layer model will be introduced in this section and is further employed to study the dynamic changes in water distribution in the skin in Chapter 4. However, it has been observed with Confocal Raman Spectroscopy that there is a water gradient inside the skin[57]. Instead of modelling the skin as one or two homogenous layers, a multilayer structure is also used to better mimic the real situation and study the structural changes of skin in this thesis. This multi-layer model will be introduced in this section and be employed in Chapter 3.

In the 2-layer model, skin is regarded as a two-layer structure by assuming a constant water content in the epidermis and dermis layers [15]. An effective medium theory (LLL model in Eq. 2. 18) is used to relate the complex refractive index to the water concentration in each layer as shown in Eq. 2. 19. By applying the Fresnel equations to a three-layer interface, the reflection coefficient for a quartz-SC-epidermis interface can be calculated, shown in Eq. 2. 20.

$$\tilde{n}_i = f_1(p_i) \tag{2. 19}$$

$$r_{qse} = \frac{r_{qs}+r_{se}\,exp(-i2\beta)}{1+r_{qs}r_{se}\,exp(-i2\beta)} \tag{2. 20}$$

where p_i represents the water volume in the i th layer and r_{qs}, r_{se} stand for reflection coefficients of the quartz-SC and SC-epidermis interfaces and can be calculated from Eq. 2. 5. β is given by $\beta = 2\pi d_s \tilde{n}_s cos\theta_s/\lambda$. $\tilde{n}_s$ and θ_s are the

complex refractive index and incident angle in SC and d_s is the thickness of the SC. The incident angle θ in each layer can be related to the refractive index by Snell's Law (Eq. 2. 13). r_{qse} is then divided by reflection coefficient for a quartz-air interface (r_{qa}) obtained by Eq. 2. 5 to derive the sample to reference reflection ratio as illustrated in Eq. 2. 21. Note that p_i has two terms in this case being water volume in SC and epidermis. This obtained reflection ratio, which is expressed as a function of the water concentration in the SC and epidermis layers and SC thickness, is then fitted to the measured reflection ratio (Eq. 2. 9) in the frequency domain.

$$M_{cal} = \frac{r_{qse}}{r_{qa}} = f_2(p_i, d_s) = M_{meas} \quad (2.\ 21)$$

As has been observed with Confocal Raman spectroscopy, the water concentration in the skin varies with depth [57]. Bennett et al. propose a multi-layer model to describe the water gradient in the skin, they call this model the stratified media model. This model simplifies the water concentration in the SC and epidermis to be a linear function with depth while the water concentration in the dermis is constant as shown by the blue dashed curve in Fig. 2. 11. Therefore, the water gradient inside the skin can be represented by the following five skin parameters: the thickness of the SC (d_1) and epidermis (d_2) and the hydration of the SC (H_0), epidermis (H_1) and dermis (H_2). The linear gradient of water inside the skin is then separated into multiple discrete layers and the continuous water gradient is then approximated by the red solid curve. Based on the water gradient

in each layer, the permittivity of each layer (ε_m) is determined using the water concentration (p_i) and EMT (Eq. 2. 17) shown in Eq. 2. 22.

$$\varepsilon_m = f_3(p_i) \tag{2. 22}$$

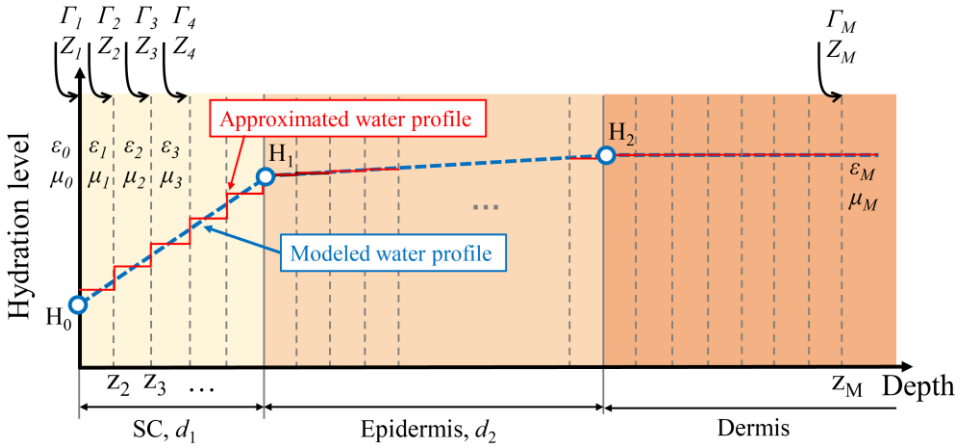

Fig. 2. 11 Water profile in skin and setup for the derivation of the reflection of a plane wave by a slab of stratified permittivity and permeability

Fig. 2. 11 shows the multi-layer model of the skin where the impedance (Z_m) and reflection coefficient (Γ_m) of each pair of adjacent layers are related by the iteration equations (Eq. 2. 23, Eq. 2. 24) where the longitudinal propagation constant(k_m) and characteristic impedance (ζ_m^{te}) is related to the permittivity (ε_m), the permeability (μ_m) and incident angle (θ) of each layer by Eq. 2. 25 and Eq. 2. 26 [49]. t_m and z_m are the layer thickness and skin depth at corresponding layer. Therefore, the reflection coefficient at the skin surface can be determined using the five skin parameters mentioned above. Fig. 2. 12 shows a detailed flowchart explaining the application of the stratified media model to extract the water gradient inside skin.

$$Z_m = \zeta_m^{te} \frac{Z_{m+1} + j\zeta_m^{te} \tan(k_m t_m)}{\zeta_m^{te} + jZ_{m+1} \tan(k_m t_m)} \tag{2. 23}$$

$$\Gamma_m = \frac{Z_{m+1} - \zeta_m^{te}}{Z_{m+1} + \zeta_m^{te}} e^{-2jk_m z_{m+1}} \tag{2. 24}$$

$$k_m = w\sqrt{\varepsilon_0\mu_0}\sqrt{\varepsilon_m - sin^2\theta} \quad (2.\ 25)$$

$$\zeta_m^{te} = \frac{w\mu_m}{k_m} \quad (2.\ 26)$$

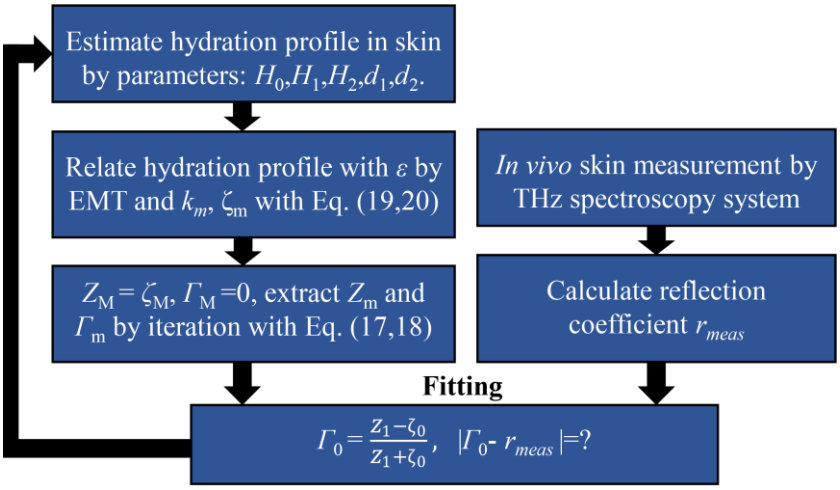

Fig. 2. 12 Flowchart of the application of the stratified media model to extract the water gradient in the skin

To understand how each parameter affects the THz pulses, we artificially assigned different values of one parameter with other parameters being constant to see the robustness or sensitivity of individual parameters in affecting the outcome. With H_1=0.7, H_2=0.8, d_1=20μm, d_2=70μm, Fig. 2.13 (a) shows the pulse shape changes under different values of H_0. We observed that by increasing the value of H0 from 0.01 to 0.7, the amplitude significantly decreased and a broadening effect is observed which refers to the time difference between the lowest valleys of the pulse increases. However, with H_1 changing from 0.5 to 0.8, the THz pulse did not change much, shown in Fig. 2.13 (b). However, THz pulse is more sensitive to H_2 changes. Illustrated in Fig. 2.13(c), with H_2 increasing from 0.6 to 1, the pulse peak decreased significantly. However, in reality H_2 will be more constant and will not reach as high as 100% water. Fig. 2.13(d) and (e) shows the

sensitivity of d_1 and d_2. From Fig. 2.13(d), with d1 increasing from 1μm to 40μm, the amplitude of THz pulse increased significantly and the time difference between the two valleys decreased. However, THz pulses are almost not affected by d_2 shown in Fig. 2.13(e) with d_2 increasing from 30 to 95μm.

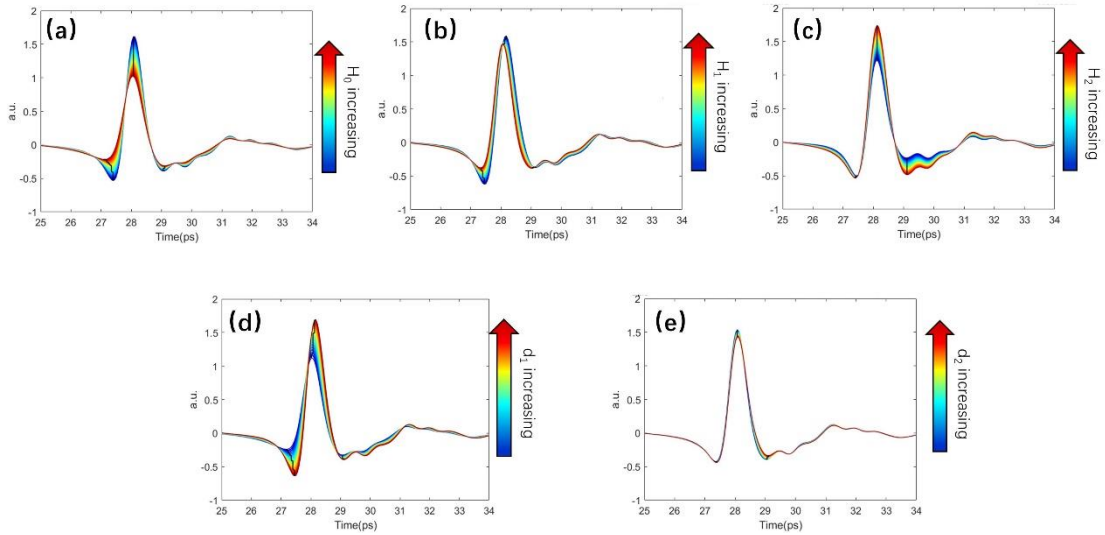

Fig. 2. 13 Test of the sensitivity of each parameter. (a) H_0 changes from 0.01 to 0.7, H_1=0.7, H_2=0.8, d_1=20μm, d_2= 70μm (b) H_1 changes from 0.5 to 0.8, H_0=0.2, H_2=0.8, d_1=20 μm, d_2=70μm (c) H_2 changes from 0.6 to 1, H_0=0.2, H_1=0.6, d_1=20μm, d_2=70μm (d) d_1 changes from 1μm to 40μm.H_0=0.2, H_1=0.7, H_2=0.8, d_2=70μm (e) d_2 changes from 30μm to 95μm, H_0=0.2, H_1=0.7, H_2=0.8, d_1=20μm. Note that the pulses are derived by inverse Fourier Transform with the pulse for reference known.

Though not mentioned in the aforementioned literature, there is also another way to model the multilayer structure of skin using the Fresnel equations. Similar to the two-layer model mentioned above, using the Fresnel equations can also yield the reflection coefficient for a multilayer structure. As shown in Fig. 2. , it is assumed that skin is a structure comprised of N layers each with the same thickness and that the water concentration after the N th layer does not change with depth. The imaging window used here is a quartz window with n=2.12. Thus, using an EMT, the complex refractive index ($\tilde{n}_m$) of each layer can be calculated

based on the water concentration gradient. The reflection coefficient of the surface can be calculated using Eq. 2. 27 , while the reflection coefficient of two consecutive layers is given by Eq. 2. 28 and the phase variation β_m is given by Eq. 2. 29 where d_m, $\tilde{n}_m$, θ_m, and λ are the thickness, complex refractive index and incident angle of m th layer and wavelength of the incident light. Therefore by iteration, the reflection coefficient from the m th layer can be calculated using Eq. 2. 30. The reflection at skin surface can thus be calculated.

$$R_{\text{N-2}} = \frac{r_{N-2,N-1}+r_{N-1,N}\,exp(-i2\beta_{N-1})}{1+r_{N-2,N-1}r_{N-1,N}\,exp(-i2\beta_{N-1})} \tag{2. 27}$$

$$r_{\text{m,m+1}} = \frac{n_m\,cos\,\theta_m - n_{m+1}\,cos\,\theta_{m+1}}{n_m\,cos\,\theta_m + n_{m+1}\,cos\,\theta_{m+1}} \tag{2. 28}$$

$$\beta_m = 2\pi d_m \tilde{n}_m cos\theta_m/\lambda \tag{2. 29}$$

$$R_m = \frac{r_{m,m+1}+R_{m+1}\,exp(-i2\beta_{\text{m+1}})}{1+r_{m,m+1}R_{m+1}\,exp(-i2\beta_{m+1})} \tag{2. 30}$$

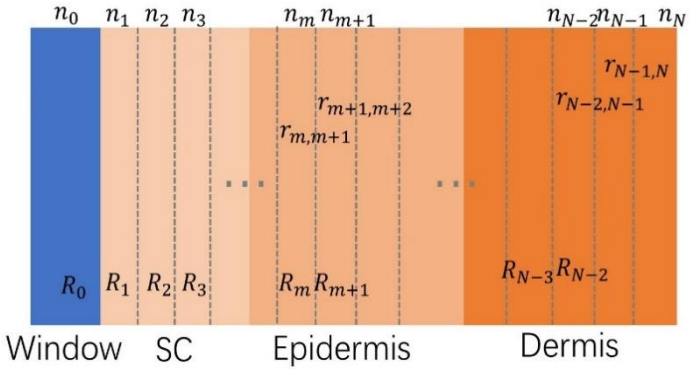

Fig. 2. 14 Diagram of the calculation of surface reflection coefficient

For comparison, we have calculated the reflection coefficients of a skin phantom with the same assumed water gradient in contact with a quartz window based on the Fresnel equations and the stratified media model. The assumed water gradient is shown in Fig. 2. (a). The reflection coefficients calculated by the above two theories are consistent with one another as shown by Fig. 2. (b).

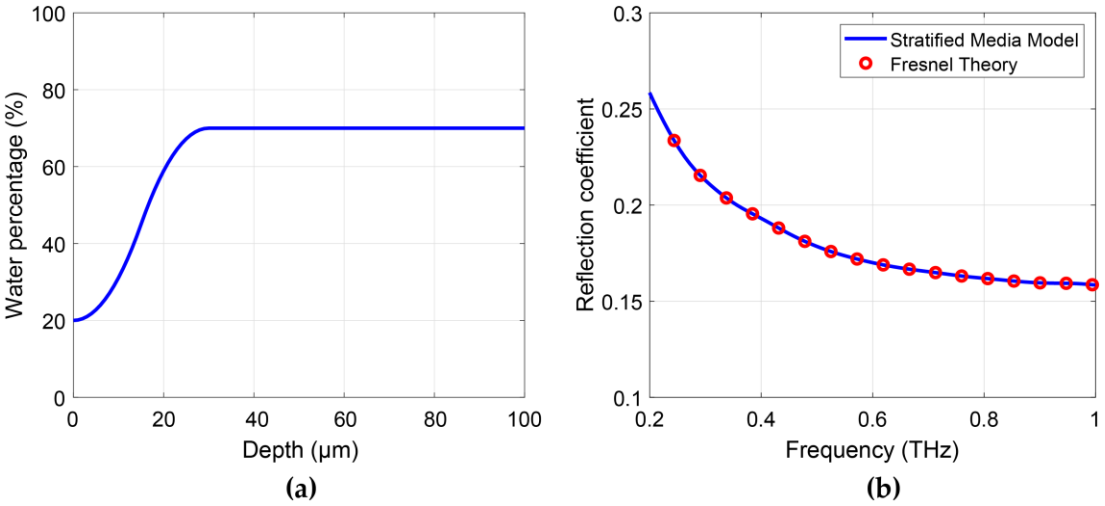

Fig. 2. 15 (a) Assumed water gradient (b) Calculated reflection coefficients at the skin surface using the stratified media model and Fresnel theory.

2.7. Summary

In this chapter, basic theory employed in the thesis is introduced including THz generation, detection and THz-TDS system. Wave propagation at an interface is also introduced. There are multiple models can be employed to study THz-skin interaction including dielectric models and structural models. The dielectric models can be used to extract physical properties with no prior knowledge needed. However, structural models can be used to study skin hydration and can be interpreted in a straightforward way.

3. Variables affecting *in vivo* skin measurements

3.1. Introduction

To enable THz techniques to be used in real life, *in vivo* skin studies are of vital importance. However, *in vivo* human skin studies are a lot more complicated than *ex vivo* studies due to the potential for dynamic changes in the region of interest or the movement of the subject throughout the measurement. Variables with the potential to affect measurements need to be carefully studied and taken into account. Robust protocols that can improve the repeatability of measurements and ensure consistent results are in high demand. Therefore, in this Chapter, parameters that affect THz *in vivo* skin measurements will be discussed with an emphasis on the effect of pressure and a recommended protocol for *in vivo* studies will also be briefly introduced.

3.2. Variables

Parameters that affect *in vivo* studies of skin in the THz regime include the skin type of subject, the experimental setup used and environmental changes such as the weather. The effect of different skin types is usually seen by the variation between subjects. Human skin is very diverse and changes with ethnicity, gender and age. Human skin of different ethnic types shows clear differences in structure and function[58]. It has been reported that Asian skin shows higher water content and SC lipid levels[58]. Aging skin shows decreased thickness of the epidermis [59], and is often characterized by roughness, dryness and wrinkling[60]. However,

there is no significant relation between gender and the measured properties of the skin. Slightly higher hydration levels in the female group was reported by Firooz et al. [61] while Ehlers et al.[62] and Wilhelm et al.[63] observed no correlation between skin hydration and sex.

Skin differences especially hydration will affect THz measurements and therefore ethnicity, aging, and probably gender will induce changes in the THz response of skin. A clear difference in the reflected THz pulse observed for the skin of Asian and Caucasian males has been demonstrated[64] as shown by Fig. 3. 1. The reflected pulse from the Caucasian male group shows clearly higher pulse peak, while the reflected pulses from left and right arm of the same subject do not show significant difference indicating that one of them could be used as the reference when studies conducting on the other arm. Peralta et al. observed the difference in the optical properties in the THz range during melanogenesis with *in vitro* skin models from Asian, Black, and Caucasian races[65]. Therefore, these factors may also need to be considered when conducting *in vivo* skin studies.

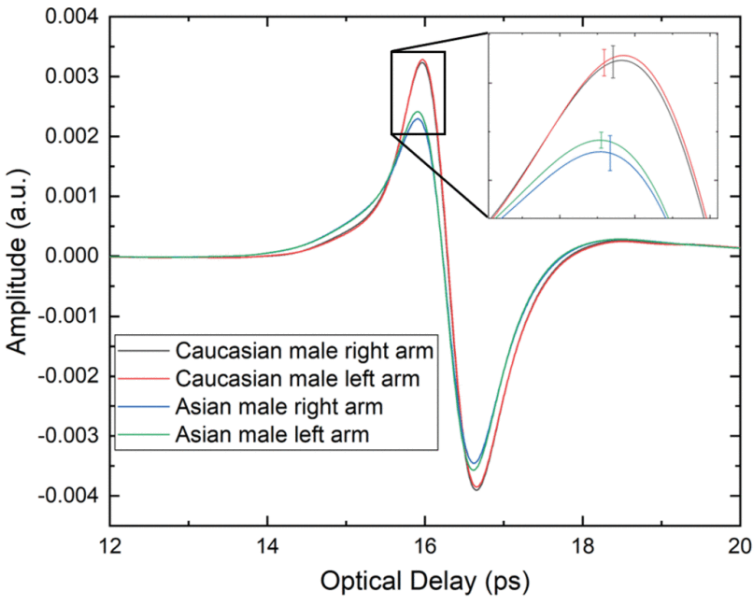

Fig. 3. 1 Averaged THz pulse reflected from volar forearm of Caucasian and Asian males. Note that each group has totally six subjects and the error bars are the standard deviation of the results from different subjects.

Moreover, the external environment will also affect skin conditions. For example, studies have observed the influence of the season on skin properties, such as hydration and sebum output[66]. Environmental humidity, temperature and additional washing will also induce changes in the skin barrier function and properties[67,68] while there is weak empirical evidence for a relationship between skin hydration and additional dietary water intake[69]. The mentioned variables above are usually difficult to eliminate and therefore careful control and consideration of them is another option.

3.2.1. Variables caused by experimental setup and measurement

However, changes and effects caused by the experimental setup and measurement routines can be minimized or removed with technical solutions. Therefore, in our *in vivo* skin measurements, variables including occlusion and

contact pressure are considered and the effects of them are minimized to ensure the consistency of measurements. Details will be discussed in sections 3.3 and 3.4 but a short explanation of these effects will be presented here. Due to the high absorption by water, *in vivo* THz measurements are usually performed using a reflection geometry. A quartz window is needed to obtain a reliable reference[70,71] and to fix and flatten the area of interest to minimize scattering effects, as illustrated in Fig. 2. 3. However, when the skin contacts the window, occlusion induced by the prevention of transdermal water loss and mechanical deformation will occur at the surface of the skin.

3.2.2. Occlusion

When skin is under steady state, water molecules can interact with the environment illustrated in Fig. 3. 2(a). However during *in vivo* THz measurements of skin, the skin is in contact with an imaging window and water molecules can no longer evaporate to the environment and therefore accumulate inside skin. This increases the hydration of the skin as illustrated in Fig. 3. 2(b). Previous studies by Sun et al. have shown how occlusion affects the THz response of skin[72]. In short, 20 minutes contact with the quartz window induces occlusion in the skin, thus increasing the water concentration and therefore affecting the THz response. The increased water concentration induces a decrease in the intensity of the reflected THz pulse. A biexponential model is also proposed to describe the trend in the THz amplitude induced by occlusion during the measurement and minimizes the effect of occlusion during the acquisition of an image using a raster

scan, as it usually takes several minutes to acquire a $2\,cm \times 2\,cm$ image with a resolution of 1 mm^2.

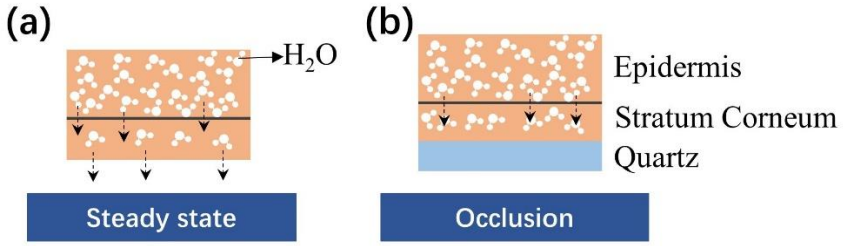

Fig. 3. 2 Illustration of water dynamics of skin under (a) steady state and (b) occlusion state

3.3. Introduction to pressure effects

During an *in vivo* measurement, slight pressure is usually applied to skin to fix the position and minimize the air gap between the quartz window and the skin. This however compresses the skin and mechanical deformation occurs. *In vitro* optical properties of skin under different pressures have been measured with a visible-IR spectrophotometer[73]. The sample is sandwiched between two glass slides allowing different pressures to be applied. They found that the tissue thickness and optical properties changed under different applied pressures. Reflectance increased under compression compared with no applied load. Clarys et al. showed that skin capacitance changes when pressure is applied[74].

To determine how pressure affects the THz response of skin, we measured a single point of the volar forearm under different applied pressures with a flat pressure sensor sandwiched between the forearm and the imaging window to indicate the local pressure. We observed the effect of pressure on the THz responses and applied a stratified media theory to model the skin and evaluate

changes under different pressures. We further explain the mechanism behind the effect of the contact pressure on the skin during *in vivo* THz measurements. However, it should be noted that we only studied the skin in the vertical direction (along skin depth).

3.4. Experimental setup and protocol

Details of the THz-TDS system has been introduced in Section 2.3 and the system enables us to record the THz response at a rate of 4 Hz, the experimental setup is illustrated in Fig. 3. 3(a). A THz pulse is produced by a photoconductive emitter[75] and the beam of radiation is focused on the upper surface of an imaging window where the area of interest on the subject's arm is placed, and the reflected signal is received by a photoconductive detector. An aluminium foil was put on the imaging window with a 20×20mm region cut out to maintain the correct position during each measurement. A flat pressure sensor (FSR 402), sandwiched between the area of interest and aluminium foil, was placed adjacent to the THz spot and target measurement area to indicate the local contacting pressure during the measurement as shown in Fig. 3. 3(c)- (d).

Before the experiment, each subject had a 20×20mm area on the volar forearm (2 to 5cm from the edge of the dorsal and the volar forearm and 5 to 10 cm away from the elbow) marked to make sure each measurement was performed on the same area. During the whole experiment, subjects were asked to keep the markers. Before the experiment, subjects were trained to apply five different

pressures ranging from $1.5N/cm^2$ to $3.5N/cm^2$. Each measurement lasted for 1 minute with only one pixel being measured. Four THz pulses were measured per second. For each pressure, we repeated the measured three times to make sure no special circumstances occurred which would cause changes. We additionally performed THz imaging to verify that observations were due to the pressure effect and not spatial variation of the skin. A one hour interval was left between each measurement of the volar forearm to eliminate the occlusion effect and let the area of interest recover back to its normal state. For data analysis, we use the THz pulses after the skin has been in contact with the window for 30 seconds to minimize the occlusion effect for different measurements as the most rapid changes in THz signals usually occur at the start of occlusion[72].

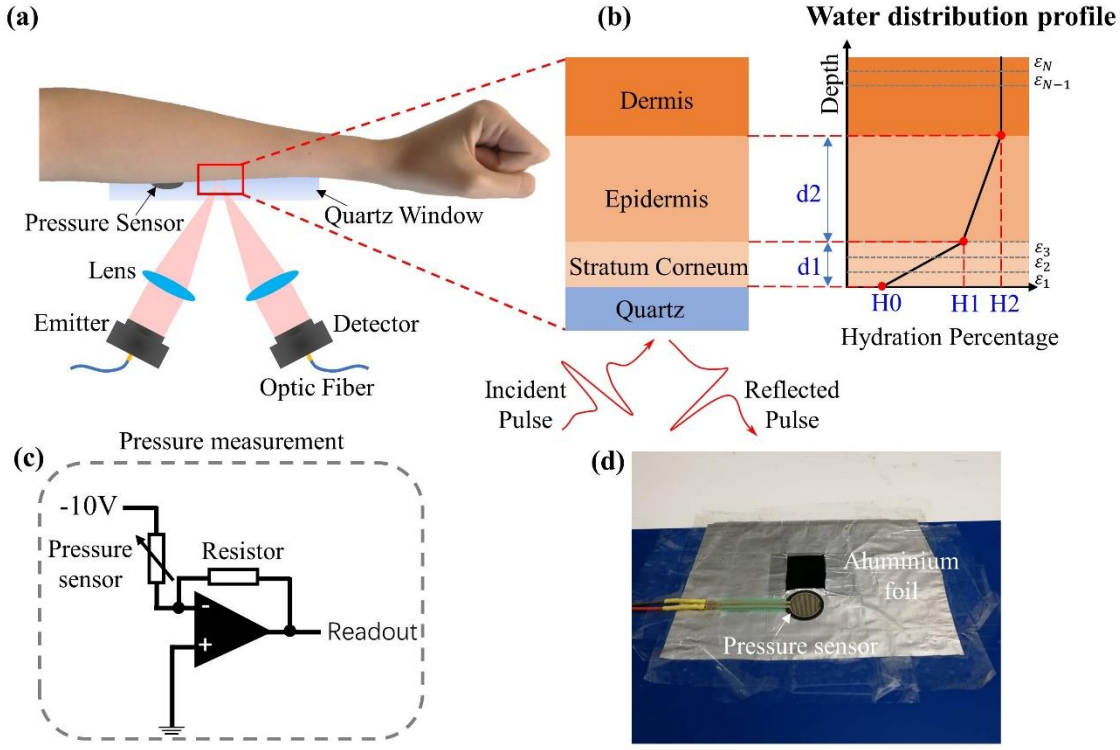

Fig. 3. 3 (a) Experimental setup (b) Skin structure and water profile inside skin (b) circuit for pressure measurement (d) the photo of the pressure installed setup

3.5. Data processing and modelling

The strong absorption of THz waves absorption by water restricts THz *in vivo* measurements to a reflection geometry. Therefore in our experimental setup for *in vivo* skin measurements, a THz wave is reflected by the air-quartz and quartz-sample interfaces. Details of the data processing for this geometry were discussed in Section 2.5, with Eq. 2. 9- Eq. 2. 15 being used to calculate the sample to reference ratio, impulse function, reflectivity, refractive index and extinction coefficient. The obtained optical indices in the frequency domain clearly show the trend caused by the pressure effect which will be detailed in the results section. However, regarding skin as a single-homogeneous layer is an over-simplification. To better understand the changes induced in the skin hydration and SC thickness, we employed the stratified media model which was introduced in Section 2.6.2.

Research into the structure of skin has shown that the water concentration in the SC can be simplified to a linear function which increases with depth, followed by a lower gradient in the epidermis and a constant in the dermis[49,76], as illustrated in Fig. 3. 3(b). In order to understand the mechanical deformation of skin under different pressures, we use a stratified media model which was introduced in Section 2.6.2 to calculate the reflectivity and find a fit to our measured results. For this, we use the stratified media model combined with the Bruggeman model to evaluate how the various skin parameters, such as skin hydration and SC thickness, change under different pressures. The full set of

equations for the application of the stratified media model can be found in Section 2.6.2, which gives the calculated surface reflectivity as following:

$$R_{cal} = \left| \frac{Z_{skin} - \frac{1}{\cos\theta_{quartz}} \sqrt{\frac{\mu_0}{\varepsilon_0 \varepsilon_{quartz}}}}{Z_{skin} + \frac{1}{\cos\theta_{quartz}} \sqrt{\frac{\mu_0}{\varepsilon_0 \varepsilon_{quartz}}}} \right|^2 \quad (3.\ 1)$$

where Z_{skin} is the impedance of skin and is calculated using the effective permittivity of skin and the stratified media model introduced in Section 2.6.2. Note, that θ_{quartz} and ε_{quartz} are values that can be known from the experimental setup used, in our case they were $\theta_{quartz} = 13.64^o$ and $\varepsilon_{quartz} = (2.12 - 0i)^2$. The fitting parameters of our proposed model are the water concentration at the surface of the SC, epidermis and dermis, the thicknesses of the SC and the epidermis, and finally the refractive index of dehydrated skin, see Fig. 3. 3(b) for illustration. Compared with what was discussed in Section 2.6.2, the refractive index of dehydrated skin is treated as an unknown variable in this model because we expect that the properties of dehydrated skin might also change due to the compression of skin. Current literature measuring the properties of dehydrated skin finds that the extinction coefficient is almost 0 [32,37,49]. By minimizing the difference between the measured and calculated reflectivities, given by Eq. 2. 11 and Eq. 3. 1 respectively, over the frequency range of 0.3 to 0.8 THz (the effective bandwidth of our THz-TDS system) the unknown parameters can be extracted.

However, our work has several limitations. The structure and properties of the skin will change with location and will vary between subjects. Though we applied

aluminum foil and marked the region of interest on the subject's arm, the position might still change a little. Another limitation is that we use a pressure sensor to measure the local pressure, however due to the reflection geometry used in this experiment, we cannot observe the pressure at the same point on the skin where the THz response is being measured. Instead, we put the sensor next to the region being measured. During the one minute measurement the applied pressure will fluctuate as it is hard for the subject not to move at all for one minute, which will also introduce an error into the results. Besides, the model used to extract the properties of the skin is only a method to help us understand the mechanisms behind the pressure effect, not a technique for directly observing these changes in the skin. In this work, we assume that the water concentration distribution increases linearly with depth in the SC and epidermis. In reality, it is not perfectly linear and with pressure applied to skin, the water distribution might change. However, this work still gives us important insights into the effect of pressure on the THz response of skin and the possible mechanisms behind this effect.

3.6. Results and discussion

3.6.1. THz response of skin under different applied pressures

Fig. 3. 4(a) shows the processed THz signals, obtained using Eq. 2. 10, under different pressures. The signals are temporally shifted by 0.5 ps for clarity. While the pulse shape did not change significantly, the peak to peak of the processed signal decreased with the increase of applied pressure. This indicates that the

reflectivity of skin decreases with increasing pressure, this is discussed further in section 3.6.2.

To ensure that the decreased peak to peak of THz pulse is due to the pressure and not due to spatial inhomogeneity of the skin, we also imaged a 10×16mm area of the volar forearm for one subject under different pressures with a 2×2 mm resolution. The results are shown in Fig. 3. 4(b) where the peak to peak of the processed signal is plotted in each pixel. The reduced peak to peak of the processed signal with increasing pressure, indicates that the trend described above in the point measurements is not due to spatial variation of the skin. Further, in Fig. 3. 4 (b) the observable decrease in the peak to peak values from left to right of the image is caused by the occlusion of the skin by the imaging window during the 36 seconds taken to acquire the image, as each image is acquired by raster scanning the THz spot in lines going from top to bottom and measuring the next line to the right. Therefore the skin measured on the right-side of the images have been occluded for more time than that on the left side, and therefore have lower values for the peak to peak of the processed signal[72].

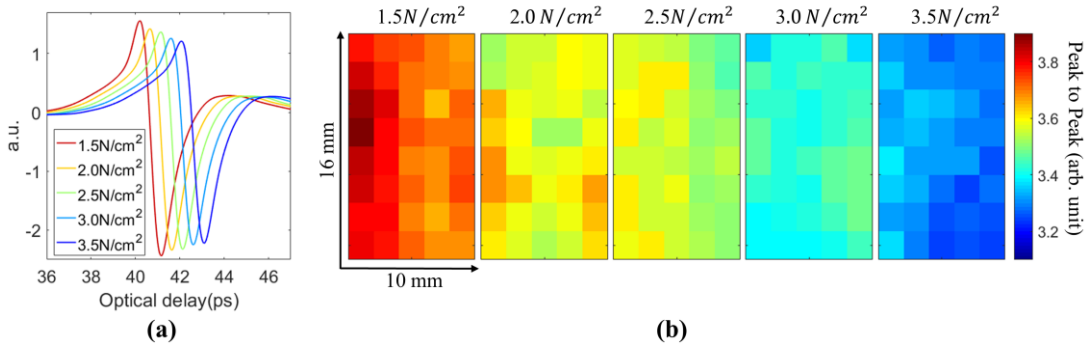

Fig. 3. 4 (a) Processed THz pulse of a single point under different pressures (b) Images of the peak to peak of the processed THz pulse under different pressures

3.6.2. Changes in the optical properties under different pressures

Fig. 3. 5(a) shows the change in the reflectivity of skin at 0.6 THz for one subject under different pressures during a one minute measurement. The small circles represent the values measured every 2.5 s, and the lines are the fitted results of all measured data. The first several points are removed due to fluctuations caused by unstable pressure. In Figure 3.3(a) one can see that the reflectivity slightly decreases throughout the one minute measurement even under the same applied pressure. Under higher pressures, the reflectivity has a lower starting value than that observed at lower pressures. This change in the reflectivity during the one minute measurement is due to the occlusion effect. After the skin contacts with the imaging window, water starts to accumulate in the SC causing an increase in the refractive index and a decrease of the reflectivity during the one minute measurement. This result shows that occlusion is a factor that cannot be ignored and must be considered when performing measurements in a reflection geometry which involves contact between the skin and an imaging window. Therefore, when doing THz *in vivo* measurements, the occlusion time must be carefully controlled and should be considered when planning the measurement protocol.

Fig. 3. 5(b) shows the reflectivity at 0.6 THz under different pressures for five subjects with 3 repeats performed at each pressure. From Fig. 3. 5((b), reflectivity is seen to decrease as the pressure increases. For all the data, the skin was in contact with the imaging window for 30 seconds prior to sampling and the plotted

value is the average of three measurements. The error bar is the standard deviation. From our results, it can be seen that the reflectivity can decrease by up to ~0.02 (over 30%) under the higher pressures and the refractive index can increase by ~0.2 (over 10%) with increasing pressure. These results indicate that under different pressures, the measured properties of the skin can be significantly different.

We speculate that the possible reason for the significant difference under different pressures is that with the increase in pressure, the skin is compressed and thus the water concentration and biological density increases. This idea is also further supported by the proposed fitting model used in section 3.6.3. The different properties under different pressures signifies that the pressure effect is not negligible when performing *in vivo* THz measurements.

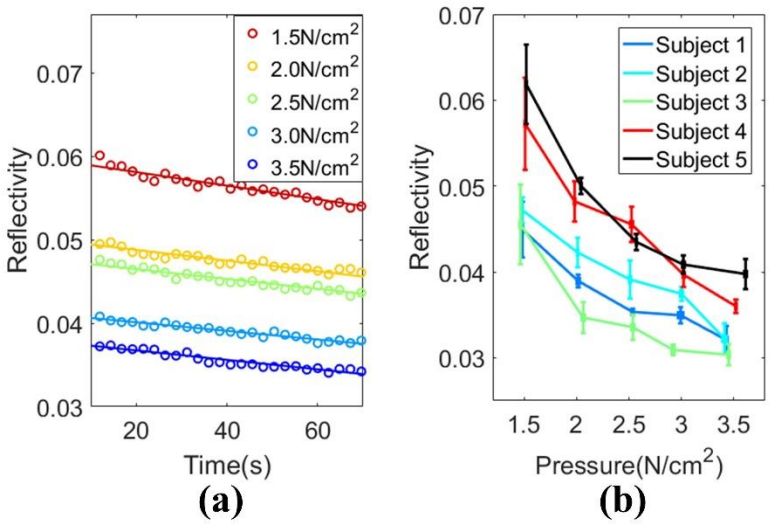

Fig. 3. 5 (a) Reflectivity of skin under different pressures at 0.6 THz during a 1 min measurement. (b) Average of 3 repeats of reflectivity of different subjects under different pressures at 0.6 THz 30 s after skin initial contact with quartz window

Fig. 3. 6(a) shows the reflectivity of one subject as a function of frequency for skin under applied pressures ranging from 1.5 N/cm^2 to 3.5 N/cm^2. The plot shows the averaged results of three measurements of one subject. We can observe significant differences across the full frequency spectrum measured under different pressures. When applying higher pressures, the reflectivity decreases for all frequencies. This result indicates that pressure will significantly affect the THz spectrum of skin. Fig. 3. *6* (b) shows the refractive index and absorption coefficient under different pressures. The refractive index increases with increased applied pressure, while the absorption coefficient shows no obvious trend. However, the calculated absorption coefficient enables us to estimate the penetration depth of THz radiation inside the measured tissues. Given that the absorption coefficient of skin is around $115\sim200\,cm^{-1}$ at frequencies from 0.3 to 0.95 THz according to Fig. 3. 6 (b), the penetration depth is around $50\sim87\,\mu m$ depending on the frequency. This was calculated using Eq. 3. 2,

$$d = 1/\alpha \qquad (3.\ 2)$$

where α is the absorption coefficient. In the case when the THz waves penetrate 100 μm into the skin, the reflected intensity received by the detector would be around 5% of the emitted intensity at 0.6 THz with the absorption coefficient being around $153.1\,cm^{-1}$. This is calculated using Eq. 3. 3.

$$I = I_0 \exp(-\alpha \times d) = I_0 \exp(-153.1 \times 2 \times 100 \times 10^{-4}) = 0.0468 I_0 \qquad (3.\ 3)$$

Therefore, we focus on understanding the mechanisms at work at skin surface especially the SC layer.

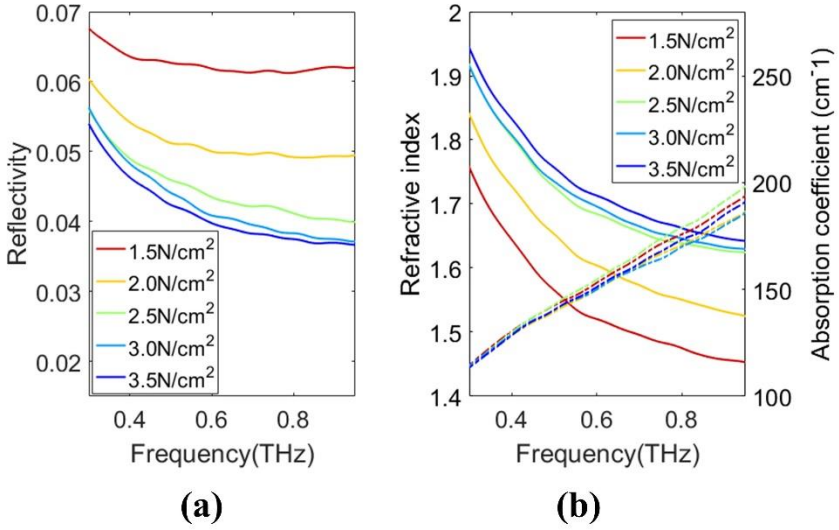

Fig. 3. 6 (a) Reflectivity (b) refractive index and absorption coefficient under different pressures from 0.3 THz to 0.95 THz.

3.6.3. Mechanism of the pressure effect

In the shown results above, it is obvious that the pressure applied to the skin during *in vivo* THz measurements will alter the THz response of skin and therefore the optical indices. However, the mechanical deformation and property changes are unknown. Therefore, we applied the stratified media model to give us insight into the pressure effect and elucidate the structural changes induced in the skin (see section 2.6 and 3.5 for details).

To increase the signal to noise of our results, we averaged ten consecutive THz pulses after the skin has been in contact with the imaging window for 30 seconds. The ten THz pulses were acquired in 2.5 seconds and since the skin has already been in contact with the imaging window for 30 seconds, the occlusion effect between these ten pulses is minimal[72]. Further, each pressure measurement was repeated 3 times to ensure there were no errors caused by the individual's behavior, ie. washing the area under investigation or sweating. We fit the measured

reflectivity with our model individually and averaged the fitting results for each pressure. Fig. 3. 7(a) shows the thickness and hydration percentage in each layer of the skin for one subject at different applied pressures. The hydration percentage is lower at the surface of the SC with a linear increase in the hydration with depth, a similar trend is followed by the epidermis layer. However, the hydration percentage remains almost constant when it reaches dermis. Fig. 3. 7 (a) shows that, as pressure increases, the SC thickness decreases and the surface hydration percentage increases. Fig. 3. 7(b) shows the averaged refractive index of the dehydrated skin and we can see a clear increase with increasing pressure. The change in the thickness of the SC is also plotted in Fig. 3. 7 (b). These fitting results support our speculation that the biological density and water concentration increase due to the increased compression of the skin. However, little information can be inferred about the deeper skin layers because of the strong absorption of THz by water, so the signal is highly attenuated by these deep skin layers.

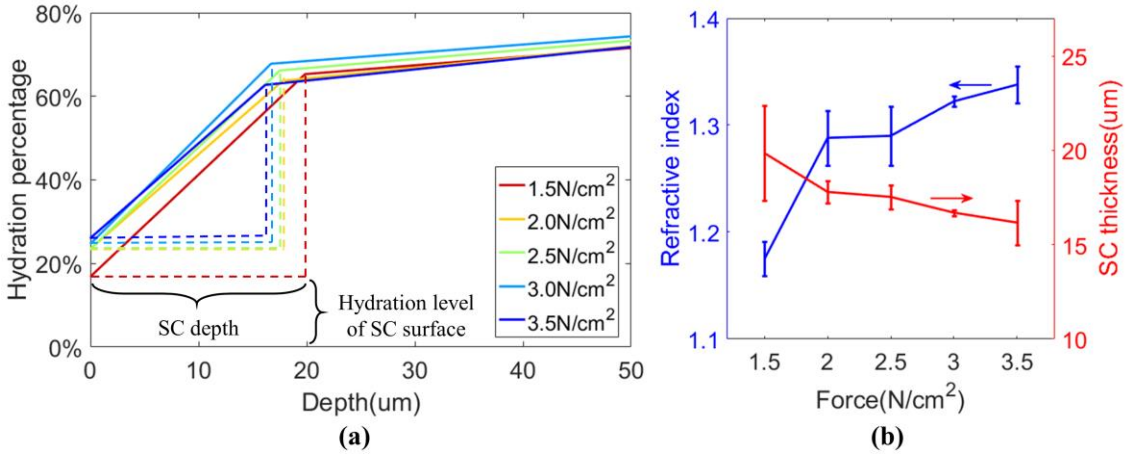

Fig. 3. 7 (a)Water distribution derived by fitting the data with the stratified media model (b) refractive index of dehydrated skin and SC thickness changes with increased pressure. Note that the errorbar is the standard deviation of 5 subjects' results.

3.7. Protocol for THz *in vivo* skin measurements

As discussed above, there are various factors affecting *in vivo* skin measurements. Among them, occlusion and the effect of contact pressure have been systematically studied and it is possible to minimize the effect of these variables on the results. However, to minimize the effect caused by these two factors, a robust protocol is needed. By integrating pressure sensors with the THz-TDS system, the applied pressure and occlusion time can be recorded. The pressure sensor is able to give a real-time feedback in our setup and therefore can be used to help the subjects apply pressure within a defined target pressure region. This also gives a record of when the skin initially contacts the quartz window and how long the skin has been occluded for. By utilizing the pressure sensor, the pressure can be controlled and the occlusion time can be recorded. When comparing different measurements, one should be make sure that pressure within the same desired range is applied and the occlusion time is consistent to minimize the effects caused by the two factors.

However, the THz response also depends on the experimental setup. For example, the polarization of THz light and the geometry (incident angle) will both affect the reflected THz pulse observed. However, calculating the optical indices of the skin from different setups would eliminate the changes caused by experimental geometry. As some tissues, such as skin are polarization-sensitive, they might give different responses when measured with different polarizations, this will be

discussed in Chapter 6. The difference caused by light polarization is due a difference in the properties of the tissue itself not due to the measurement. Therefore, when conducting comparisons between studies, the polarization of light should also be considered.

Other environmental variables can be eliminated and minimized by normalization of the results and with a well-controlled experimental procedure. For example, when studying the effect of a topically-applied product (ie. moisturizer), a control region should be measured where no product is applied and in addition to the treated region where the product of interest is applied. By monitoring the differences between these two regions, one can study the effects caused by the product. This procedure can be called normalization because the environment will affect both regions equally, so the change measured in the control region can be subtracted from the change in the treated region, removing the influence of the environment on the skin. This method is also used by our group to study the effects of moisturizer on the skin. Details of this work can be found in reference[77]. However, methods to control variation arising from differences in skin type are still limited because of a lack of studies on the effect of ethnicity, gender and age on the THz response of skin. Therefore, our study neglects any differences caused by the skin type.

3.8. Summary

In this Chapter, the variables that affecting *in vivo* THz studies have been introduced in order to establish a robust protocol. During contact measurements of the skin, occlusion and contact pressure will affect the THz response of skin due to internal changes inside skin. The pressure effect is carefully studied in this Chapter including the observation of changes in the THz pulse response and optical properties of skin under different pressures, while the occlusion effect was previously studied extensively by Sun et al.[72]. The stratified media model is also used to help gain understanding of the changes in the thickness and hydration of the SC under different pressure. The increased contact pressure will cause the skin to be compressed and therefore the surface hydration and skin density increases while the SC thickness decreases. This leads to the decreased reflectivity and increased refractive index observed. Due to the significant changes in the optical indices under different contact pressures, careful control of pressure with a pressure sensor is needed during *in vivo* studies. A protocol which considers and carefully controls these various factors which can affect THz measurements is in high demand. Pressure sensors can only be used to account for pressure and occlusion effects. Normalization and careful protocol planning as well as controlled environmental conditions are also recommended.

4. Investigation of Silicone gel sheet treatment

4.1. Introduction

Hypertrophic and keloid scars frequently occur on human skin after surgery and burn injuries[78,79]. Current treatment methods include applying tretinoin cream, pulsed dye laser and surgical excision etc.[78] Silicone therapy is widely used for healing and preventing hypertrophic and keloid scars in clinical treatment because of the minimum side effects, high efficiency and ease of application[78,80,81]. Silicone gel sheet (SGS) is one of the products that is widely available in markets. However, the mechanism of the impact on the skin is little understood [78]. One study suggests that the semi-occlusive nature of SGS provides an increase in hydration that causes a decrease in transepidermal water loss(TEWL) and downregulates the production of collagen[80,82]. There are also other studies showing that the temperature and static electric field changes upon the application of SGS might also play a role in the efficacy of the treatment[79,83,84]. Therefore, quantitively monitoring the effects of SGS treatment *in vivo* is important to help advance the understanding of the mechanism of SGS treatment. However, methods to quantitively and objectively monitor the internal dynamic alterations of skin *in vivo* are lacking, usually assessments of the progress of treatment use factors such as scar shape, color, texture and thickness[85,86]. Due to the high sensitivity of THz radiation to fluidic changes inside skin and the repeatability of the protocol developed in Chapter 3, we employed THz imaging to monitor the

effect of SGS treatment on normal skin *in vivo*. It could be further used for scar treatment analysis.

4.2. Experiment setup and protocols

Self- adhesive CICA-CARE scar treatment gel sheet and BapScarCare SPF25 silicone scar gel were used to be applied to the volar forearm in our experiment, shown by Fig. 4. 1. As illustrated in Fig. 4. 2(a), a THz-TDS system (Menlo TERA K15) was used. The system is able to measure time-domain pulses from a single point at a frequency of 4 Hz and image the targeted area with $0.5mm \times 0.5mm$ resolution by moving the x-y stage.

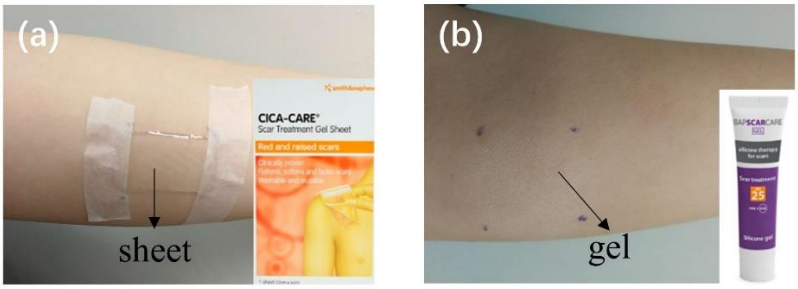

Fig. 4. 1 Skin applied with (a)Silicone gel sheet and (b) silicone gel

In our experiment, we performed two types of measurements, point scans and imaging. For the point scans, the THz beam was focused onto a single point in the targeted area. In the imaging mode, a line was scanned during each measurement, the THz beam was only moved in the y direction to image a single line at intervals of 0.5 mm. The images were acquired after treatment with SGS for different time periods. A piece of aluminium foil with different apertures cut out (30× 20mm for point scan, 20× 40mm for line scan) was put on the imaging window when doing the different experiments to make sure that the same area was measured each

time. Illustrated in Fig. 4. 2 (b)-(d), the target area on the skin was also marked with pen at the corners.

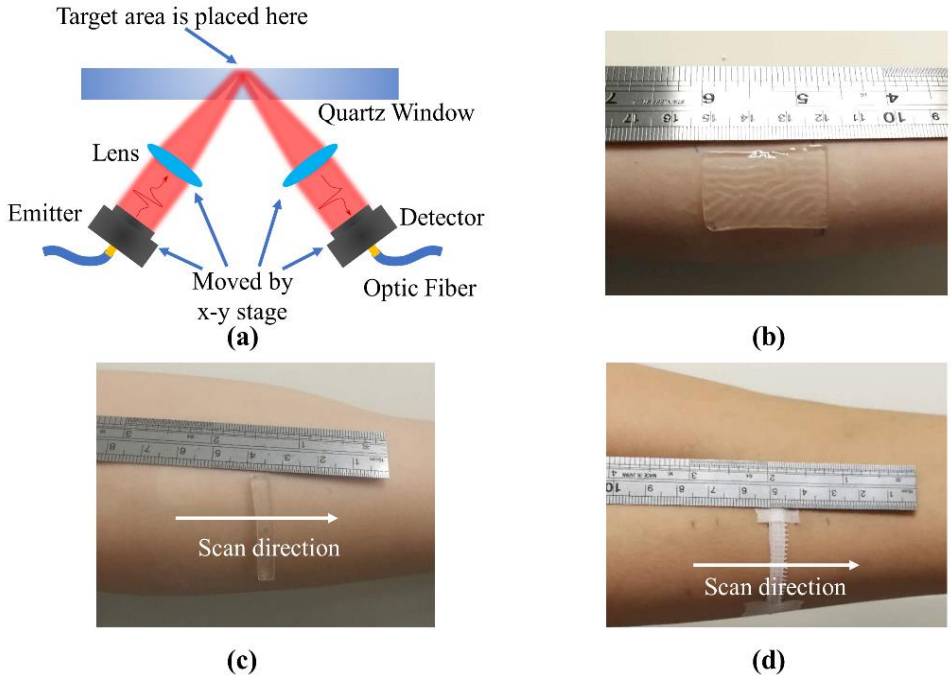

Fig. 4. 2 (a)Experiment setup. Photograph of the (b) silicone gel sheeting (c) a slim strip of silicone gel sheeting (d) wet bandage applied to normal skin

For the point scan measurements, the initial state of skin was measured for 1 minute continuously before the application of the SGS. Then there was a rest time of at least one hour to allow the skin to recover from the effects of occlusion. A piece of $30 \times 20mm^2$ SGS was then applied to the marked area for 4 hours for each subject, as illustrated in Fig. 4. 2 (b). After treatment, the SGS was removed before the area was measured again for 1 minute. We repeated this experiment on 10 subjects in order to verify the effects.

For the line scan measurements, a 5× 20mm strip of SGS was applied to the volar forearm and after the SGS was removed, a line scan was performed with the scan direction perpendicular to that of SGS strip, as displayed in Fig. 4. 2 (c) where

both treated and untreated areas are measured. A 5× 20mm strip of wet bandage which had been soaked in water for 5 minutes before squeezing out the excess water was also applied to skin as shown in Fig. 4. 2 (d), the bandage was applied to untreated skin for 10 minutes then removed to allow the target region to be measured. We measured the effect of SGS after 10 minutes, 4 hours and 12 hours application and the state of the skin was monitored for 2 hours after the removal of the SGS.

4.3. Results and discussion

4.3.1. THz response of skin before and after SGS application

Fig. 4. 3 displays the THz response of skin before and after 4 hours treatment with SGS. A single point in the area of interest was measured continuously for 1 minute for 10 subjects. Details of the data processing were introduced in section 2.5. Fig. 4. 3 (a) shows the averaged peak to peak of processed signal of the 10 subjects during a 1 minute measurement. The error bar is the standard deviation. After 4 hours of occlusion by the SGS, the peak to peak of the processed signal decreased dramatically, this indicates that the water content in the skin was altered. Studies show that since THz radiation is highly absorbed by water, the increase of water in the skin leads to a decrease in the amplitude of the reflected signal[72,87]. Fig. 4. 3 (b) reveals how the processed THz pulse changed after treatment for one subject. The result proves that SGS has an occlusive effect on skin and that this increases the hydration level of skin. Moreover, as illustrated in Fig. 4. 3 (a), before the application of SGS, the peak to peak decreases during the

one-minute contact measurement. However, after application of SGS, the peak to peak during the one-minute measurement remains almost unchanged, this suggests that the skin is already saturated with water due to the occlusive effects of the SGS.

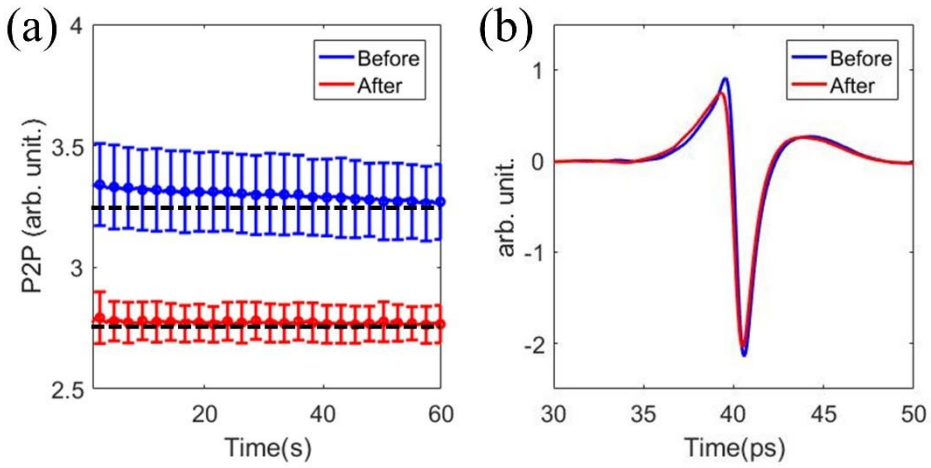

Fig. 4. 3 (a) Averaged peak to peak of the processed signal of 10 subjects (b) Processed signal of one subject before and after treatment by SGS for 4 hours.

We also conducted measurements on silicone gel as a comparison. Instead of applying SGS onto the target area, the gel form was rubbed into skin and the measurements on the same area were token directly at 10 minutes and 4 hours after application. As shown by Fig. 4. 4, the peak to peak of skin only showed a subtle decrease 10 minutes after application and after 4 hours there was almost no difference between the original skin (before application) and treated skin. This indicates that SGS has better performance in terms of occlusion. Therefore, in this study, we mainly studied the effect of SGS.

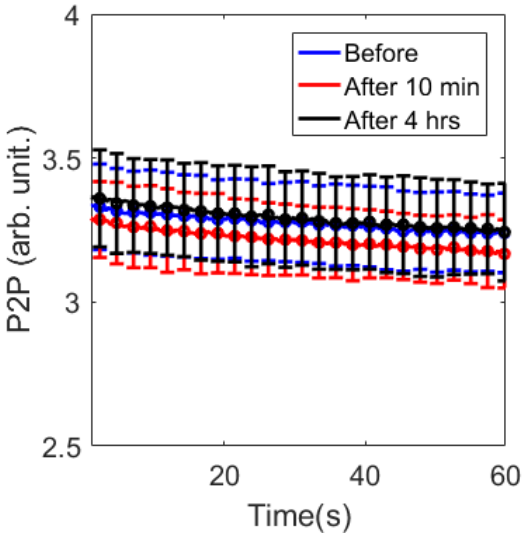

Fig. 4. 4 Averaged peak to peak of processed signal of 10 subjects before and after treatment by silicone gel for 10 minutes and 4 hours.

4.3.2. Changes in the optical properties before and after SGS application

The optical indices of the skin were calculated using the procedure mentioned in section 2.5, Fig. 4. 5 shows the averaged changes in the optical indices of 10 subjects before and after 4 hours of occlusion with SGS in the frequency domain with the error bars showing the standard deviation. We plotted the pulses 30 s after initial contact with quartz window as the rate of change in the skin due to occlusion decreases with occlusion time so by 30 s into the measurement, the signals were more time-stable. After treatment the reflectivity decreased across all frequencies from 0.2 THz to 1 THz (Fig 4.4 (a)), whilst the refractive index increased (Fig. 4. 5 (b))and absorption coefficient decreased (Fig. 4. 5 (c)). Our results showed good consistency between all subjects and demonstrate that the THz spectrum is significantly different for skin that has been treated with SGS due to changes in the properties of the skin. We suspect that the increase in the refractive index may be due to the increased water content inside the skin.

However, with water increasing in the skin, the absorption coefficient should also increase, this is not consistent with our finding in Fig. 4. 5 (c). This is because treating skin as a one-layer homogeneous structure is an over-simplification, as the water content in the SC and epidermis are different. Therefore, in next section we will derive the changes in the hydration state of the skin by treating skin as a 2-layer structure.

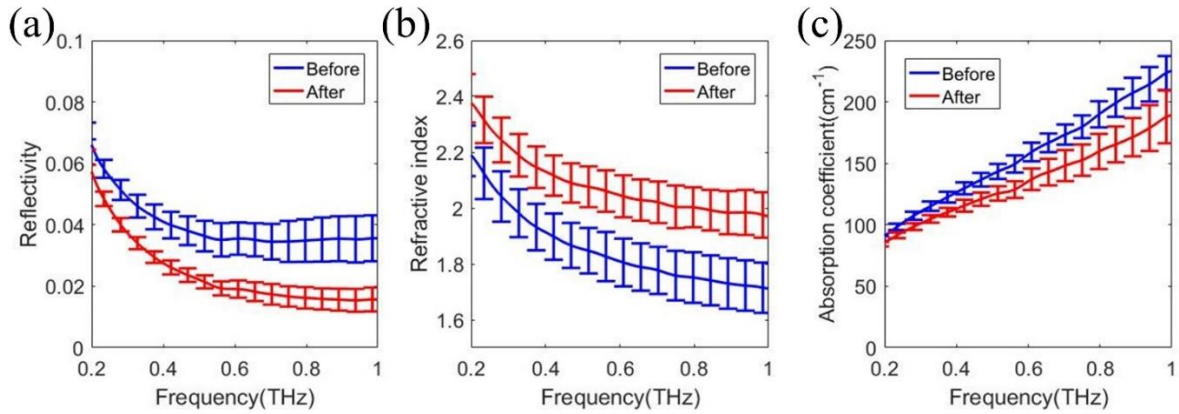

Fig. 4. 5 (a) Averaged reflectivity (b) refractive index (c) absorption coefficient of 10 subjects before and after treatment by SGS for 4 hours.

4.3.3. Hydration in the SC and epidermis extracted using a 2-layer skin model

As discussed in section 2.6, the hydration in the SC and epidermis can be calculated using EMT and Fresnel theory. Fig. 4. 6(a) shows the extracted hydration in the SC from the 1 minute measurements taken before and after the application of SGS for 4 hours. The water percentage in the SC increased by about 40% following the treatment, indicating the occlusive effect of the SGS. However, as illustrated in Fig. 4. 6 (b), the water percentage in the epidermis did not change much. The SC swelled a little due to the treatment as we observe an increase in

thickness. Fig. 4. 7 shows the averaged refractive index and absorption coefficient at t=30s for 10 subjects where the error bars are the standard deviation. This figure verifies what we found in Fig. 4. 6. Both the refractive index and absorption coefficient increase for the SC layer due to the significantly increased water content in this layer, whilst these two optical indices remain the same in the epidermis layer due to the almost unchanged hydration in this layer.

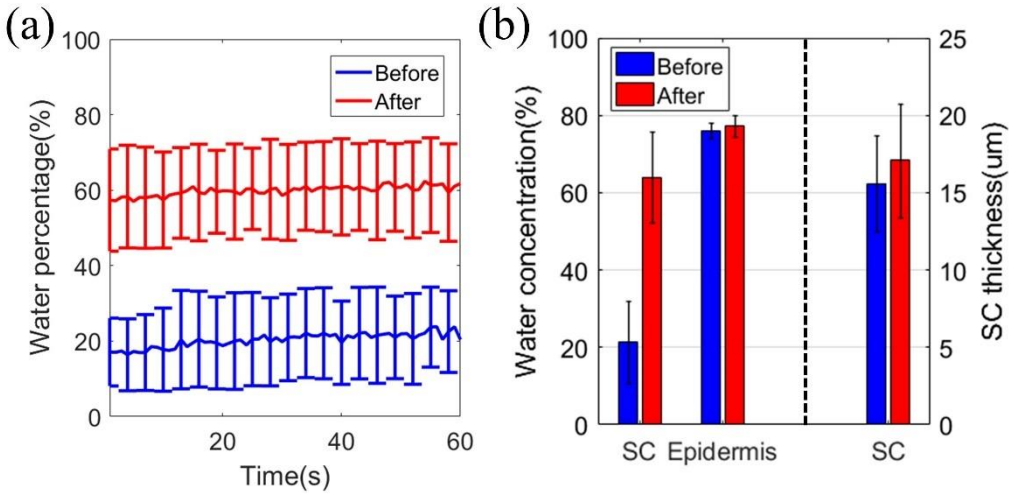

Fig. 4. 6 (a) Averaged water percentage in SC (b) averaged water percentage in SC, epidermis and SC thickness of 10 subjects at t=30 s before and after treatment by SGS for 4 hours.

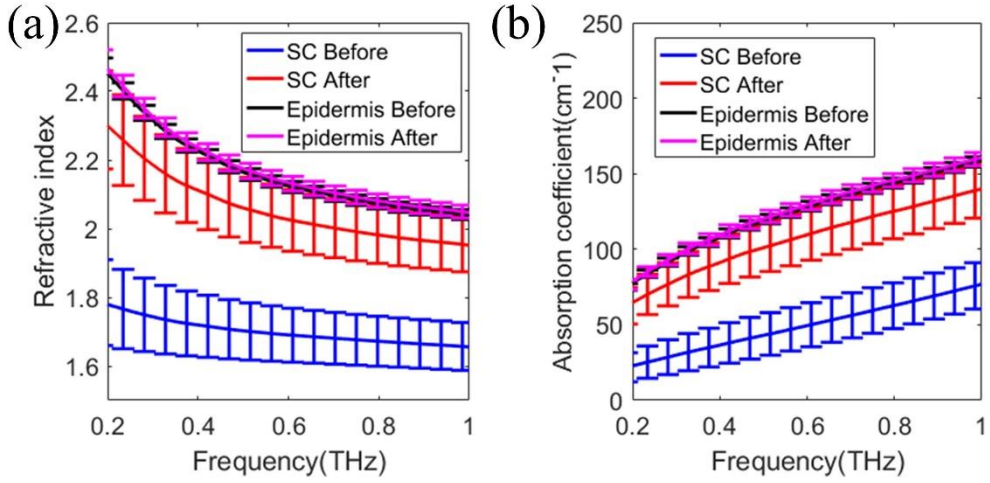

Fig. 4. 7 (a) Averaged Refractive index (b) averaged absorption coefficient of 10 subjects at t=30 s before and after treatment with SGS for 4 hours.

4.3.4. Occlusion effect by SGS

With the knowledge that the SGS partially prevents water inside the skin from diffusing to the outside, the process which occurs during treatment is still only vaguely understood. Here we show an experiment in which an imaging scan is conducted to show the contrast between untreated skin and areas treated with SGS. In this way, we can quantify the effects induced by the SGS and check how it affects the skin over different application times. The scan direction and other details have already been described in section 4.2. Before applying the SGS, we measured the normal skin 3 times. Then after resting for over 1 hour, a 5× 20mm strip of SGS was applied to the area of interest. Then a line scan was performed of the skin after 10, 30, 60, 120 and 240 minutes of occlusion by the SGS. The SGS was re-applied to the same area immediately after each measurement. The results are shown in Fig. 4. 8(a) where the peak to peak of the processed signal was normalized by the averaged amplitude of the untreated skin. Each line in the image represents a line scan measurement acquired at a different time. After 10 and 30 minutes of occlusion by the SGS, the peak to peak of the processed signal continued to decrease but the amplitude almost did not change after 1 hour of occlusion meaning that the water content in the skin was almost saturated so there were no further effects due to occlusion. Fig. 4. 8 (b) shows the processed THz pulse before treatment and after increasing occlusion times (sampled from the line scan at the point indicated by the black line in Fig. 4. 8 (a)). There is a clear decrease in

the amplitude of the pulse in the first hour and a slight fluctuation in the subsequent 3 hours.

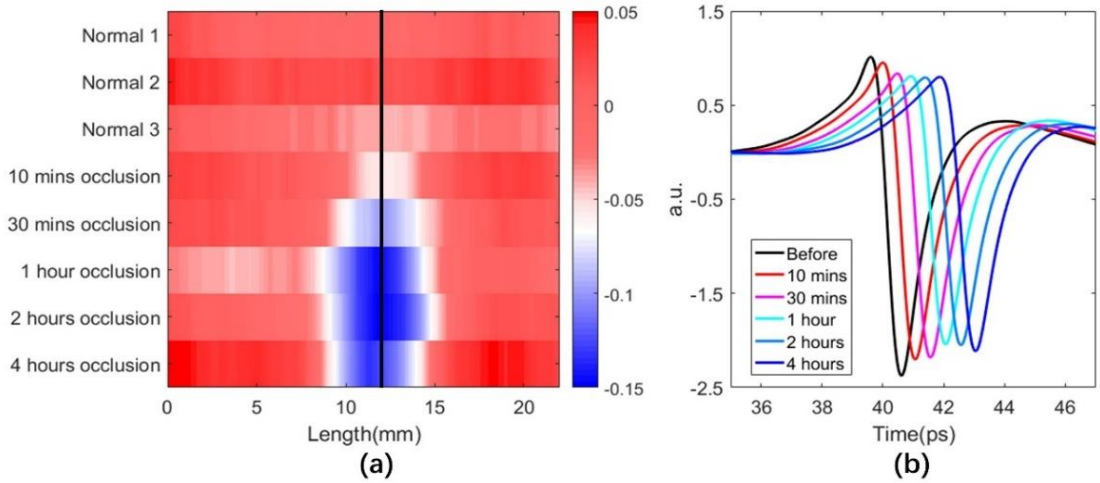

Fig. 4. 8 (a) Peak to peak of different line scan measurements after skin was occluded by SGS for different times (b) Processed signal of different line scan measurement after skin was occluded by SGS for different time (sampled from the point marked by the black line in (a)).

4.3.5. Lateral diffusion of water caused by SGS

In Fig. 4. 9(a) and (b), the line scan image results following 10 minutes of occlusion by SGS and the wet bandage and their recovery process are shown. A comparison of the SGS results in Fig. 4. 9 (a) with the wet bandage results in Fig. 4.8(b) reveals that the amplitude of the reflected signal decreases much more significantly following the application of the wet bandage. Though the bandage is only 5 mm in width, the width where the amplitude decreased in Fig. 4. 9 (b) is about 10 mm. While for the image of the SGS treatment, the width is only about 5 mm as shown in Fig. 4. 9 (a). Further, in Fig. 4. 10 in next section, the affected area is only about 5 mm regardless of how long the SGS has been applied to skin. However, skin that has been treated for 10 minutes by either the SGS or wet

bandage recovered quickly (under 5 minutes) after removal. These results indicate that SGS only occludes the skin and only increases the hydration level in the applied area, in other words the water does not diffuse to the lateral surrounding areas. However, for the wet bandage, water does diffuse to surrounding areas and thus increases the water content of nearby tissue. Although the wet bandage increases hydration level in skin speedily and significantly, skin still recovers back quickly.

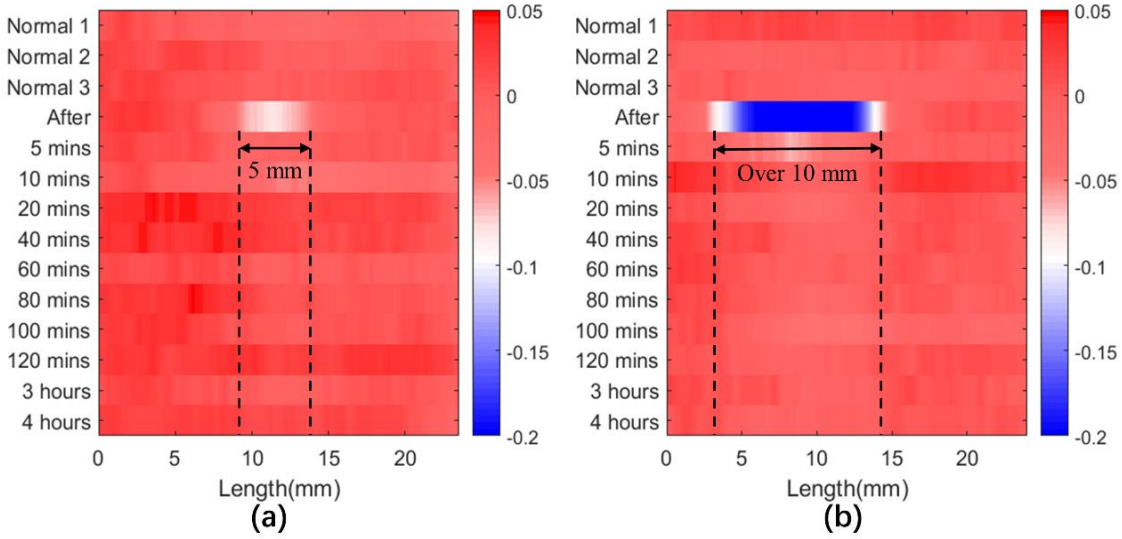

Fig. 4. 9 Normalized peak to peak of the processed signal of line scan measurement of skin before and after occlusion by (a) SGS (b) wet bandage for 10 minutes.

4.3.6. Recovery process after the removal of SGS

With the knowledge that the SGS can provide an observable occlusion effect after 10 minutes of treatment, we are left with the question of how long patients should wear it to optimize the effects of the treatment whilst balancing this with the inconvenience for the patient of having to wear the SGS. To understand how the skin state changes after the removal of the SGS, the recovery process was also

observed. Subjects were asked to wear the SGS for different durations: 4 hours and 12 hours. Fig. 4. 10 shows the recovery process after wearing SGS for 4 and 12 hours respectively. Note that the amplitude has been normalized to the averaged amplitude before treatment. The amplitude of the signal increases following removal of the SGS and has almost recovered back to the initial state after 1 hour for both treatment durations. The results indicate that after removing SGS, the occlusion effect is only maintained for a short duration and will recover back to the steady state within 80-100 minutes. This means that in order to maintain the occlusion effects, the SGS should be worn for longer times. This result may provide useful information for clinical treatment strategies.

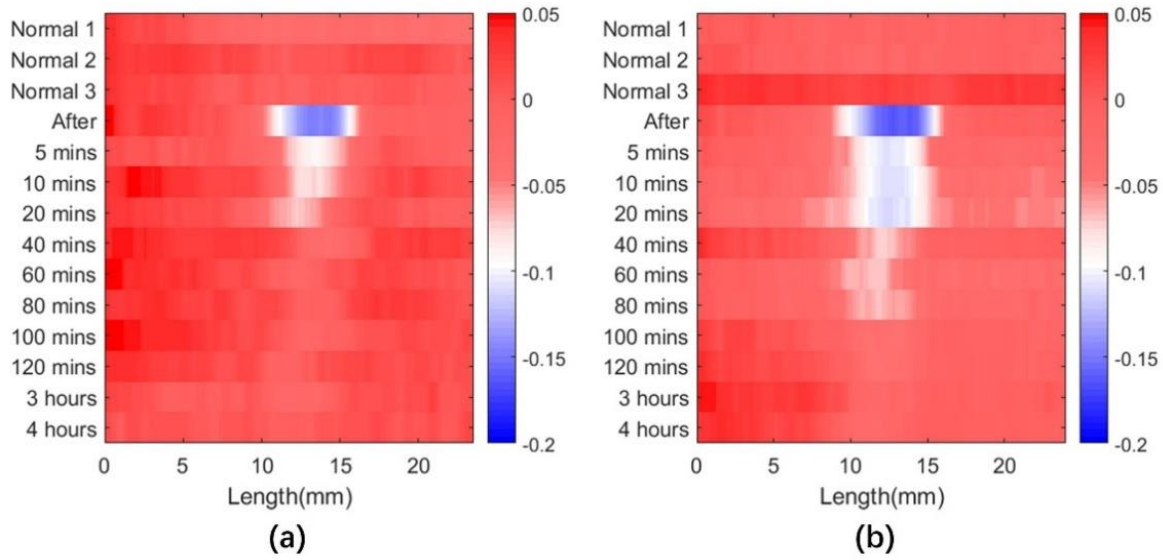

Fig. 4. 10 Peak to peak of different line scan measurement of skin before and after occlusion by SGS for (a) 4 hours (b) 12 hours

4.4. Summary

In this chapter, we demonstrated how THz spectroscopy and imaging can be used for monitoring SGS treatment. Both the frequency and time domain results

show significant alterations following the SGS treatment. The line scan imaging in this work is of fundamental importance in using THz imaging to investigate SGS occlusion effects. There are several findings in our work. From the point scan results, the frequency and time domain results show that SGS has an occlusive effect on the skin and will cause the THz signal and spectrum to change. With the skin model, we are able to extract the fluidic changes inside skin. By comparing the treated site with an untreated site, we find that the water content inside the skin will increase with occlusion by SGS treatment and will be saturated after about 1 hour. However, after removing SGS, the skin will quickly recover back in under 100 minutes. This conclusion may provide information for clinical treatments. The comparison with the result of applying a wet bandage draws the conclusion that SGS only provides an occlusive effect and increases the hydration level in the treated area and water does not diffuse laterally. In summary, our work demonstrates that THz imaging can be used for quantitively monitoring SGS treatment *in vivo* and in particular observing the occlusion and hydration effects caused by SGS treatment. Our work enhances the understanding of the mechanism and effect of SGS treatment on the skin and can be further used clinically.

5. THz imaging for transdermal drug delivery

5.1. Introduction

Transdermal drug delivery has recently attracted interest due to its superiority compared to other approaches to drug delivery such as oral and hypodermic needle applications[88]. However, the resistance of the SC is limiting the efficiency of transdermal drug delivery. Microneedle patches are one of the methods used to enhance the efficiency of transdermal drug delivery. Microneedle patches are arrays of needles in the micro scale which can easily penetrate the SC and deliver drugs to the epidermis or dermis layers in the skin without disturbing nerves. Compared to hypodermic injections, it is painless and allows patients to administer drugs themselves. Compared to oral delivery, it provides another option for drugs that are not suitable for intestinal absorption and avoids gastrointestinal tract side effects [88].

Currently, the microneedle patch is divided into different types based on different drug administration and microneedle fabrication methods[89,90]. Solid microneedle patches are used to create temporary channels in the skin surface and the drug is then applied directly to the target area after removing the patch. The temporarily created conduits allow the drug to diffuse into the skin. Another type of microneedle patch uses drug coated needles and once the patch is applied to the skin, the drug starts to diffuse. Dissolving and hollow microneedle patches can deliver drugs to the skin either by the microneedles themselves or through a

channel inside the needle allowing the drug to transfer into the skin[89,90]. Repeated application of microneedle patches can cause irritation in the skin and nanoneedle patches provide an option for repeated application due to the extremely small size of the needles.

To understand the efficacy of the drug delivery, imaging methods that can reveal the transdermal drug delivery process are in high demand. Optical coherence tomography(OCT) can be used to study the skin structure before and after the application of the microneedles. Zhao et al. showed holes created by microneedles in skin and observed microvascular changes and the start of the recovery of the created holes after 4 hours[91]. Another commonly used imaging technique to analyze the depth and the quantity the drug has penetrated into skin is fluorescence imaging[91,92]. However, it is *ex vivo* and needs fluorescent agents for drugs to be tracked. Therefore, a technique that can provide *in vivo* imaging and can quantify the amount of drug delivered is in high demand.

5.2. THz imaging for transdermal drug delivery

Due to its high sensitivity to liquids, THz imaging can easily track drugs dissolved in glycerol, water or other solutions. Moreover, THz-TDS systems enable us to acquire the THz spectrum of the target area which can assist in the detection of characteristic peaks or troughs in the frequency domain for the drug of interests. Kim et al. used THz imaging to monitor ketoprofen dissolved in dimethyl sulfoxide (DMSO) applied to the skin surface and the reflection imaging of the underside of

skin showed that the amount of drug penetrating through skin can be represented by THz pulse amplitude and shape[38]. The concentrations of drugs on the skin surface can also represented by the THz pulse [39]. Naccache et al. observed that the spectral peak of ibuprofen at around 1.04THz changes under different temperatures which can be further used for THz thermometry and imaging[93].

Glycerol is commonly used as a component in cosmetic products and as a chemical enhancer for transdermal drug delivery[94]. It has been reported that 50% w/v glycerol/water mixture will not cause discernible histological changes in nude rice skin[95]. Glycerol has also been used as a contrast agent for THz imaging[94]. Therefore, using glycerol/water mixtures as the solvent can give good contrast and cause subtle damage to skin. Aspirin is known as an antipyretic, analgesic and antiplatelet drug. However, oral administration of aspirin can have gastrointestinal side effects[96]. Transdermal delivery provides a safer, more convenient alternative to avoid these side effects[96]. Ethanol is used to enhance the solubility of aspirin.

Based on the capability of THz imaging and the high demand for monitoring transdermal drug delivery, in this chapter we explore how to utilize THz imaging to evaluate different transdermal drug delivery methods *ex vivo*.

5.3. Experimental setup and protocols

The experiment is conducted using a reflection geometry with a THz-TDS system with the upside of the porcine skin placed onto the quartz window as

illustrated in Fig. 5. 1. The drug solutions were synthesized by 50mg/ml aspirin/ethanol solution and 50% w/v glycerol/water solution with aspirin/ethanol solution making up 10% of the total volume.

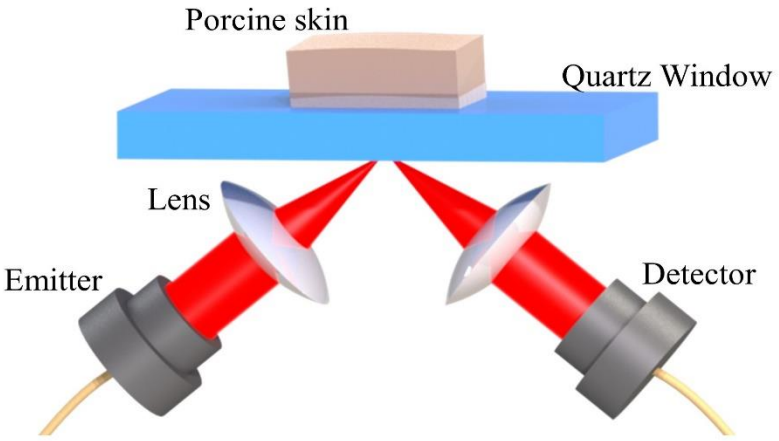

Fig. 5. 1 Experimental setup and the placement of the porcine skin on the window

Ex vivo experiments on fresh porcine skin were conducted. The porcine skin was cut into 3×3 cm^2 pieces and cleaned with a moist cotton pad. Cling film was used to prevent the porcine skin from dehydration before the THz measurements were performed. To test the efficiency of the drug delivery, we measured 5 groups, with one group acting as the control group. The measurements of each group were repeated 10 times with the same protocol. The first group is the control group and in this group the samples did not receive any kind of treatment. The second group is the 'Normal Transdermal Drug Delivery (NT) group and in this group, 5 µl of the drug was applied to the porcine skin surface for 5 minutes before imaging with a rubber ring being used to confine the liquid and avoid the drug flowing over. The third group is the 'Transdermal Drug Delivery by Pad (PT)' group, in this group, 80 µl of the drug was dripped onto a 1 cm diameter cotton pad. The pad was then

applied to the porcine skin surface for 5 minutes. The fourth group is the 'Nano-Needle Drug Delivery (NN)' group, and was first treated with a nano-needle patch to create nano-scale holes on the surface of the porcine skin and then the drug soaked cotton pad was applied to the porcine skin. The fifth group is 'Micro-Needle Drug Delivery (MN)' group, in this group, we used the same strategy as NN group but we used a micro-needle patch instead. The treatment protocols are summarized in Table 5.1. Fig. 5. 2 shows an illustration of the different treatment protocols. Fig. 5.3 is a diagram of the micro and nan needle patches.

Table 5.1. Groups and Corresponding Treatment Protocols

Control	Normal Transdermal Drug Delivery (NT)	Transdermal Drug Delivery by Pad (PT)	Nano-Needle Drug Delivery (NN)	Micro-Needle Drug Delivery (MN)
No drug applied.	5 µl of the drug solution was directly applied to the porcine skin surface.	80 µl of the drug was dripped onto a 1 cm diameter cotton pad and then the pad was applied to the porcine skin surface.	A nano-needle patch (Nano needle, Konmison) was used to create nano-scale holes on the porcine skin surface and then a cotton pad with 80 µl of the drug was applied.	Same as NN group but used a micro-needle patch (9-pin microneedle, Konmison) instead.

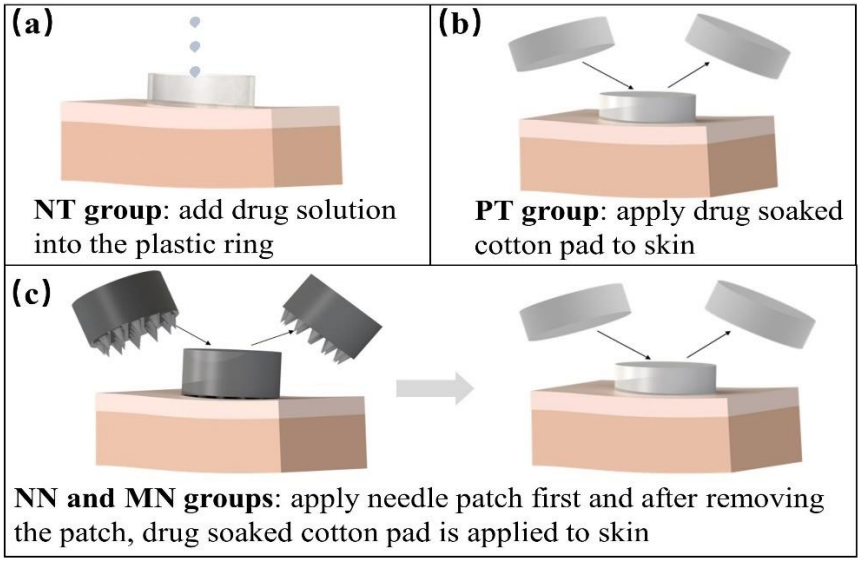

Fig. 5. 2 Diagram of treatment protocols for the (a) NT group (b) PT group (c) NN and MN groups

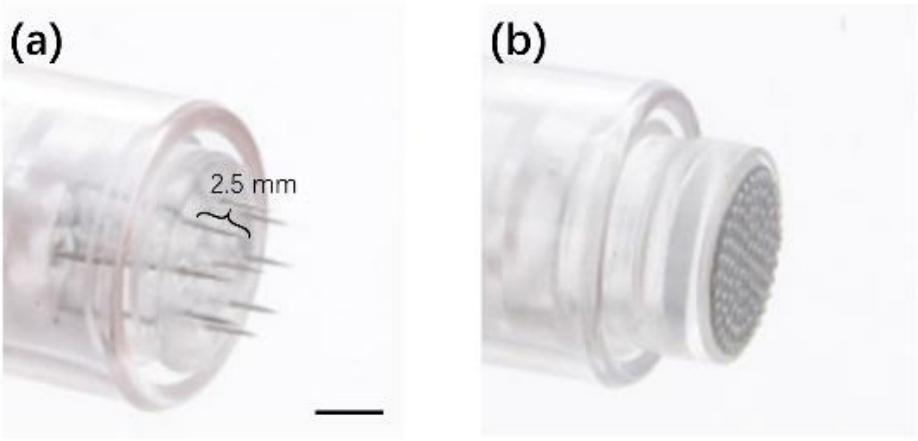

Fig. 5. 3 Diagram of (a) microneedle patch with 9 needles in one patch and (b) nano needle patch with 200 needles in one patch. The bar is 3 mm. The needles in (a) and (b) are 2.5 mm and 0.25 mm in length respectively. The needle widths (diameters) are 0.25 mm for both.

As mentioned above, we have 5 groups in total. Each piece of porcine skin was imaged before any kind of treatment. After the treatment, the image was repeated on each piece of porcine skin. Each image is 2×2 cm^2 with each pixel representing $0.5mm^2$. Note that for NT group, the residue of the drug was wiped off before imaging. For other groups, the drug soaked cotton pad enabled skin to absorb drug

without leaving a residue. The drug solution was also measured in reflection geometry with a rubber ring to confine the solution and make sure that the thickness of the solution inside the rubber ring is thick enough to provide total attenuation of THz radiation inside the water layer.

5.4. Results and discussion

5.4.1. Drug spectrum

The different liquids used for this experiment were measured and the results were processed using the processing method mentioned in section 2.5. Note that M in Eq. 2. 9 is a complex number and in the following, we show both the amplitude($|M|$) and phase information of M. The spectrum results for porcine skin are also calculated for comparison. In Fig. 5. (a), from the amplitude spectrum, we can observe that the spectra of the glycerol/water and drug solutions are significantly different from that of porcine skin due to the properties of glycerol especially at low frequencies as the error bar for porcine skin grows with frequency. However, for the phase in Fig. 5. (b), the differences are small. For the refractive index in Fig. 5. 5(a), the drug solution is slightly different from the porcine skin but for the absorption coefficient in Fig. 5. 5 (b), the difference is significant. However, the absorption coefficient is sensitive to any possible air gap between imaging window and sample particularly at higher frequencies and the absorption coefficient is derived by simplifying porcine skin as a single homogenous layer structure which could lead to misleading results as discussed in section 4.3.2 and 4.3.3. The absorption coefficient at 0.6 THz is about 130 cm^{-1}, slightly lower than

that of human skin on the volar forearm, which indicates a similar penetration depth of THz radiation which is around 77 μm. Therefore the amplitude of M ($|M|$) at low frequencies such as 0.3 THz is chosen as the classification parameter to be plotted for the images.

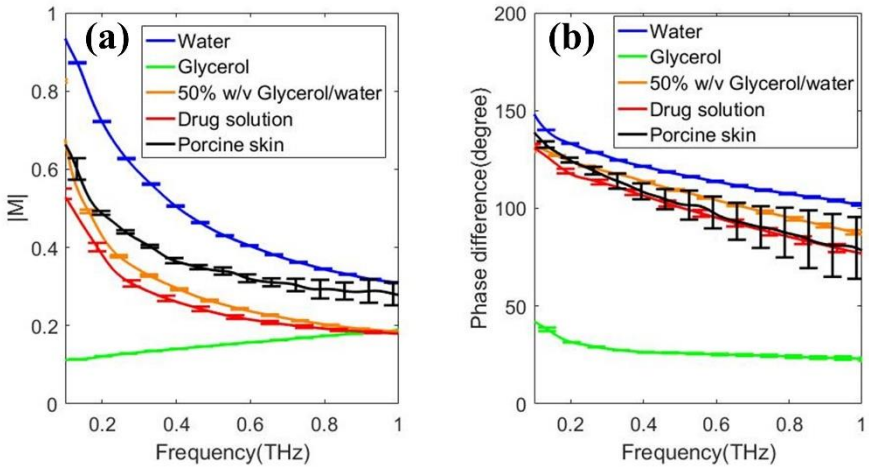

Fig. 5. 4 Spectra of different solutions and fresh porcine skin. (a) Amplitude and (b) Phase difference of M. Note that the error bars are standard deviation of three measurements

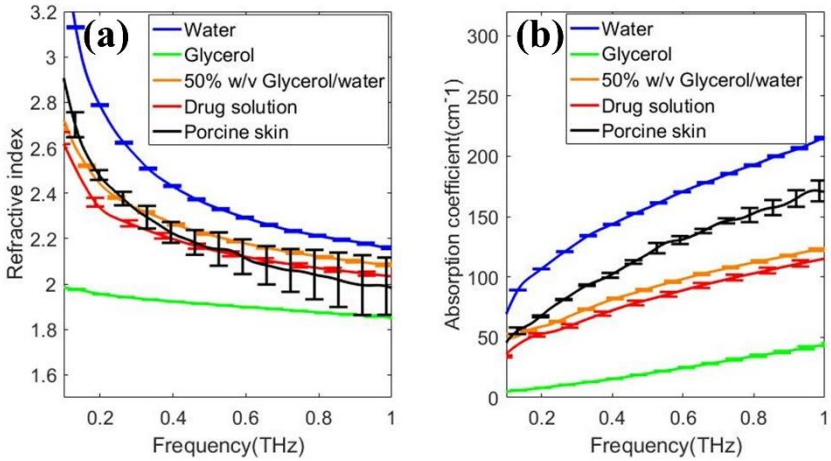

Fig. 5. 5 Spectra of different solutions and fresh porcine skin. (a) Refractive index and (b) Absorption coefficient. Note that the error bars are standard deviation of three measurements

5.4.2. Imaging results

Imaging results can give a better indication of how THz measurements can be applied to investigate transdermal drug delivery. To minimize the variance of

different pieces of porcine skin, the results after treatment need to be normalized to the imaging result acquired before any treatment. Here, the central 25 points from the image were averaged to obtain $\overline{|M|_{before}}$ for the image acquired prior to treatment and then each pixel ($|M_{ij}|_{after}$) in the image acquired after treatment were normalized to $\overline{|M|_{before}}$ to get the normalized amplitude ratio ($|M_{ij}|_{norm}$) as shown in Eq.5. 1.

$$|M_{ij}|_{norm} = \frac{|M_{ij}|_{after} - \overline{|M|_{before}}}{\overline{|M|_{before}}} \quad (5.\ 1)$$

Fig. 5. (a)-(e) show the different treatments effects on the fresh porcine skin and Fig. 5. (f)-(j) show the representative THz imaging results plotted by the normalized amplitude ratio corresponding to the treatment. $|M_{ij}|_{norm}$ decreases on the site where the drug was applied. We can observe that if we first apply the nano-needle patch onto the skin and then use the soaked pad for transdermal drug delivery (result shown in Fig. 5. (i)), $|M_{ij}|_{norm}$ decreases more significantly than if we just use a cotton pad as shown in Fig. 5. (h) as the nano-needle patch increases the permeability of the skin. The microneedle patch does not show much enhancement due to the limited number of needles in one patch.

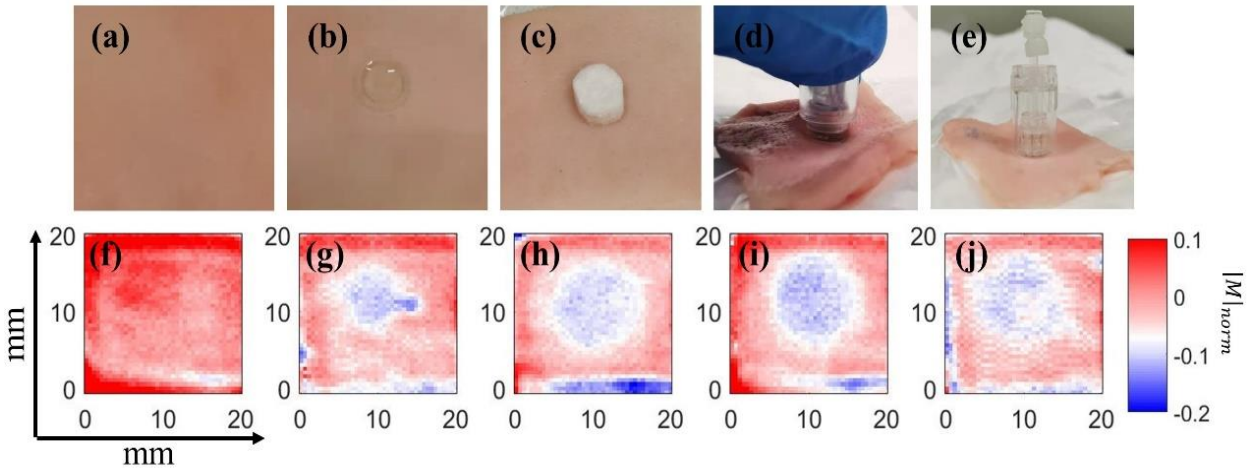

Fig. 5. 6 Imaging result of 5 groups (a,f) control group (b,g) NT group (c,h) PT group (d,i) NN group (e,j) MN group. $|M|_{norm}$ at 0.3 THz is plotted here. Table 5.1 specifies the treatment of each group.

The decease of $|M|$ comes from the increase in the amount of drug solution penetrating into the skin. Using the initial skin parameters of 30% biological background and 70% water (blue curve) with an EMT, we find that $|M|$ decreases when the water volume of the skin is replaced with increasing amounts of the drug, as shown in Fig. 5. . From the calculated results in Fig. 5. , we find that $|M|$ decreases more significantly at the low frequency region when the amount of drug solution inside the skin increases. Based on the results of this theoretical calculation, we can conclude that the amplitude ratio can represent the relative amount of drug solution in the skin, especially in the low frequency region. This verifies our choice to use $|M|$ as the classification parameter to plot the images.

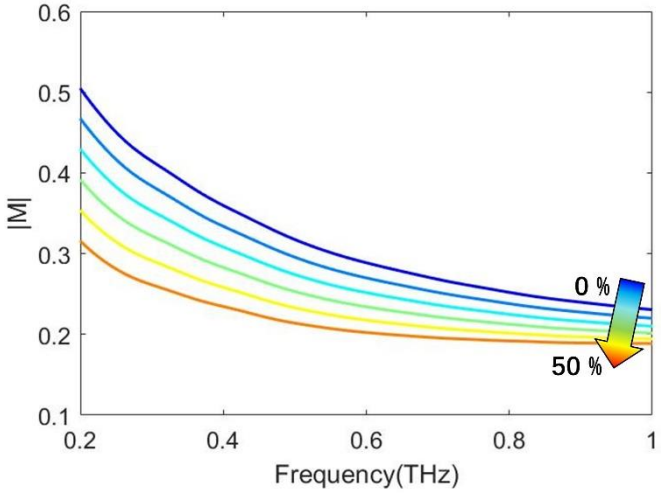

Fig. 5. 7 Theoretical results showing how the amplitude ratio ($|M|$) changes with amount of drug solution increasing from 0 to 50%.

5.4.3. Data analysis

The measurements of the 5 groups were repeated 10 times and we chose the average of the central 25 data points($\overline{|M|_{norm}}$) of the site where the drug was applied as the indicator for further analysis. Fig. 5. (a)-(b) shows how the pixels for the calculation of $|M|_{norm}$ were selected. The normality of the $\overline{|M|_{norm}}$ is checked by Shapiro-Wilk Normality test [97]. We use the one-way ANOVA and Tukey-Kramer tests [98] in MATLAB to check for the significant differences between the groups. The results show that the five groups are significantly different on the level the amplitude ratio decreases ($F=85.05$, $p<0.05$). Fig. 5. (c) shows that after treatment all 4 groups are significantly different compared to the control group. However, group 4 (NN) is significantly different compared to all the other treatment groups and $\overline{|M|_{norm}}$ is the smallest indicating that the nanoneedle patch is the most effective at increasing the efficiency of transdermal drug delivery compared to the other topical application methods tested. Note that

the error bars are the Tukey's minimal significant difference indicating the minimal difference between groups in order to claim significant difference. The red line indicates that $\overline{|M|_{norm}}$ of NN group does not overlap with the other groups.

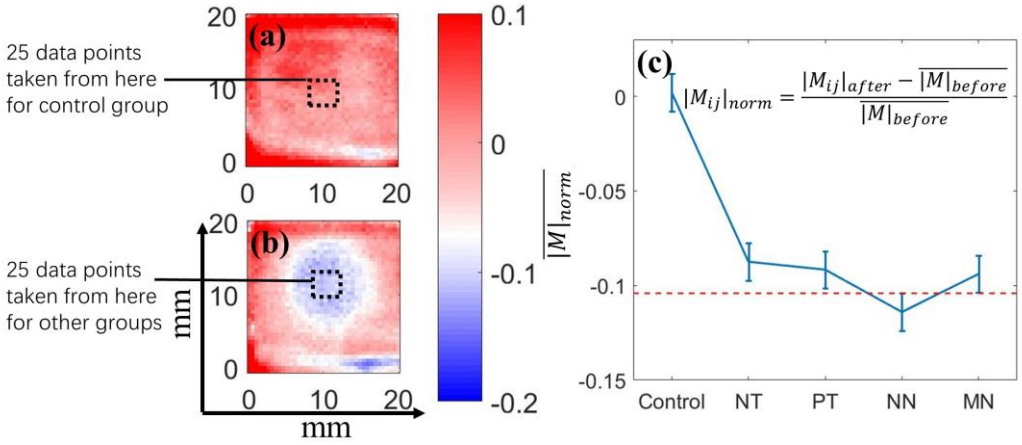

Fig. 5. 8 $|M|_{norm}$ at 0.3 THz before NN treatment and (b) after NN treatment (c)Tukey's Honestly Significant Difference Test of $\overline{|M|_{norm}}$. Error bars are Tukey's minimal significant difference with $\alpha_{Tukey} = 0.05$.

5.5. Summary

In this chapter, we introduced how THz imaging is used to monitor transdermal drug diffusion via topical and micro/nano-needle patch application and compare the efficacy of the application strategies. Statistical methods were used to evaluate the difference between the groups. This work is the first attempt to compare transdermal drug delivery via different application methods with THz imaging as a quantitative imaging technique. The amplitude of the sample to reference ratio at low frequencies can be used as the classification parameter to quantitively represent the drug solution penetrated into skin. The result shows that with a nanoneedle patch, the transdermal drug diffusion is increased. This work

demonstrates that THz imaging could be used as a quantitative in vivo measurement technique to monitor the efficiency of transdermal drug delivery.

6. THz ellipsometry configurations for skin measurement

6.1. Introduction

The above chapters only used THz imaging to study the optical property changes caused by the content variations of the components, such as water. Though Chapter 3 and 4 have used skin models to study SC thickness changes, the study of skin structural changes is still lacking. Moreover, the above mentioned models are based on the assumption that skin is a one-layer/multilayer structure with high homogeneity in each layer. However, studies have found that the SC is composed of flattened corneocytes (the SC cells) and a lipid matrix[99]. The corneocytes are stacked up to 18-20 layers in SC layers with length of corneocyte cells in tens of micrometer scale and thickness less than a micrometer[100]. The "brick and mortar" structure in the SC invalidates the homogeneity assumption in SC. Therefore we expect that the SC gives different response when illuminate by THz light with different polarizations.

The usually used reflection setup provides limited spectral information to extract skin properties and reveal the anisotropic properties of SC as this geometry provides only one set of spectrum information. However, in an anisotropic skin model there are totally 3 sets of complex refractive index to be solved, namely the complex refractive index for the SC in ordinary and extraordinary directions respectively, and the complex refractive index of epidermis. The multi-

configuration geometries that can provide more sets of uncorrelated spectrums are demanded to enable the anisotropic model to be fit. Therefore in this chapter, a multi-configuration ellipsometer system is proposed to study skin changes.

6.2. Experiment setup and protocols

A multi-configuration ellipsometer shown by Fig. 6. 1(a)-(c) is established to provide four sets of independent spectral information. By using a double right-angle prism system, the ellipsometer is able to alter configurations easily. The polarizer is mounted on a motorized rotator to electrically change the polarization of the THz beam. The prism system is made of a Si prism and a gold coated prism which provides perfect reflection. The gold coated prism is symmetrically mounted under the Si prism illustrated in Fig. 6. 1 (a). The emitter, detector, lenses and polarizers are set in transmission geometry shown in Fig. 6. 1 (b). The double prism system is put onto the transmission geometry. Two optical paths are realized by adjusting the height of the prism system. Illustrated in Fig. 6. 1 (a), the incident angle in Si prism is $\theta_{i1} = 56.94^{\circ}$ or $\theta_{i2} = 33.06^{\circ}$ respectively when the THz beam is directly refracted by the upper Si prism, or first reflected by the lower gold coated prism to alter the incident angle into the upper Si prism. The two angles are restricted by the right-angle prisms but one is around the critical angle which enables greater sensitivity to shallow depths of skin, the other is close to the Brewster angle which has higher sensitivity to s- polarized light reflections. The coating thickness is about 200nm which is thick enough to provide a perfect

reflection. Illustrated in Fig. 6. 1 (b), the polarization of the THz beam is controlled by three polarizers. P1 and P3 are fixed at 45° to s- direction. Polarization state of the detected THz beam is controlled only by rotate P2. The technical details of P2 are in reference[101].

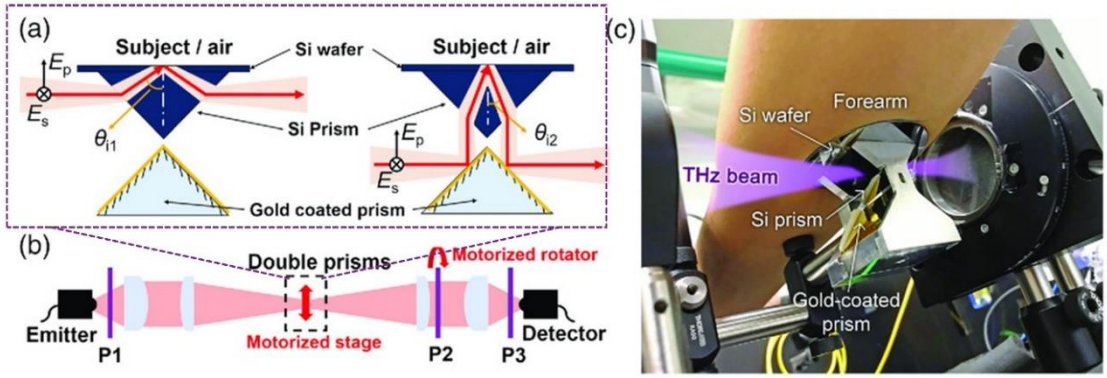

Fig. 6. 1 (a) Double prism system and the two THz optical paths (b) THz transmission geometry for the prism system to be installed (c) a photo of the experimental setup when conducting the measurement

The transmitted electric field ratio ($\rho(w)$) of P2 which is defined by $\rho(w) = E_{blocking}/E_{passing}$ is characterized in Fig. 6.2(a), which is inversely proportional to the extinction ratio ER (Eq. 6.1) of P2.

$$\text{ER}= 20\log\left(\frac{1}{\rho(w)}\right) = 20\log\left(\frac{E_{passing}}{E_{blocking}}\right) \quad (6.\ 1)$$

From Fig.6.2 (b), the magnitude of extinction ratio of P2 is about 20~40dB from 0.1 to 1 THz to ensure a relatively good performance of measurements. .Unlike traditional ellipsometry measurements which characterize the ratio between s- and p- reflections[101], we measured the reference(air) and used the sample to reference ratio under each configuration to characterize the optical properties. . In short, the prism system is used to change incident angle at Si-skin interface and the polarizer (P2) is used to change the polarization of incoming beam so that four

complimentary measurements can be measured easily and reliably. Fig. 6. 1 (c) illustrates the photo when the volar forearm is placed onto the Si prism to conduct *in vivo* measurements.

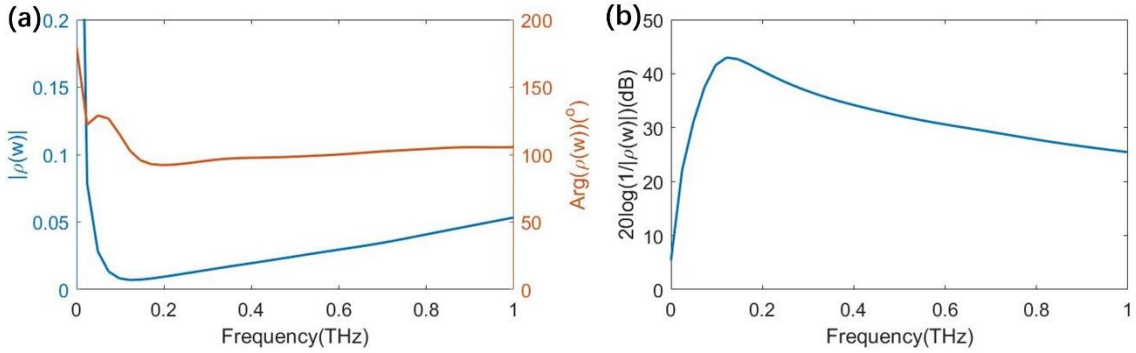

Fig. 6. 2 (a) Graph showing the magnitude and phase of the Transmitted electric field ratio (ρ(w)) of P2 (b) extinction ratio(ER) of P2.

The occlusion process was tested in this system. Subjects were asked to place their volar forearm onto the Si prism for continuous 31 minutes. The target area was placed onto the Si prism for 1 minute prior to the measurement started. During the measurement, the prism system will move up and down as in Fig. 6. 1(a) but the subjects were asked to keep still. In each round, 6 measurements were taken. Firstly, the prism system will be moved to the lowest position by the stage to do p- and s- polarized measurement at θ_{i1}, then stage was moved up by 1.6 cm to conduct p- and s- polarized measurement of skin at θ_{i2}. After that, the prisms were moved up by 2.5 cm to be out of the beam region, hence the transmission measurement in p- and s- polarizations were collected. 5 subjects were measured in total. During the 31 minutes, these steps were repeated for 16 times with 2 minutes for each round. Then subjects were asked to remove their volar forearm and Si-air references were measured by the same protocol.

6.3. Anisotropic skin model

Due to the anisotropy of SC, the optical properties of skin is polarization-dependent. Shown by Fig. 6. 3, the extraordinary direction is perpendicular to the skin surface, while the ordinary direction is parallel to the skin surface. In this work, we modeled skin as a 2-layer structure (SC and epidermis), with the SC layer showing birefringence. Different from the isotopic models of skin mentioned in Chapter 2,3,4, p- and s-reflection coefficients of anisotropic skin model can be expressed using a tri-layer Fresnel model shown by Eq. 6. and 6. .

$$r_p^{Si-Skin} = \frac{E_{rp}^{Si-skin}}{E_{ip}} = \frac{r_p^{Si-SC}+r_p^{SC-EP}exp(-2\beta_p)}{1+r_p^{Si-SC}r_p^{SC-EP}exp(-2\beta_p)} \quad (6.\ 2)$$

$$r_s^{Si-Skin} = \frac{E_{rs}^{Si-skin}}{E_{is}} = \frac{r_s^{Si-SC}+r_s^{SC-EP}exp(-2\beta_s)}{1+r_s^{Si-SC}r_s^{SC-EP}exp(-2\beta_s)} \quad (6.\ 3)$$

Where

$$r_p^{Si-SC} = \frac{\tilde{n}_{SC-o}\tilde{n}_{SC-e}cos\theta_i-\tilde{n}_{Si}\left(\tilde{n}_{SC-e}^2-\tilde{n}_{Si}^2sin^2\theta_i\right)^{1/2}}{\tilde{n}_{SC-o}\tilde{n}_{SC-e}cos\theta_i+\tilde{n}_{Si}\left(\tilde{n}_{SC-e}^2-\tilde{n}_{Si}^2sin^2\theta_i\right)^{1/2}} \quad (6.\ 4)$$

$$r_s^{Si-SC} = \frac{\tilde{n}_{Si}cos\theta_i-\left(\tilde{n}_{SC-o}^2-\tilde{n}_{Si}^2sin^2\theta_i\right)^{1/2}}{\tilde{n}_{Si}cos\theta_i+\left(\tilde{n}_{SC-o}^2-\tilde{n}_{Si}^2sin^2\theta_i\right)^{1/2}} \quad (6.\ 5)$$

$$r_p^{SC-Ep} = \frac{\tilde{n}_{Ep}\left(\tilde{n}_{SC-e}^2-\tilde{n}_{Si}^2sin^2\theta_i\right)^{1/2}-\tilde{n}_{SC-o}\tilde{n}_{SC-e}cos\theta_{Ep}}{\tilde{n}_{Ep}\left(\tilde{n}_{SC-e}^2-\tilde{n}_{Si}^2sin^2\theta_i\right)^{1/2}+\tilde{n}_{SC-o}\tilde{n}_{SC-e}cos\theta_{Ep}} \quad (6.\ 6)$$

$$r_s^{SC-Ep} = \frac{\left(\tilde{n}_{SC-o}^2-\tilde{n}_{Si}^2sin^2\theta_i\right)^{1/2}-\tilde{n}_{Ep}cos\theta_{Ep}}{\left(\tilde{n}_{SC-o}^2-\tilde{n}_{Si}^2sin^2\theta_i\right)^{1/2}+\tilde{n}_{Ep}cos\theta_{Ep}} \quad (6.\ 7)$$

$$\beta_p = \frac{\omega d}{c}\left(\frac{\tilde{n}_{SC-o}}{\tilde{n}_{SC-e}}\right)\left(\tilde{n}_{SC-e}^2-\tilde{n}_{Si}^2sin^2\theta_i\right)^{1/2} \quad (6.\ 8)$$

$$\beta_s = \frac{\omega d}{c}\left(\tilde{n}_{SC-o}^2-\tilde{n}_{Si}^2sin^2\theta_i\right)^{1/2} \quad (6.\ 9)$$

θ_i and θ_{Ep} are the incident angle at the Si-SC interface and refraction angle in the epidermis, respectively. d represents the SC thickness. c is the speed of light. E_{ip} and E_{is} are the p- and s- polarized incident fields, as indicated in Fig. 6. 3 (b). Both ordinary and extraordinary components of the SC affect the p-reflection

coefficient, while only the ordinary component of the SC decides the s-reflection coefficient. The reference reflections r_p^{Si-air} and r_s^{Si-air} with different incident angles in Si prism can be calculated by Eq. 2. 5 and Eq. 2. 6 mentioned in Chapter 2. The sample to reference ratios are then derived with the obtained reflection coefficients. By minimizing the difference between the four theoretical calculations and the corresponding experimental data, we are able to extract $\tilde{n}_{SC-o}$, $\tilde{n}_{SC-e}$ and $\tilde{n}_{Ep}$ which correspond to the complex refractive index of ordinary and extraordinary components of SC and epidermis. However, $\tilde{n}_{SC-o}$, $\tilde{n}_{SC-e}$ and $\tilde{n}_{Ep}$ are frequency-dependent and this causes a larger number of parameters to be determined by fitting. Therefore, the offset exponential (OE) function was used to define $n(\omega)$ shown in Eq. 6. and $k(\omega)$ corresponding to the real part and imaginary part of $\tilde{n}(\omega)$.

$$n(\omega) = ae^{b\omega} + c \tag{6. 10}$$

The OE function has been used to describe dispersive and absorptive materials like water and therefore is also effective to describe tissues[102]. By employing the OE function, the number of unknown parameters are minimized. Then Genetic Algorism is used to determine the parameters with $\Delta\tau$ also to be determined to account for the phase shift due to the temperature changes in Si prism when the arm is placed during measurement. This process is represented by Eq. 6. 1.

$$\rho_{Skin-ref} = \frac{E_{p/s}^{skin}(\theta,w)\times e^{iw\tau_{skin}}}{E_{p/s}^{ref}(\theta,w)\times e^{iw\tau_{ref}}} = \frac{E_{p/s}^{skin}(\theta,w)}{E_{p/s}^{ref}(\theta,w)} \times e^{iw\Delta\tau} \quad (6.\ 1)$$

where $E_{p/s}^{skin}(\theta,w)$ and $E_{p/s}^{ref}(\theta,w)$ are the measured electric field of skin and reference (air) in s-/p- polarization with incident angle in Si prism being either θ_{i1} or θ_{i2}, respectively.

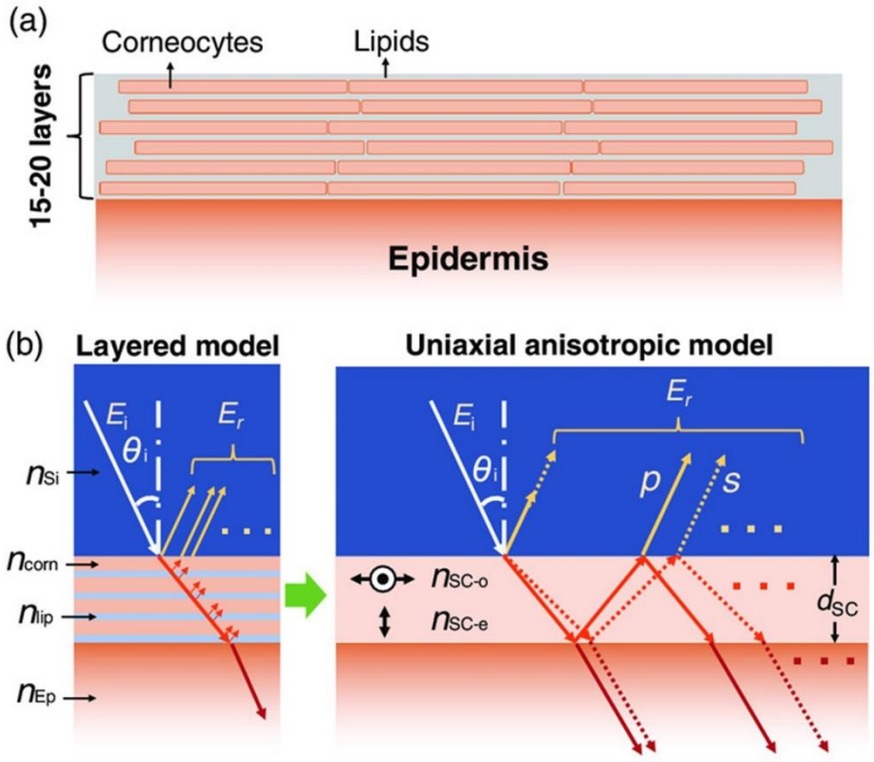

Fig. 6. 3 (a) The "brick and mortar" structure in SC (b) layered model (left) and anisotropic skin model (right)

To compare the equivalence of the anisotropic skin model and layered model shown in Fig. 6.3, we used effective medium theory for a layered structure to calculate the effective ordinary and extraordinary refractive index of SC as shown in Eq. 6.12 and Eq. 6.13.

$$\tilde{n}_{SC-o}{}^2 = f_1\tilde{n}_{corn}{}^2 + f_2\tilde{n}_{lip}{}^2 \quad (6.\ 12)$$

$$\tilde{n}_{SC-e}{}^2 = \frac{1}{f_1/\tilde{n}_{corn}{}^2 + f_2/\tilde{n}_{lip}{}^2} \quad (6.\ 13)$$

Where $\tilde{n}_{corn}$ and $\tilde{n}_{lip}$ refer to the refractive index of corneocyte and lipid respectively while f_1 and f_2 are the fraction of each layer respectively. By Fresnel equations, we are able to calculate the surface reflection of skin for the layered model with given refractive index of corneocyte and lipid shown in Fig. 6.4(a) and (b) and the thickness of each layer being 0.9 μm and 0.4 μm for corneocyte and lipid layers. The surface reflection of anisotropic skin model is also calculated based on the equivalent ordinary and extraordinary refractive index of SC and compared with the layered model. The reflection ratios of both models under different geometries are almost identical as shown in Fig. 6.4(c) and (d). This indicates the feasibility of the anisotropic skin model.

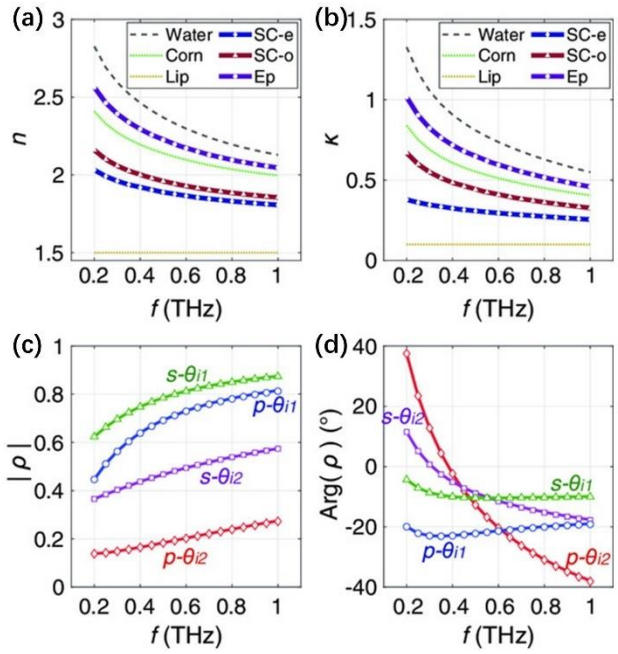

Fig. 6.4 (a)Refractive index (b) extinction coefficient of water, corneocyte, lipid, SC in ordinary direction, SC in extraordinary direction and epidermis (c) amplitude ratio (d) phase difference of reflection of layered model(symbols) and anisotropic model (solid curves).

6.4. Results and discussion

6.4.1. Verification of the model

The proposed anisotropic skin model is then applied to fit the measured data to verify the proposed model is equivalent to the measurement. The discrete symbols

in Fig. 6. (a) and Fig. 6. (b) illustrate the measured signal ratios at different geometries when skin has been occluded for 30 minutes and the solid curves are the fitting results. The good agreement between measured and fitting results verifies the proposed anisotropic skin model. Fig. 6. (b) and (c) are the fitted refractive index ($n(\omega)$) and extinction coefficient ($k(\omega)$) of SC in ordinary and extraordinary directions and epidermis. A clear deviation between the indices of ordinary and extraordinary components of SC indicates the property difference and birefringence of SC. Moreover, the value of both $n(\omega)$ and $k(\omega)$ of epidermis are higher than that of SC in both directions which agrees with the reported knowledge about the water gradient in skin. $n(\omega)$ and $k(\omega)$ of water are also shown in Fig. 6. (c) and (d) and have the largest values compared to that of SC and epidermis.

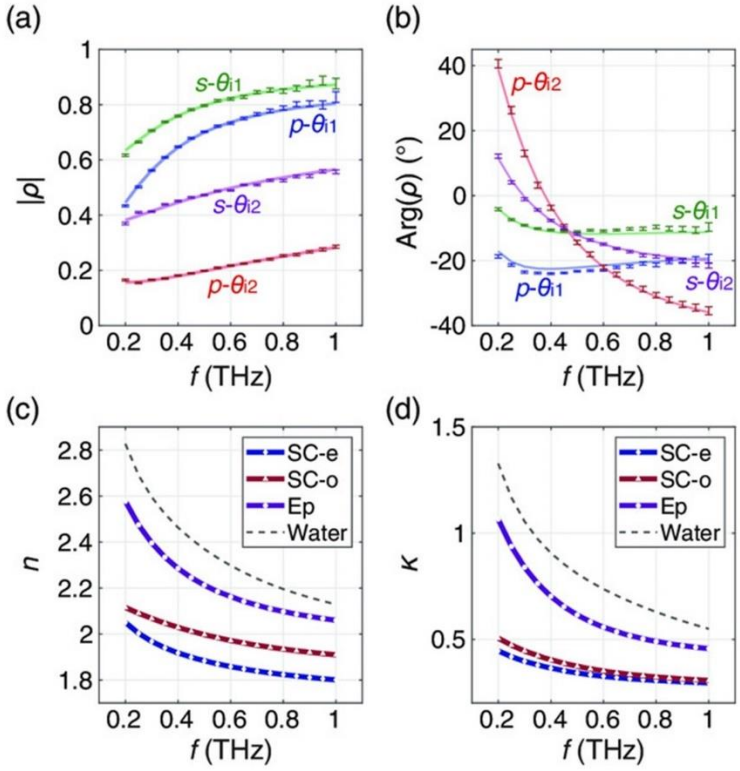

Fig. 6. 5 (a) Amplitude of signal ratios (b) Phase difference of signal ratios (c) refractive index (d) extinction coefficient of ordinary and extraordinary components of SC, epidermis and water. Note that the error bar in (a) and (b) are caused by the noise.

6.4.2. Occlusion process observed by THz ellipsometry

Fig. 6. shows the changes in the refractive index and extinction coefficient of the ordinary and extraordinary components of SC and epidermis during the 31 minute measurement. Both the refractive index and extinction coefficient of the SC in ordinary and extraordinary directions increase with occlusion time. However, the spectrums of epidermis remain almost the same. The obtained result indicates that the occlusion only altered the state of the SC but did not affect epidermis much. To better compare the optical indices difference between ordinary and extraordinary directions of the SC and epidermis, the refractive index and extinction coefficient at 0.6 THz of 5 subjects during the occlusion are shown in Fig. 6. (a) and (b). During the 31 minutes, the refractive index and extinction coefficient of epidermis stayed unchanged while the indices of the SC ordinary and extraordinary components increased gradually. Moreover, the optical indices for the SC in different directions (ordinary and extraordinary) show clear differences. This verifies the birefringent property of the SC.

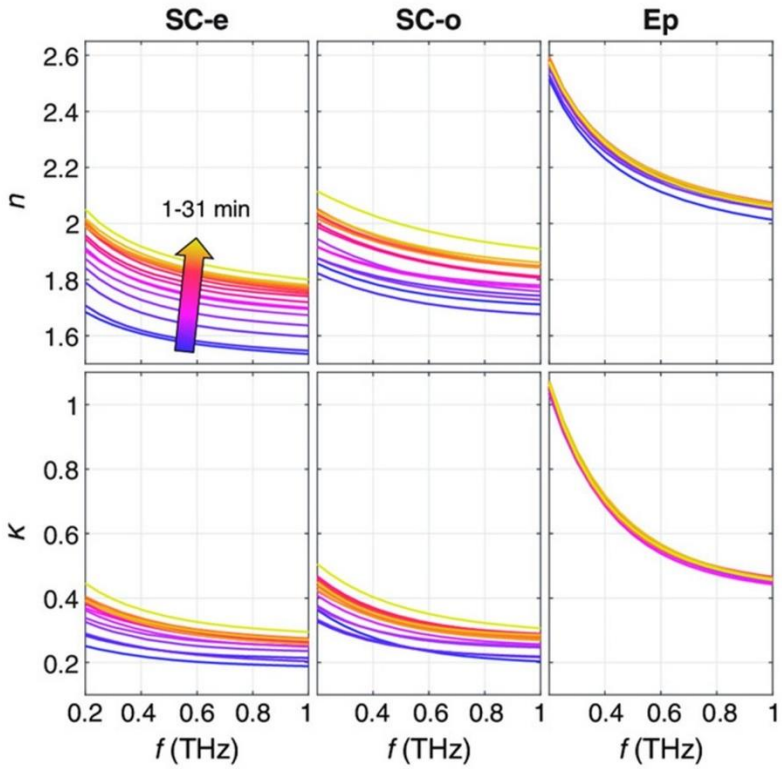

Fig. 6. 6 Refractive index and extinction coefficient spectrums of SC in extraordinary and ordinary direction and epidermis during occlusion process

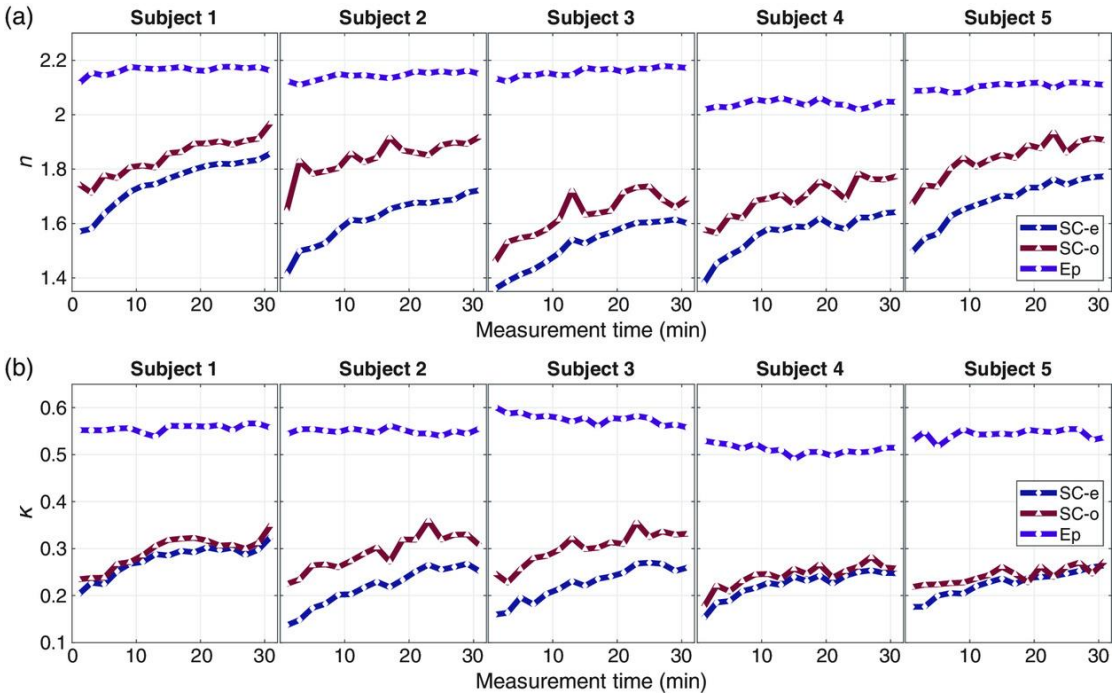

Fig. 6. 7 (a)Refractive index and (b)extinction coefficient at 0.6 THz of SC in extraordinary and ordinary direction and epidermis of the 5 subjects during the 31-minute occlusion test

6.4.3. Dispersion and birefringence

Usually, the hydration level in skin is represented by the refractive index and extinction coefficient which can be understood by the EMT mentioned in section 2.6. However, this may not be true in anisotropic skin models. Illustrated in Fig. 6. , the relative positions of spectrums of SC in ordinary and extraordinary directions from different subjects vary a lot. To better quantify the changes in hydration and structure of SC, we define dispersion and birefringence.

As mentioned above in Fig. 2. *10*, optical property values of dehydrated skin is almost constant in frequency domain, while water is highly dispersive and the complex refractive index decreases with frequency. Therefore, the dispersion of skin optical properties is positively correlated with the water content in skin. Dispersion is defined by the difference between first and last frequency point shown by Eq. 6. .

$$\text{Dispersion} = |\tilde{n}_{SC-e}(\omega_1) - \tilde{n}_{SC-e}(\omega_m)| \tag{6. 2}$$

ω_1 and ω_m refer to frequencies at 0.2 THz and 1 THz respectively.

The inhomogeneity of SC is reflected by the difference between ordinary and extraordinary components of SC. Therefore Eq. 6. and Eq. 6. define the nBir and kBir, respectively. Larger values indicate a higher inhomogeneity.

$$nBir = \sum_{w_1}^{w_m}[n_{SC-o}(w) - n_{SC-e}(w_m)]/m \quad (6.\ 3)$$

$$kBir = \sum_{w_1}^{w_m}[k_{SC-o}(w) - k_{SC-e}(w_m)]/m \quad (6.\ 4)$$

The calculated dispersion and birefringence of the subjects are shown in Fig. 6. . Dispersion of all the 5 subjects shows a remarkable increase trend during the 31 minute occlusion. The increased value of dispersion means the increased hydration level in SC. The decreased value of nBir indicates the decreased inhomogeneity of SC during the occlusion. However, kBir does not decrease as much as nBir. This can be explained by the two aspects of inhomogeneity of the SC: intercellular and depth inhomogeneity which refer to the effective n and k difference between the corneocytes and the lipid matrix, and effective n and k variation across the SC depth, respectively. Both refractive index of lipid (n_{lip}) and corneocytes (n_{corn}) increase with occlusion time. Thus, the intercellular inhomogeneity of n does not change much but the depth inhomogeneity decreases because the surface effective n increases, therefore the effective n has a less gradient across the depth. Therefore, the total inhomogeneity of n is reduced. However, the increased extinction coefficient of corneocytes (k_{corn}) increases the intercellular inhomogeneity but decreases the depth inhomogeneity as that of lipid (k_{lip}) is considered to be 0. Therefore, nBir decreases more significantly.

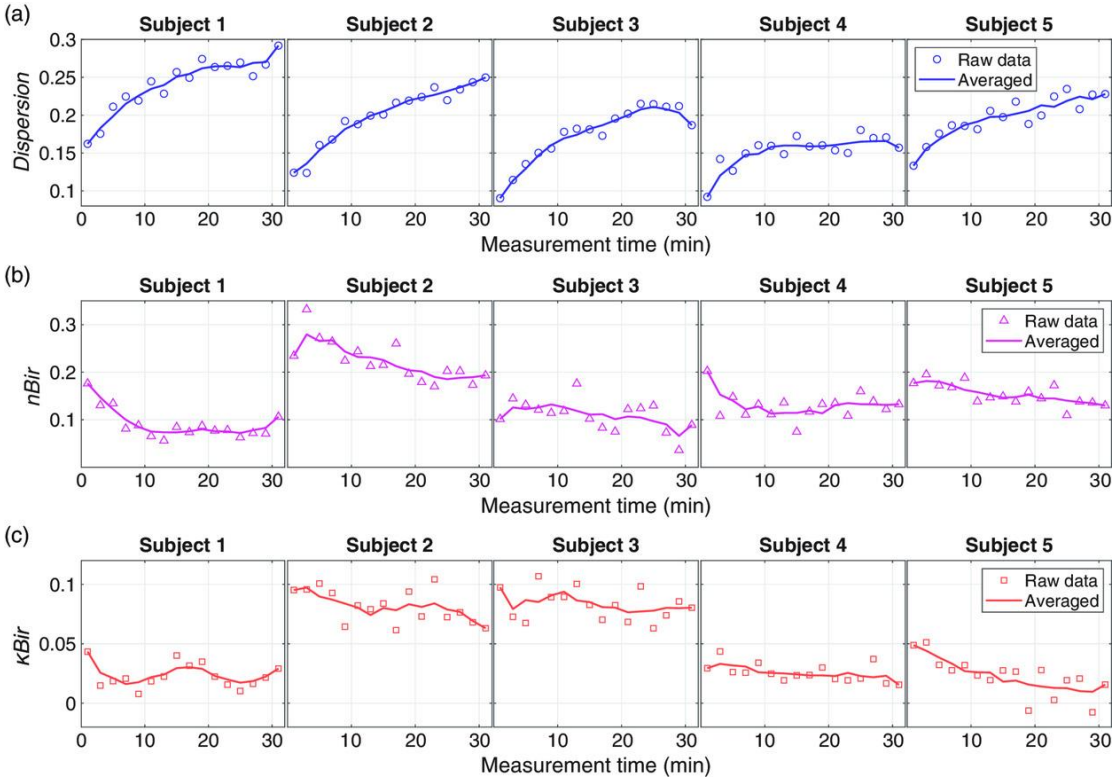

Fig. 6. 8 (a)Dispersion (b) nBir and (c) kBir of SC of the 5 subjects during the 31-minute occlusion test.

6.4.4. Application

The defined dispersion and birefringence of SC can be used to evaluate the effect of skin product. Commercialized bio-oil was used in the demonstration of how THz ellipsometer was used for skin treatment monitoring. Totally 3 tests were conducted with test 1 and 3 on the same subject in different months and test 2 on another subject. During the measurement, 60 μl bio-oil was applied to the target area for each test.

Skin was measured 3 times before any oil was applied onto the skin. After application of the bio-oil, skin was remeasured at 10 minutes, 20 minutes,30 minutes, 1 hour and 2 hours to observe the hydration and structure changes of skin. Note that different from the previous occlusion measurement in which skin

was measured continuously for 31 minutes, only 1 measurement was conducted at each time points and after each measurement skin was removed from the Si prism. Illustrated in Fig. 6. , refractive index (n) and extinction coefficient (k) at 0.6 THz was plotted with the measurement time. After application of the bio-oil, all the n in the three tests shows a clear increase of both ordinary and extraordinary components of SC. However, this trend is less pronounced for k with a slightly distinct increase trend in extraordinary component. Both n and k maintain constant for epidermis. Dispersion and birefringence were also calculated in Fig. 6. to understand the hydration and structure changes in skin. For all the three tests, dispersion increases remarkably after application of bio-oil indicating the increased hydration in SC. However, the hydration does not continue increasing with time for all the tests as shown by Fig. 6. . Test 2 shows higher starting value of dispersion indicating higher initial hydration of SC for test 2. nBir decreases a little bit for all the 3 tests. However, only test 1 and 3 show decreased kBir after application of bio-oil.

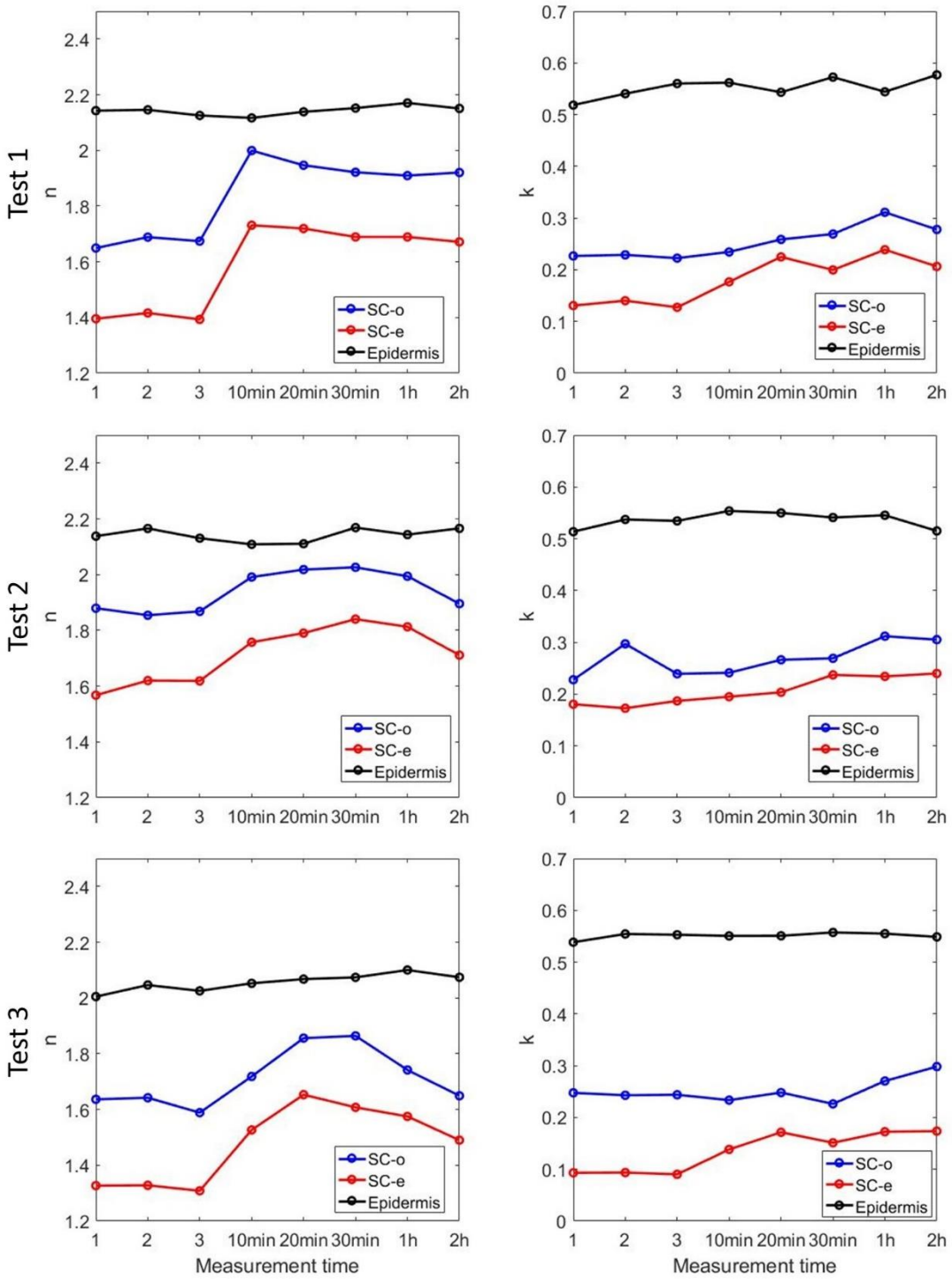

Fig. 6. 9 Refractive index (n) and extinction coefficient (k) at 0.6 THz of different time points before and after application of the bio-oil of the three tests. Note that the first three measurements were conducted before application of bio-oil. Test 1 and 3 were on the same subject in different months and test 2 was on another subject.

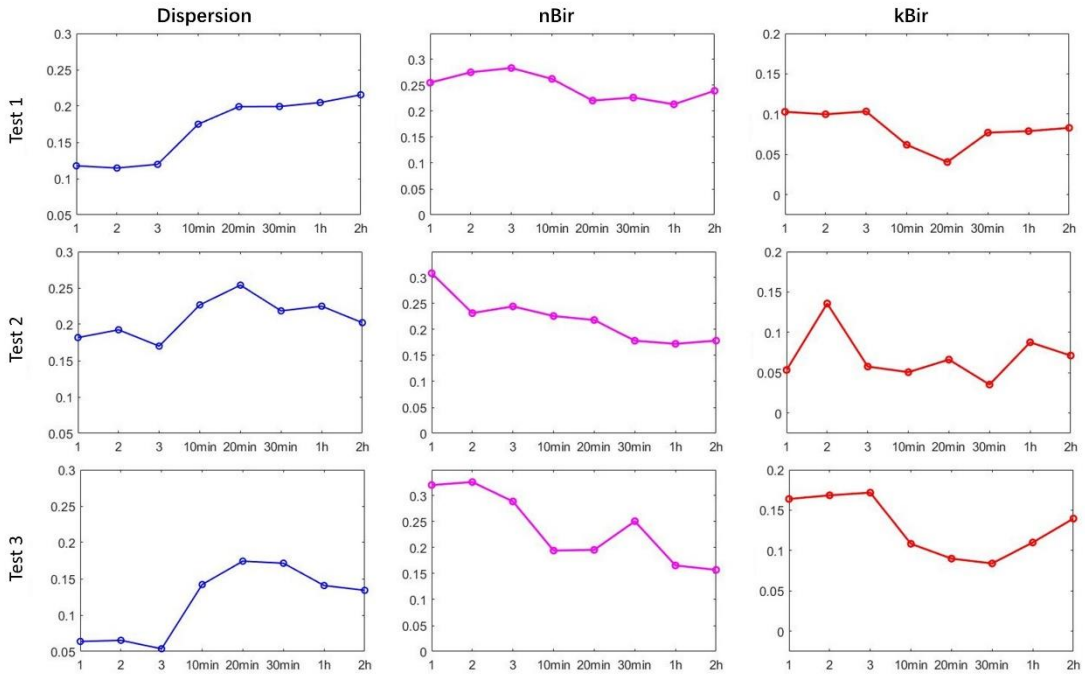

Fig. 6. 10 Dispersion, nBir and kBir before and after application of the bio-oil of the three tests. Note that the first three measurements were conducted before application of bio-oil. Test 1 and 3 were on the same subject in different months and test 2 was on another subject.

6.5. Summary

In this chapter, THz ellipsometry configurations are introduced to study both the hydration and structure of skin. Unlike other typical THz-TDS system, a double prism system is integrated to enable multiple incident angles onto the skin. Polarizers are also used to provide s- and p- polarized light. The signals obtained in this setup contains more information and therefore can be used to study the complex skin structure. With our proposed anisotropic skin model, SC shows a birefringent property. Therefore, dispersion and birefringence are also introduced to characterize the hydration and structure of SC. The 31-minute occlusion process was monitored and the changes of skin after applying bio-oil was also studied. The

proposed THz ellipsometer has the potential to be used to study not only the hydration but also the structure of skin.

7. Summary and future work

7.1. Summary of the thesis

In this thesis, typical THz imaging and spectroscopy methods are introduced and employed for skin characterization. The work mainly includes studying the variables which affect *in vivo* measurements of the skin taken with a THz-TDS system, establishing a robust protocol for such applications, potential future applications and instrumentation for better characterization.

In the first two chapters, THz imaging techniques and current medical applications and advances are introduced. The theories and data processing methods are presented. Most of this thesis is focused on skin characterization. Therefore, current skin modelling approaches are also introduced.

Chapter 3 introduces the variables that affect THz i*n vivo* skin measurements. An imaging window is usually employed to help align the optics and position the target area of skin, this causes occlusion and mechanical deformation of skin. Along with other parameters such as skin type, climate and environment, the effect of occlusion during the measurement is also briefly introduced. However, the contact pressure between skin and the imaging window will significantly alter the THz response of skin. The change induced by contact pressure is systematically studied including the THz pulse response, optical indices and imaging, by installing pressure sensors. To better understand what is happening inside the skin, a stratified media model combined with effective medium theory is used to

extract the changes in the hydration and thickness of the SC thickness. In order to get consistent results, a protocol considering occlusion and contact pressure is proposed. Normalization is also recommended to eliminate other variables.

Chapter 4 and 5 explore the application of THz imaging to skin assessment. Silicone gel sheet (SGS) is used to treat abnormal scars by providing occlusion effects and in Chapter 4, we use a THz-TDS system to monitor the hydration changes in skin after the application of SGS. The fluidic shifts and lateral diffusion were measured throughout the application of the SGS and the recovery of the skin after it had been removed. A two-layer skin model is also used to extract the hydration profile in the SC. Transdermal drug delivery which avoids gastrointestinal side effects is monitored using a THz-TDS system in Chapter 5. Several topical application methods including direct topical application, using a drug-soaked cotton pad for topical application, employing micro/nano-needle patches to help enhance the permeability of skin. The result shows that THz imaging is able to monitor the efficiency of transdermal drug delivery and among the tested application methods, the nano-needle patch shows the best performance.

The above chapters mainly use THz pulse information and spectrum information to monitor skin changes in terms of hydration and layer thickness. However, the ability of a THz-TDS system to study skin structure is not sufficiently demonstrated. The anisotropic properties of the SC caused by the lamellar structure were introduced in Chapter 6. By using a double prism system, four configurations involving two incident angles and two polarizations can be achieved

during the *in vivo* skin measurements. Dispersion and birefringence are defined to represent the hydration and inhomogeneity of the SC. The occlusion process by the prism during the 31-minute measurement is demonstrated as well as the changes caused by the application of bio-oil. Both show that the hydration of the SC increased and inhomogeneity decreased following the application of the bio-oil.

In Chapters 3, 4 and 6, different skin models are applied in order to study the properties of skin. However, there are some limitations that should be noted when employing these models. Table 7.1 summarizes the merits and limitations of the different skin models.

Table 7.1. Merits and limitations of different models

Model	Merits	Limitations
Double Debye model (Chapter 2)	Extraction of physical properties Very little prior knowledge needed	Accuracy for dry tissues is questionable.
Effective medium theory (Chapter 2)	Direct extraction of the hydration Very few fitting parameters	A prior knowledge on the dehydrated skin needed Based on assumption that skin is homogeneous
Single-layer model (Chapter 2)	Simple calculation and characterization	Oversimplification Cannot resolve different layers of skin Not comparable among different setups
Double-layer model (Chapter 4)	Differentiation of SC and epidermis Good accuracy	Dielectric models (EMTs) needed
Stratified media model / Fresnel Theory (Chapter 2 and 3)	Clear water concentration distribution Good consistency with Raman spectroscopy	Pre-defined water gradient needed Calculation complexity

Anisotropic SC model (Chapter 6)	No dielectric model used Both hydration and structural information obtained Birefringence of SC considered	Multiple uncorrelated measurements needed

7.2. Future work

The variety of models and measurement protocols results in divergent results being obtained in different THz *in vivo* skin measurements, providing obstacles against comparison between different works. For example, by using different refractive indices of dehydrated skin illustrated in Fig. 2. *10* as an input for the skin model, the extracted water concentration can be different. Consistent measurement protocol is another important factor to ensure consistent results between different works [77]. Variables such as applied pressure and occlusion time should be carefully controlled as they significantly affect the reflectivity. Due to the rapid changes of water dynamics inside skin, current *in vivo* studies of skin are mostly point scan or line-scan [48,103]. Therefore, a faster, more accurate THz system is in high demand to ensure the accuracy of measurements before skin models are applied to interpret more complex applications such as drug diffusion. However, the high cost of a multi-pixel THz camera is preventing the system from being widely used commercially. Therefore, a cost-effective single-pixel THz camera combined with a digital micro-mirrors device might be preferable for real world applications[104]. Drug diffusion along lateral and vertical directions could

possibly be monitored by such a camera. The medical screening ability of THz imaging will also be enhanced by a decrease in the imaging time and cost.

Apart from consistent THz measurement protocol and improvement of the THz imaging system, the algorithms used for parameter extraction when modeling skin also play an important part. For example, when treating skin as a one-layer or double-layer structure and applying EMTs to extract the hydration of the skin, the solution would be simple and easy to extract. However, when it goes to a multi-layer structure, the number of parameters used to represent skin hydration will increase, bringing greater complexity for computing the solution. Due to the development of heuristic algorithms, optimization methods used for the solution search has been enhanced. Clegg et al. employed genetic algorithms to effectively find the best values of the multi-Debye parameters of tissues in the GHz regime[105,106]. Ding et al. further combined the genetic algorithm to improve the extraction of the double Debye parameters in the THz regime[107]. Bao et al. have developed a branch and bounding (BB) method of global optimization for double Debye model parameter extraction[52,108,109]. Yang et al. have employed particle swarm optimization techniques to extract the double Debye parameters of collagen[110]. Therefore, these algorithms can also be potentially utilized in extracting multi-layer skin parameters.

With the variables affecting in vivo skin measurement and protocols proposed to account for the effects, consistent measurement results are ensured to make meaningful comparison between studies and be applied for various applications.

With development of instrumentation of THz systems and algorithms for extracting skin model parameters, the ability of a typical THz-TDS system to study skin or tissues can also be enhanced.

Bibliography

1. D. H. Auston, K. P. Cheung, and P. R. Smith, "Picosecond photoconducting Hertzian dipoles," Appl. Phys. Lett. **45**(3), 284 (1984).

2. X. Yang, X. Zhao, K. Yang, Y. Liu, Y. Liu, W. Fu, and Y. Luo, "Biomedical Applications of Terahertz Spectroscopy and Imaging," Trends Biotechnol. **34**(10), 810–824 (2016).

3. R. M. Woodward, V. P. Wallace, B. E. Cole, R. J. Pye, D. D. Arnone, E. H. Linfield, and M. Pepper, "Terahertz Pulse Imaging in reflection geometry of skin tissue using time domain analysis techniques," in *Clinical Diagnostic Systems: Technologies and Instrumentation* (2002), pp. 160–169.

4. S. Fan, B. S. Y. Ung, E. P. J. Parrott, V. P. Wallace, and E. Pickwell-MacPherson, "In vivo terahertz reflection imaging of human scars during and after the healing process," J. Biophotonics **10**(9), 1143–1151 (2017).

5. K. Cal, J. Stefanowska, and D. Zakowiecki, "Current tools for skin imaging and analysis," Int. J. Dermatol. **48**, 1283–1289 (2009).

6. D. Rallan and C. C. Harland, "Skin imaging: Is it clinically useful?," Clin. Exp. Dermatol. **29**, 453–459 (2004).

7. A. Boyd, O. Cain, A. Chauhan, and G. J. Webb, "Medical liver biopsy: background, indications, procedure and histopathology," Frontline Gastroenterol. **11**(1), 40–47 (2020).

8. R. Alvarez-Román, A. Naik, Y. N. Kalia, H. Fessi, and R. H. Guy, "Visualization of skin penetration using confocal laser scanning microscopy," Eur. J. Pharm. Biopharm. **58**(2), 301–316 (2004).

9. N. S. White and R. J. Errington, "Fluorescence techniques for drug delivery research: Theory and practice," Adv. Drug Deliv. Rev. **57**(1), 17–42 (2005).

10. B. A. I. Van Den Bergh, D. C. Swartzendruber, A. Bos-Van Der Geest, J. J. Hoogstraate, A. H. G. J. Schrijvers, H. E. Boddé, H. E. Junginger, and J. A. Bouwstra, "Development of an optimal protocol for the ultrastructural examination of skin by transmission electron microscopy," J. Microsc. **187**(2), 125–133 (1997).

11. L. T. Kilpatrick-Liverman, P. Kazmi, E. Wolff, and T. G. Polefka, "The use of near-infrared spectroscopy in skin care applications," Ski. Res. Technol. **12**(3), 162–169 (2006).

12. L. Franzen and M. Windbergs, "Applications of Raman spectroscopy in skin research - From skin physiology and diagnosis up to risk assessment and dermal drug delivery," Adv. Drug Deliv. Rev. (2015).

13. N. Nakagawa, M. Matsumoto, and S. Sakai, "In vivo measurement of the water content in the dermis by confocal Raman spectroscopy," Ski. Res. Technol. **16**(2), 137–141 (2010).

14. P. J. Caspers, G. W. Lucassen, and G. J. Puppels, "Combined in vivo confocal Raman spectroscopy and confocal microscopy of human skin," Biophys. J. **85**(1), 572–580 (2003).

15. N. Kollias and G. N. Stamatas, "Optical non-invasive approaches to diagnosis of skin diseases," in *Journal of Investigative Dermatology Symposium Proceedings* (2002).

16. N. Nagai, R. Kumazawa, and R. Fukasawa, "Direct evidence of inter-molecular vibrations by THz spectroscopy," Chem. Phys. Lett. (2005).

17. M. Tonouchi, "Cutting-edge terahertz technology," Nat. Photonics (2007).

18. A. Mirbeik-Sabzevari and N. Tavassolian, "Ultrawideband, Stable Normal and Cancer Skin Tissue Phantoms for Millimeter-Wave Skin Cancer Imaging," IEEE Trans. Biomed. Eng. **66**(1), 176–186 (2019).

19. E. C. Fear, "Microwave imaging of the breast," Technol. Cancer Res. Treat. **4**(1), 69–82 (2005).

20. A. Y. Owda, N. Salmon, A. J. Casson, and M. Owda, "The reflectance of human skin in the millimeter-wave band," Sensors (Switzerland) **20**(5), 1480 (2020).

21. J. Welzel, E. Lankenau, R. Birngruber, and R. Engelhardt, "Optical coherence tomography of the human skin," J. Am. Acad. Dermatol. **37**(6), 958–963 (1997).

22. M. Schwartz, A. Levine, and O. Markowitz, "Optical coherence tomography in dermatology," Cutis **18**(6), 061224 (2017).

23. F. Mirrashed and J. C. Sharp, "In vivo morphological characterisation of skin by MRI micro-imaging methods," Ski. Res. Technol. **10**(3), 149–160 (2004).

24. C. Xu, X. Wang, and M. Pramanik, *Imaging Technologies and Transdermal Delivery in Skin Disorders* (2019).

25. H. A. E. Benson and A. C. Watkinson, *Transdermal and Topical Drug Delivery: Principles and Practice* (2012).

26. B. E. Cole, R. M. Woodward, D. A. Crawley, V. P. Wallace, D. D. Arnone, and M. Pepper, "Terahertz Imaging and Spectroscopy of Human Skin, In-vivo," in *Commercial and Biomedical Applications of Ultrashort Pulse Lasers; Laser Plasma Generation and Diagnostics* (2001), p. 4276.

27. A. Böhling, S. Bielfeldt, A. Himmelmann, M. Keskin, and K. P. Wilhelm, "Comparison of the stratum corneum thickness measured in vivo with confocal Raman spectroscopy and confocal reflectance microscopy," Ski. Res. Technol. **20**(1), 50–57 (2014).

28. I. Echchgadda, J. A. Grundt, M. Tarango, B. L. Ibey, T. Tongue, M. Liang, H. Xin, and G. J. Wilmink, "Using a portable terahertz spectrometer to measure the optical properties of in vivo human skin," J. Biomed. Opt. **18**(2), 120503 (2013).

29. B. B. Hu and M. C. Nuss, "Imaging with terahertz waves," Opt. Lett. **20**(16), 1716–1718 (1995).

30. V. P. Wallace, A. J. Fitzgerald, E. Pickwell, R. J. Pye, P. F. Taday, N. Flanagan, and H. A. Thomas, "Terahertz pulsed spectroscopy of human basal cell carcinoma," Appl. Spectrosc. **60**(10), 1127–1133 (2006).

31. W. G. Yeo, O. Gurel, C. L. Hitchcock, S. Park, K. Sertel, and N. K. Nahar, "Evaluation of cancer tissue morphology via THz spectroscopic imaging: Human lung and small intestine malignancies," Infrared Phys. Technol. **97**, 411–416 (2019).

32. Y. He, K. Liu, C. Au, Q. Sun, E. P. J. Parrott, and E. Pickwell-MacPherson, "Determination of terahertz permittivity of dehydrated biological samples," Phys. Med. Biol. **62**, 8882–8893 (2017).

33. V. P. Wallace, A. J. Fitzgerald, S. Shankar, N. Flanagan, R. Pye, J. Cluff, and D. D. Arnone, "Terahertz pulsed imaging of basal cell carcinoma ex vivo and in vivo," Br. J. Dermatol. **151**(2), 424–432 (2004).

34. Z. D. Taylor, R. S. Singh, M. O. Culjat, J. Y. Suen, W. S. Grundfest, H. Lee, and E. R. Brown, "Reflective terahertz imaging of porcine skin burns," Opt. Lett. **33**(11), 1258–1260 (2008).

35. N. Bajwa, S. Sung, D. B. Ennis, M. C. Fishbein, B. N. Nowroozi, D. Ruan, A. MacCabi, J. Alger, M. A. S. John, W. S. Grundfest, and Z. D. Taylor, "Terahertz Imaging of Cutaneous Edema: Correlation with Magnetic Resonance Imaging in Burn Wounds," IEEE Trans. Biomed. Eng. **64**(11), 2682–2694 (2017).

36. S. Sung, S. Selvin, N. Bajwa, S. Chantra, B. Nowroozi, J. Garritano, J. Goell, A. D. Li, S. X. Deng, E. R. Brown, W. S. Grundfest, and Z. D. Taylor, "THz Imaging System for in vivo Human Cornea," IEEE Trans. Terahertz Sci. Technol. **8**(1), 27–37 (2018).

37. G. G. Hernandez-Cardoso, S. C. Rojas-Landeros, M. Alfaro-Gomez, A. I. Hernandez-Serrano, I. Salas-Gutierrez, E. Lemus-Bedolla, A. R. Castillo-Guzman, H. L. Lopez-Lemus, and E. Castro-Camus, "Terahertz imaging for early screening of diabetic foot syndrome: A proof of concept," Sci. Rep. **7**(42124), (2017).

38. K. W. Kim, K.-S. Kim, H. Kim, S. H. Lee, J.-H. Park, J.-H. Han, S.-H. Seok, J. Park, Y. Choi, Y. Il Kim, J. K. Han, and J.-H. Son, "Terahertz dynamic imaging of skin drug absorption," Opt. Express **9**(20), 9476–9484 (2012).

39. K. W. Kim, H. Kim, J. Park, J. K. Han, and J. H. Son, "Terahertz tomographic imaging of transdermal drug delivery," IEEE Trans. Terahertz Sci. Technol. **1**(2), 99–106 (2012).

40. D. H. Auston, "Picosecond optoelectronic switching and gating in silicon," Appl. Phys. Lett. **26**(3), 101–103 (1975).

41. X.-C. Zhang and J. Xu, *Introduction to THz Wave Photonics* (Springer, 2010).

42. A. Bonvalet, M. Joffre, J. L. Martin, and A. Migus, "Generation of ultrabroadband femtosecond pulses in the mid-infrared by optical rectification of 15 fs light pulses at 100 MHz repetition rate," Appl. Phys. Lett. **67**(20), 2907–2909 (1995).

43. Q. Meng, R. Ye, Z. Zhong, J. Yu, and B. Zhang, "Analysis on THz Radiation Generation Efficiency in Optical Rectification by Tilted-Pulse-Front Pumping," J. Infrared, Millimeter, Terahertz Waves **36**, 866–875 (2015).

44. R. L. Ives, "Microfabrication of high-frequency vacuum electron devices," IEEE Trans. Plasma Sci. **32**(3), 1277–1291 (2004).

45. P. Dean, A. T. imaging using quantum cascade lasers-A. review of systems and applications Valavanis, J. Keeley, K. Bertling, Y. L. Lim, R. Alhathlool, A. D. Burnett, L. H. Li, S. P. Khanna, D. Indjin, T. Taimre, A. D. Rakić, E. H. Linfield, and A. G. Davies, "Terahertz imaging using quantum cascade lasers - A review of systems and applications," J. Phys. D. Appl. Phys. **47**(37), 374008 (2014).

46. A. Rogalski and F. Sizov, "Terahertz detectors and focal plane arrays," Opto-electronics Rev. **19**, 340–404 (2011).

47. Y. J. Lin and M. Jarrahi, "Heterodyne terahertz detection through electronic and optoelectronic mixers," Reports Prog. Phys. **83**(6), 066101 (2020).

48. X. Chen, Q. Sun, J. Wang, H. Lindley-Hatcher, and E. Pickwell-MacPherson, "Exploiting Complementary Terahertz Ellipsometry Configurations to Probe the Hydration and Cellular Structure of Skin In Vivo," Adv. Photonics Res. **2000024**, (2021).

49. D. B. Bennett, W. Li, Z. D. Taylor, W. S. Grundfest, and E. R. Brown, "Stratified media model for Terahertz reflectometry of the skin," IEEE Sens. J. **11**(5), 1253–1262 (2011).

50. E. Pickwell, B. E. Cole, A. J. Fitzgerald, M. Pepper, and V. P. Wallace, "In vivo study of human skin using pulsed terahertz radiation," Phys. Med. Biol. (2004).

51. E. Pickwell, B. E. Cole, A. J. Fitzgerald, V. P. Wallace, and M. Pepper, "Simulation of terahertz pulse propagation in biological systems," Appl. Phys. Lett. **84**(12), 2190–2192 (2004).

52. B. C. Q. Truong, H. D. Tuan, A. J. Fitzgerald, V. P. Wallace, and H. T. Nguyen, "High correlation of double Debye model parameters in skin cancer detection," in *2014 36th Annual International Conference of the IEEE Engineering in Medicine and Biology Society, EMBC 2014* (2014).

53. H. J. Liebe, G. A. Hufford, and T. Manabe, "A model for the complex permittivity of water at frequencies below 1 THz," Int. J. Infrared Millimeter Waves **12**, 659–675 (1991).

54. M. Scheller, C. Jansen, and M. Koch, "Applications of Effective Medium Theories in the Terahertz Regime," in *Recent Optical and Photonic Technologies* (2010), pp. 231–250.

55. G. G. Hernandez-Cardoso, A. K. Singh, and E. Castro-Camus, "Empirical comparison between effective medium theory models for the dielectric response of biological tissue at terahertz frequencies," Appl. Opt. **59**(13), D6–D11 (2020).

56. R. Gente, N. Born, N. Voß, W. Sannemann, J. Léon, M. Koch, and E. Castro-Camus, "Determination of leaf water content from terahertz time-domain spectroscopic data," J. Infrared, Millimeter, Terahertz Waves **34**, 316–323 (2013).

57. V. K. Tippavajhala, T. D. Magrini, D. C. Matsuo, M. G. P. Silva, P. P. Favero, L. R. De Paula, and A. A. Martin, "In Vivo Determination of Moisturizers Efficacy on Human Skin Hydration by Confocal Raman Spectroscopy," AAPS PharmSciTech **19**(7), 3177–3186 (2018).

58. R. A.V., "Ethnic skin types: Are there differences in skin structure and function?," Int. J. Cosmet. Sci. **28**, 79–93 (2006).

59. M. A. Farage, K. W. Miller, P. Elsner, and H. I. Maibach, "Structural characteristics of the aging skin: A review," Cutan. Ocul. Toxicol. **26**(4), 343–357 (2007).

60. L Baumann, "Skin ageing and its treatment," J. Pathol. **211**(2), 241–251 (2007).

61. A. Firooz, B. Sadr, S. Babakoohi, M. Sarraf-Yazdy, F. Fanian, A. Kazerouni-Timsar, M. Nassiri-Kashani, M. M. Naghizadeh, and Y. Dowlati, "Variation of biophysical parameters of the skin with age, gender, and body region," Sci. World J. **2012**, (2012).

62. C. Ehlers, U. I. Ivens, M. L. Møller, T. Senderovitz, and J. Serup, "Females have lower skin surface pH than men: A study on the influence of gender, forearm site variation, right/left difference and time of the day on the skin surface pH," Ski. Res. Technol. **7**(2), 90–94 (2001).

63. K. P. Wilhelm, A. B. Cua, and H. I. Maibach, "Skin Aging: Effect on Transepidermal Water Loss, Stratum Corneum Hydration, Skin Surface pH, and Casual Sebum Content," Arch. Dermatol. **127**(12), 1806–1809 (1991).

64. X. R. Barker and E. Pickwell-Macpherson, "In vivo THz Measurements of Human Skin: Investigating the Dependence on Ethnicity and Arm Dominance," in *International Conference on Infrared, Millimeter, and Terahertz Waves, IRMMW-THz* (2019), pp. 1–2.

65. X. G. Peralta, D. Lipscomb, G. J. Wilmink, and I. Echchgadda, "Terahertz spectroscopy of human skin tissue models with different melanin content," Biomed. Opt. Express **10**(6), 2942–2955 (2019).

66. H. Qiu, X. Long, J. C. Ye, J. Hou, J. Senee, A. Laurent, R. Bazin, F. Flament, A. Adam, J. Coutet, and B. Piot, "Influence of season on some skin properties: Winter vs. summer, as experienced by 354 Shanghaiese women of various ages," Int. J. Cosmet. Sci. **33**(4), 377 (2011).

67. K. A. Engebretsen, J. D. Johansen, S. Kezic, A. Linneberg, and J. P. Thyssen, "The effect of environmental humidity and temperature on skin barrier function and dermatitis," J. Eur. Acad. Dermatology Venereol. **30**(2), 223–249 (2016).

68. D. Voegeli, "The effect of washing and drying practices on skin barrier function," J. Wound, Ostomy Cont. Nurs. **35**(1), 84–90 (2008).

69. M. Akdeniz, T. Tomova-Simitchieva, G. Dobos, U. Blume-Peytavi, and J. Kottner, "Does dietary fluid intake affect skin hydration in healthy humans? A systematic literature review," Ski. Res. Technol. **24**(3), 459–465 (2018).

70. S. Fan, E. P. J. Parrott, B. S. Y. Ung, and E. Pickwell-MacPherson, "Calibration method to improve the accuracy of THz imaging and spectroscopy in reflection geometry," Photonics Res. **4**(3), A29--A35 (2016).

71. X. Chen, E. P. J. Parrott, B. S. Y. Ung, and E. Pickwell-Macpherson, "A Robust Baseline and Reference Modification and Acquisition Algorithm for Accurate THz Imaging," IEEE Trans. Terahertz Sci. Technol. **7**(5), 493–501 (2017).

72. Q. Sun, E. P. J. Parrott, Y. He, and E. Pickwell-MacPherson, "In vivo THz imaging of human skin: Accounting for occlusion effects," J. Biophotonics **11**(2), e201700111 (2018).

73. E. K. Chan, B. Sorg, D. Protsenko, M. O'Neil, M. Motamedi, and a. J. Welch, "Effects of compression on soft tissue optical properties," IEEE J. Sel. Top. Quantum Electron. **2**(4), 943–950 (1996).

74. P. Clarys, R. Clijsen, and A. O. Barel, "Influence of probe application pressure on in vitro and in vivo capacitance (Corneometer CM 825 ®) and conductance (Skicon 200 EX ®) measurements," Ski. Res. Technol. **17**(4), 445–450 (2011).

75. K. Reimann, "Table-top sources of ultrashort THz pulses," Reports Prog. Phys. **70**(10), 1597–1632 (2007).

76. R. R. Warner, M. C. Myers, and D. a Taylor, "Electron probe analysis of human skin: determination of the water concentration profile.," J. Invest. Dermatol. **90**(2), 218–224 (1988).

77. H. Lindley-Hatcher, A. I. Hernandez-Serrano, Q. Sun, J. Wang, J. Cebrian, L. Blasco, and E. Pickwell-MacPherson, "A Robust Protocol for In Vivo THz Skin Measurements," J. Infrared, Millimeter, Terahertz Waves **40**(9), 980–989 (2019).

78. D. Stavrou, O. Weissman, E. Winkler, L. Yankelson, E. Millet, O. P. Mushin, A. Liran, and J. Haik, "Silicone-based scar therapy: A review of the literature," Aesthetic Plast. Surg. **34**(5), 646–651 (2010).

79. B. Berman, O. A. Perez, S. Konda, B. E. Kohut, M. H. Viera, S. Delgado, D. Zell, and Q. Li, "A review of the biologic effects, clinical efficacy, and safety of silicone elastomer sheeting for hypertrophic and keloid scar treatment and management," Dermatologic Surg. **33**(11), 1291–1303 (2007).

80. T. A. Mustoe, "Evolution of silicone therapy and mechanism of action in scar management," Aesthetic Plast. Surg. **32**(1), 82–92 (2008).

81. S. Y. Kwon, S. D. Park, and K. Park, "Comparative effect of topical silicone gel and topical tretinoin cream for the prevention of hypertrophic scar and keloid formation

and the improvement of scars," J. Eur. Acad. Dermatology Venereol. **28**(8), 1025–1033 (2014).

82. T. A. Mustoe and A. Gurjala, "The role of the epidermis and the mechanism of action of occlusive dressings in scarring," Wound Repair Regen. **19**, 16–21 (2011).

83. M. A. Musgrave, N. Umraw, J. S. Fish, M. Gomez, and R. C. Cartotto, "The effect of silicone gel sheets on perfusion of hypertrophic burn scars," J. Burn Care Rehabil. **23**(3), 208–214 (2002).

84. B. Hirshowitz, E. Lindenbaum, Y. Har-Shai, L. Feitelberg, M. Tendler, and D. Katz, "Static-electric field induction by a silicone cushion for the treatment of hypertrophic and keloid scars," Plast. Reconstr. Surg. **101**(5), 1173–1183 (1998).

85. P. S. Powers, S. Sarkar, D. B. Goldgof, C. W. Cruse, and L. V. Tsap, "Scar assessment: Current problems and future solutions," J. Burn Care Rehabil. **20**(1), 54–60 (1999).

86. P. P. M. Van Zuijlen, A. P. Angeles, R. W. Kreis, K. E. Bos, and E. Middelkoop, "Scar assessment tools: Implications for current research," Plast. Reconstr. Surg. **109**(3), 1108–1122 (2002).

87. Q. Sun, R. I. Stantchev, J. Wang, E. P. J. Parrott, A. Cottenden, T. W. Chiu, A. T. Ahuja, and E. Pickwell-MacPherson, "In vivo estimation of water diffusivity in occluded human skin using terahertz reflection spectroscopy," J. Biophotonics **12**(2), e201800145 (2019).

88. S. H. Bariya, M. C. Gohel, T. A. Mehta, and O. P. Sharma, "Microneedles: An emerging transdermal drug delivery system," J. Pharm. Pharmacol. **1**(64), 11–29 (2012).

89. Y.-C. Kim, J.-H. Park, and M. R. Prausnitz, "Microneedles for drug and vaccine delivery," Adv. Drug Deliv. Rev. **64**(14), 1547–1568 (2012).

90. M. R. Prausnitz, "Engineering Microneedle Patches for Vaccination and Drug Delivery to Skin," Annu. Rev. Chem. Biomol. Eng. **8**, 177–200 (2017).

91. J. Zhao, Y. Wu, J. Chen, B. Lu, H. Xiong, Z. Tang, and Y. Ji, "In vivo monitoring of microneedle-based transdermal drug delivery of insulin," J. Innov. Opt. Health Sci. **11**(5), 1–12 (2018).

92. J. Li, B. Liu, Y. Zhou, Z. Chen, L. Jiang, W. Yuan, and L. Liang, "Fabrication of a Ti porous microneedle array by metal injection molding for transdermal drug delivery," PLoS One **2**(12), e0172043 (2017).

93. R. Naccache, A. Mazhorova, M. Clerici, R. Piccoli, L. K. Khorashad, A. O. Govorov, L. Razzari, F. Vetrone, and R. Morandotti, "Terahertz Thermometry: Combining Hyperspectral Imaging and Temperature Mapping at Terahertz Frequencies," Laser Photonics Rev. **5**(11), 1600342 (2017).

94. S. J. Oh, S.-H. Kim, K. Jeong, Y. Park, Y.-M. Huh, J.-H. Son, and J.-S. Suh, "Measurement depth enhancement in terahertz imaging of biological tissues," Opt. Express **21**(18), 21299–21305 (2013).

95. U. T. LASHMAR, J. HADGRAFT, and N. THOMAS, "Topical Application of Penetration Enhancers to the Skin of Nude Mice: a Histopathological Study," J. Pharm. Pharmacol. **41**(2), 118–121 (1989).

96. H. O. Ammar, M. Ghorab, S. A. El-Nahhas, and R. Kamel, "Design of a transdermal delivery system for aspirin as an antithrombotic drug," Int. J. Pharm. **327**(1–2), 81–88 (2006).

97. S. S. Shapiro and M. B. Wilk, "An Analysis of Variance Test for Normality (Complete Samples)," Biometrika **52**(3/4), 591–611 (1965).

98. J. W. Tukey, "Comparing Individual Means in the Analysis of Variance," Biometrics **5**(2), 99–114 (1949).

99. G. K. Menon, G. W. Cleary, and M. E. Lane, "The structure and function of the stratum corneum," Int. J. Pharm. **435**(1), 3–9 (2012).

100. P. S. Tajreja, N. K. Kleene, W. L. Pickens, T. F. Wang, and G. B. Kasting, "Visualization of the lipid barrier and measurement of lipid pathlength in human stratum corneum," AAPS PharmSci **3**(2), 48–65 (2001).

101. X. Chen, E. P. J. Parrott, Z. Huang, H.-P. Chan, and E. Pickwell-MacPherson, "Robust and accurate terahertz time-domain spectroscopic ellipsometry," Photonics Res. **6**(8), 768–775 (2018).

102. X. Chen and E. Pickwell-Macpherson, "A sensitive and versatile thickness determination method based on non-inflection terahertz property fitting," Sensors **19**(19), 4118 (2019).

103. J. Wang, R. I. Stantchev, Q. Sun, T.-W. Chiu, A. T. Ahuja, and E. P. MacPherson, "THz in vivo measurements: the effects of pressure on skin reflectivity," Biomed. Opt. Express **9**(12), 6467–6476 (2018).

104. R. I. Stantchev, X. Yu, T. Blu, and E. Pickwell-MacPherson, "Real-time terahertz imaging with a single-pixel detector," Nat. Commun. **11**(1), 1–8 (2020).

105. J. Clegg and M. P. Robinson, "A genetic algorithm used to fit Debye functions to the dielectric properties of tissues," in *2010 IEEE World Congress on Computational Intelligence, WCCI 2010 - 2010 IEEE Congress on Evolutionary Computation, CEC 2010* (2010).

106. J. Clegg and M. P. Robinson, "A genetic algorithm for optimizing multi-pole Debye models of tissue dielectric properties," Phys. Med. Biol. **57**(19), 6227 (2012).

107. X. Ding, F. Yang, X. Yu, M. Li, B. Gao, Y. Fang, and X. Huang, "Optimization of data fitting algorithm for tissue dielectric properties in THz-band using genetic algorithm," in *International Conference on Infrared, Millimeter, and Terahertz Waves, IRMMW-THz* (2019).

108. B. C. Q. Truong, H. D. Tuan, H. H. Kha, and H. T. Nguyen, "Global optimization for human skin investigation in terahertz," in *Proceedings of the Annual International Conference of the IEEE Engineering in Medicine and Biology Society, EMBS* (2012), pp. 5474–5477.

109. B. C. Q. Truong, H. D. Tuan, H. H. Kha, and H. T. Nguyen, "Debye parameter extraction for characterizing interaction of terahertz radiation with human skin tissue," IEEE Trans. Biomed. Eng. **60**(6), 1528–1537 (2013).

110. K. Yang, N. Chopra, Q. H. Abbasi, K. A. Qaraqe, and A. Alomainy, "Collagen Analysis at Terahertz Band Using Double-Debye Parameter Extraction and Particle Swarm Optimisation," IEEE Access **5**, 27850–27856 (2017).